

UNIVERSITY OF CALIFORNIA
SANTA CRUZ

**SEARCH FOR WW AND WZ RESONANCE PRODUCTION IN
 $\ell\nu qq$ FINAL STATES IN pp COLLISIONS AT $\sqrt{s} = 13$ TEV WITH
THE ATLAS DETECTOR**

A dissertation submitted in partial satisfaction of the
requirements for the degree of

DOCTOR OF PHILOSOPHY

in

PHYSICS

by

Natasha Woods

June 2019

The Dissertation of Natasha Woods
is approved:

Abraham Seiden, Chair

Mike Hance

Bruce Schumm

Tyrus Miller
Vice Provost and Dean of Graduate Studies

Copyright © by

Natasha Woods

2019

Table of Contents

List of Figures	vi
List of Tables	xv
Abstract	xvi
Dedication	xvii
Acknowledgments	xviii
1 Theoretical Motivation	1
1.1 The Standard Model of Particle Physics	1
1.1.1 Introduction	1
1.1.2 Quantum Field Theory	1
1.1.3 $U(1)_{EM}$ Local Gauge Invariance	2
1.1.4 Yang-Mills Gauge Theories	5
1.1.5 Particles in the Standard Model	6
1.1.6 Higgs Mechanism	11
1.1.7 Electroweak Theory	12
1.1.8 Quantum ChromoDynamics	12
1.2 Standard Model Successes and Limitations	18
1.3 New Physics Models with Diboson Resonances	20
1.3.1 Randall Sundrum Bulk Model	20
1.3.2 Extended Scalar Sector	21
1.3.3 Simple Standard Model Extensions	22
2 LHC and ATLAS Detector	25
2.1 LHC	25
2.2 The ATLAS Detector	31
2.2.1 Coordinate System	33
2.3 Inner Detector	34
2.3.1 Pixel Detector	37

2.3.2	Semiconductor Tracker	37
2.3.3	Transition Radiation Tracker	37
2.4	Calorimeters	39
2.5	Muon Spectrometer	42
2.6	Magnet System	46
2.7	Trigger System	47
3	Analysis	49
3.1	Dataset and Simulated Samples	49
3.1.1	Dataset	49
3.1.2	Simulated Samples	52
3.2	Object Selection	52
3.2.1	Electrons	52
3.2.2	Muons	53
3.2.3	small-R jets	55
3.2.4	large-R jets	58
3.2.5	Variable Radius jets	61
3.2.6	MET/neutrinos	61
3.2.7	Jet Flavor Tagging	61
3.2.8	Overlap Removal	62
3.3	Event Selection and Categorization	63
3.3.1	Pre-selection	63
3.3.2	Trigger	63
3.3.3	GGF/VBF RNN	65
3.3.4	Topological Cuts	70
3.4	Background Estimate	80
3.4.1	Multijet Sample	80
3.5	Systematics	93
3.5.1	Experimental Systematics	93
3.5.2	Theory Systematics	95
3.6	Statistical Analysis	103
3.7	Fitted Systematics	106
3.8	Fit Results	106
3.9	Results	106
3.9.1	Quark/Gluon Tagging	106
4	Quark and Gluon Tagging	122
4.1	Prospects	122
4.2	n_{trk} Calibration	128
4.3	Application	133
5	Conclusion	138
5.1	Conclusions	138

List of Figures

1.1	The particles of the Standard Model.	8
1.2	Summary of how Standard Model particles interact with other Standard Model particles.	9
1.3	This figure shows the three dominant QCD interactions. From Ref. [14]	14
1.4	Strength of the U(1), SU(2), and SU(3) gauge couplings as a function of the energy scale of the interaction (Q). From Ref. [10] . .	16
1.5	A comparison of cross section measurements at $\sqrt{s} = 7, 8, 13$ TeV from ATLAS compared to theoretical measurements. From Ref. [5]	19
1.6	Cartoon of RS Bulk Model	21
2.1	Scaling of cross sections with \sqrt{s} . Natasha: write more here . . .	26
2.2	LHC Layout. Natasha write more	28
2.3	LHC Accelerator. Natasha write more	30
2.4	Big picture layout of ATLAS detector. Natasha: write more . . .	32
2.5	Big picture layout of ATLAS detector. Natasha: write more . . .	32
2.6	A simplified schematic of how different particles interact and are detected within ATLAS.	33
2.7	Layout of ATLAS Inner Detector	35
2.8	Layout of ATLAS ID Barrel System.	36
2.9	Overview of ATLAS electromagnetic and hadronic calorimeters. .	40
2.10	Schematic of ECAL.	41
2.11	Schematic of HCAL.	41

2.12	Schematic of Muon Spectrometer [cite G35]	44
2.13	Schematic of MDT chamber. [cite G35]	45
2.14	Schematic of RPC chamber, which is used for triggering in the central region of the detector [cite G35].	45
2.15	Schematic of TGC chamber, which is used for triggering in the muon end-cap region. [cite G35]	46
2.16	Layout of ATLAS magnet systems.	47
3.1	Integrated luminosity for data collected from ATLAS from 2011 - 2018	50
3.2	Mean number of interactions per crossing for data collected from ATLAS from 2011 - 2018	51
3.3	[4] This figure show the breakdown of the muon reconstruction efficiency scale factor measured in $Z \rightarrow \mu\mu$ as a function of p_T	55
3.4	[6] This diagram shows the calibration stages for EM jets.	58
3.5	The upper cut on D_2 (a) and jet mass window cut i.e. the upper and lower boundary of the mass (b) of the W -tagger as a function of jet p_T . Corresponding values for Z -tagger are shown in (c) and (d). The optimal cut values for maximum significance are shown as solid markers and the fitted function as solid lines. Working points from $VV \rightarrow JJ$ [ATLAS-HDBS-2018-31-002] is also shown as dashed lines as a reference. Natasha reword?	60
3.6	Natasha write caption	60
3.7	RNN architecture. Natasha add caption	67
3.8	RNN Score distribution for ggF and VBF signals and backgrounds.	68
3.9	ROC curve using k-fold validation for RNN.	69
3.10	Comparison of GGF Z' limits for different RNN score selections.	70
3.11	Event Categorization. Natasha write more.	73
3.12	Data MC comparison for the merged WW HP TCR.	74
3.13	Data MC comparison for the merged WW LP TCR.	75
3.14	Data MC comparison for the merged WZ HP TCR.	76

3.15	Data MC comparison for the merged WZ LP TCR.	77
3.16	Data MC comparison for the resolved WW TCR.	78
3.17	Data MC comparison for the resolved WZ TCR.	79
3.18	The E_T^{miss} distribution in MJCR for 2017 data in the electron channel(left), muon channel with W-boson pT < 150 GeV (center) and > 150 GeV (right). Multi-jet templates are calculated as remaining data components after excluding known MC	82
3.19	Postfit Data/MC comparison of distributions of E_T^{miss} , m_T^W , lepton and neutrino p_T , $m_{\ell\nu jj}$, lepton- ν angular distance in the WW electron channel. The MJ template is obtained from the pre-MJ-fit.	83
3.20	Postfit Data/MC comparison of distributions of E_T^{miss} , m_T^W , lepton and neutrino p_T , $m_{\ell\nu jj}$, lepton- ν angular distance in the WW muon channel. The MJ template is obtained from the pre-MJ-fit.	84
3.21	Postfit Data/MC comparison of distributions of E_T^{miss} , m_T^W , lepton and neutrino p_T , $m_{\ell\nu jj}$, lepton- ν angular distance in the WZ untag electron channel. The MJ template is obtained from the pre-MJ-fit.	85
3.22	Postfit Data/MC comparison of distributions of E_T^{miss} , m_T^W , lepton and neutrino p_T , $m_{\ell\nu jj}$, lepton- ν angular distance in the WZ untag muon channel. The MJ template is obtained from the pre-MJ-fit.	86
3.23	Postfit Data/MC comparison of distributions of E_T^{miss} , m_T^W , lepton and neutrino p_T , $m_{\ell\nu jj}$, lepton- ν angular distance in the WZ untag electron channel. The MJ template is obtained from the pre-MJ-fit.	87
3.24	Postfit Data/MC comparison of distributions of E_T^{miss} , m_T^W , lepton and neutrino p_T , $m_{\ell\nu jj}$, lepton- ν angular distance in the WZ untag muon channel. The MJ template is obtained from the pre-MJ-fit.	88
3.25	Postfit Data/MC comparison of distributions of E_T^{miss} , m_T^W , lepton and neutrino p_T , $m_{\ell\nu jj}$, lepton- ν angular distance in the VBF WW electron channel. The MJ template is obtained from the pre-MJ-fit.	89
3.26	Postfit Data/MC comparison of distributions of E_T^{miss} , m_T^W , lepton and neutrino p_T , $m_{\ell\nu jj}$, lepton- ν angular distance in the VBF WW muon channel. The MJ template is obtained from the pre-MJ-fit.	90

3.27 Postfit Data/MC comparison of distributions of E_T^{miss} , m_T^W , lepton and neutrino p_T , $m_{\ell\nu jj}$, lepton- ν angular distance in the VBF WZ electron channel. The MJ template is obtained from the pre-MJ-fit.	91
3.28 Postfit Data/MC comparison of distributions of E_T^{miss} , m_T^W , lepton and neutrino p_T , $m_{\ell\nu jj}$, lepton- ν angular distance in the VBF WZ muon channel. The MJ template is obtained from the pre-MJ-fit.	92
3.29 The $W/Z+jet$ systematics for the a) Merged ggF, b) Resolved ggF, c) Merged VBF, and d) Resolved VBF regions. The top subplot shows the nominal and variation distributions/bands, the middle shows the ratio of the two, and the final shows just the shape of the envelope (the final uncertainty).	96
3.30 The two-point generator comparison between Sherpa and MadGraph for the $W/Z+jet$ samples in the a) Merged ggF, b) Resolved ggF, c) Merged VBF, and d) Resolved VBF regions. The normalization of the Madgraph sample is set to the Sherpa value to consider only shape effects. The bottom inlet shows the ratio of the two.	98
3.31 Ratio between the variations of generator (red) and hadronization (blue) variations for the Merged regime for $t\bar{t}$ sample.	99
3.32 Ratio between the variations of generator (red) and hadronization (blue) variations for the Resolved regime for $t\bar{t}$ sample.	99
3.33 Ratio between the variations of ISR up (red) and down (blue) variations for the Merged regime for $t\bar{t}$ sample.	100
3.34 Ratio between the variations of ISR up (red) and down (blue) variations for the Resolved regime for $t\bar{t}$ sample.	101
3.35 Ratio between the variations of FSR up (red) and down (blue) variations for the Merged regime for $t\bar{t}$ sample.	102
3.36 Ratio between the variations of FSR up (red) and down (blue) variations for the Resolved regime for $t\bar{t}$ sample.	102

3.37	PDGID of the truth-level parton matched to the small-R jets passing the Resolved GGF WW Signal Region selections for the (a) Leading (b) Sub-Leading jets . These distributions are shown for 300, 500, and 700GeV Z' signals and the background.	108
3.38	The number of tracks in small-R jets in events passing the Resolved GGF WW Signal Region selections for the (a) Leading (b) Sub-Leading jets. These distributions are shown for 300, 500, and 700GeV Z' signals and the background.	108
3.39	The number of tracks in background small-R jets in events passing the Resolved GGF WW Signal region selection vs. $\ln(p_T)$ for (a)Leading (b) Sub-Leading jets. The best fit line for the distribution is also shown, as well as the percentage of jets that pass a cut of number of tracks $< 4 \times \ln(p_T) - 5$. Note the number of total entries in these plots has been normalized to one.	109
3.40	The number of tracks in small-R jets in 300GeV Z' events passing the Resolved GGF WW Signal region selection vs. $\ln(p_T)$ for (a)Leading (b) Sub-Leading jets. The best fit line for the distribution is also shown, as well as the percentage of jets that pass a cut of number of tracks $< 4 \times \ln(p_T) - 5$.Note the number of total entries in these plots has been normalized to one.	109
3.41	The number of tracks in small-R jets in 500GeV Z' events passing the Resolved GGF WW Signal region selection vs. $\ln(p_T)$ for (a)Leading (b) Sub-Leading jets. The best fit line for the distribution is also shown, as well as the percentage of jets that pass a cut of number of tracks $< 4 \times \ln(p_T) - 5$.Note the number of total entries in these plots has been normalized to one.	110

3.42 The number of tracks in small-R jets in 700GeV Z' events passing the Resolved GGF WW Signal region selection vs. $\ln(p_T)$ for (a)Leading (b) Sub-Leading jets. The best fit line for the distribution is also shown, as well as the percentage of jets that pass a cut of number of tracks $< 4 \times \ln(p_T) - 5$.Note the number of total entries in these plots has been normalized to one.	110
3.43 The number of tracks in leading small-R jets in background events passing the Resolved GGF WW Signal region selection vs. $\ln(p_T)$ for (a)Gluons (b) Quarks jets. The best fit line for the distribution is also shown, as well as the percentage of jets that pass a cut of number of tracks $< 4 \times \ln(p_T) - 5$.Note the number of total entries in these plots has been normalized to one.	111
3.44 ROC Curve for Quark and Gluon Tagging with a cut on the number of tracks that depends on the $\ln(p_T)$	111
3.45 The top panel shows the distribution of m_{lvqq} with and without quark gluon tagging. The middle panel shows the ratio of the signals and backgrounds with and without quark gluon tagging. The bottom panel shows the change in S/\sqrt{B} with quark gluon tagging.	112
3.46 The top panel shows the distribution of m_{lvqq} with and without requiring jets to be true quarks. The middle panel shows the ratio of the signals and backgrounds with and without requiring jets to be true quarks. The bottom panel shows the change in S/\sqrt{B} when requiring jets to be true quarks.	118
3.47 Unfolded and extracted n_C qg dstbs.	119
3.48 PDGID of the truth-level parton matched to the small-R jets passing the Resolved GGF WW Signal Region selections for the (a) Leading (b) Sub-Leading jets . These distributions are shown for 300, 500, and 700GeV Z' signals and the background.	120

3.49 These figures show the impact of the uncertainties on the number of tracks in the leading jet in the sum of the background sample in the Resolved GGF WW SR (a) tracking efficiency (b) fake (c) PDF (d) ME (e) unfolding uncertainties.	121
4.1 PDGID of the truth-level parton matched to the small-R jets passing the Resolved GGF WW Signal Region selections for the (a) Leading (b) Sub-Leading jets . These distributions are shown for 300, 500, and 700GeV Z' signals and the background.	124
4.2 The number of tracks in small-R jets in events passing the Resolved GGF WW Signal Region selections for the (a) Leading (b) Sub-Leading jets. These distributions are shown for 300, 500, and 700GeV Z' signals and the background.	124
4.3 The number of tracks in background small-R jets in events passing the Resolved GGF WW Signal region selection vs. $\ln(p_T)$ for (a)Leading (b) Sub-Leading jets. The best fit line for the distribution is also shown, as well as the percentage of jets that pass a cut of number of tracks $< 4 \times \ln(p_T) - 5$. Note the number of total entries in these plots has been normalized to one.	125
4.4 The number of tracks in small-R jets in 300GeV Z' events passing the Resolved GGF WW Signal region selection vs. $\ln(p_T)$ for (a)Leading (b) Sub-Leading jets. The best fit line for the distribution is also shown, as well as the percentage of jets that pass a cut of number of tracks $< 4 \times \ln(p_T) - 5$.Note the number of total entries in these plots has been normalized to one.	125
4.5 The number of tracks in small-R jets in 500GeV Z' events passing the Resolved GGF WW Signal region selection vs. $\ln(p_T)$ for (a)Leading (b) Sub-Leading jets. The best fit line for the distribution is also shown, as well as the percentage of jets that pass a cut of number of tracks $< 4 \times \ln(p_T) - 5$.Note the number of total entries in these plots has been normalized to one.	126

4.6	The number of tracks in small-R jets in 700GeV Z' events passing the Resolved GGF WW Signal region selection vs. $\ln(p_T)$ for (a)Leading (b) Sub-Leading jets. The best fit line for the distribution is also shown, as well as the percentage of jets that pass a cut of number of tracks $< 4 \times \ln(p_T) - 5$.Note the number of total entries in these plots has been normalized to one.	126
4.7	The number of tracks in leading small-R jets in background events passing the Resolved GGF WW Signal region selection vs. $\ln(p_T)$ for (a)Gluons (b) Quarks jets. The best fit line for the distribution is also shown, as well as the percentage of jets that pass a cut of number of tracks $< 4 \times \ln(p_T) - 5$.Note the number of total entries in these plots has been normalized to one.	127
4.8	ROC Curve for Quark and Gluon Tagging with a cut on the number of tracks that depends on the $\ln(p_T)$	127
4.9	The top panel shows the distribution of m_{lvqq} with and without quark gluon tagging. The middle panel shows the ratio of the signals and backgrounds with and without quark gluon tagging. The bottom panel shows the change in S/\sqrt{B} with quark gluon tagging.	128
4.10	The top panel shows the distribution of m_{lvqq} with and without requiring jets to be true quarks. The middle panel shows the ratio of the signals and backgrounds with and without requiring jets to be true quarks. The bottom panel shows the change in S/\sqrt{B} when requiring jets to be true quarks.	134
4.11	Unfolded and extracted n_C qg dstbs.	135
4.12	PDGID of the truth-level parton matched to the small-R jets passing the Resolved GGF WW Signal Region selections for the (a) Leading (b) Sub-Leading jets . These distributions are shown for 300, 500, and 700GeV Z' signals and the background.	136

4.13 These figures show the impact of the uncertainties on the number
of tracks in the leading jet in the sum of the background sample
in the Resolved GGF WW SR (a) tracking efficiency (b) fake (c)
PDF (d) ME (e) unfolding uncertainties. 137

List of Tables

1.1	Representations of the SM fermions under $SU(3)_C \times SU(2)_L \times U(1)_Y$ gauge symmetry group. $SU(2)_L$ gauge transformations allow one to go between rows and $SU(3)_C$ transformations allow one to go between columns in these fermion representations. [REWORD]	7
3.1	The list of triggers used in the analysis.	64
3.2	Summary of selection criteria used to define the signal region (SR), W +jets control region (W CR) and $t\bar{t}$ control region ($t\bar{t}$ CR) for merged 1-lepton channel.	72
3.3	The list of selection cuts in the resolved analysis for the WW and WZ signal regions (SR), W +jets control region (WR) and $t\bar{t}$ control region (TR).	73
3.4	Definitions of “inverted” leptons used in multijet control region . .	81
3.5	Fit validation result in WCRs for 2015+16 data. The fit is done in various WCRs, in order to obtain the corresponding scale factors for MJ templates: ggF resolved WCR for the $WW \rightarrow lvqq$ selection, ggF resolved untagged WCR for the $WZ \rightarrow lvqq$ selection, ggF resolved tagged WCR for the $WZ \rightarrow lvqq$ selection, VBF resolved WCR for the $WW \rightarrow lvqq$ selection, and VBF resolved WCR for the $WZ \rightarrow lvqq$ selection. Post-fit event yields for electroweak processes and MJ contributions are shown. The SF column shows the corresponding normalization scale factors for electroweak processes from the fit. R.U. stands for relative uncertainty.	97

Abstract

Search for WW and WZ resonance production in $\ell\nu qq$ final states in pp collisions at $\sqrt{s} = 13$ TeV with the ATLAS detector

by

Natasha Woods

tl;dr description of research

A loving dedication.

å

xvii

Acknowledgments

Proper acknowledgments of everyone else who helped you graduate. Write later

¹ Chapter 1

² Theoretical Motivation

³ Intro goes here

⁴ 1.1 The Standard Model of Particle Physics

⁵ 1.1.1 Introduction

⁶ By determining the dynamics of the most elementary degrees of freedom, par-
⁷ ticle physics hopes to uncover the fundamental laws of the universe. The definition
⁸ of elementary has evolved through time and currently refers to matter and force
⁹ mediating particles: fermions and bosons, respectively. The Standard Model of
¹⁰ Particle Physics (SM) describes the quantum behavior of three of the four funda-
¹¹ mental forces: weak, strong, and electromagnetic, via boson and fermion interac-
¹² tions. Gravity is not included in the SM and still under investigation.

¹³ 1.1.2 Quantum Field Theory

¹⁴ In the SM, forces (and particles) are represented as fields. In this context,
¹⁵ fields are mathematical objects that define a tensor (e.g. scalar, vector, etc) at

¹⁶ every point on a manifold, here the manifold is space-time. These fields obey laws
¹⁷ dictated by Quantum Field Theory (QFT). Particles arise naturally in QFT as
¹⁸ quantized field excitations localized in spacetime.

¹⁹ According to Noether's theorem, symmetries of a field give rise to conserved
²⁰ quantities (e.g. time-translation invariance leads to energy conservation). Often
²¹ in the history of physics, a conserved quantity of a field is found and then the
²² underlying symmetry of the field is inferred. Gauge symmetries are symmetries
²³ among the internal degrees of freedom of the field (components of the tensor),
²⁴ which give rise to quantities associated with fields. By specifying the symmetries
²⁵ of a system the dynamics and conserved quantities of the system may be succinctly
²⁶ defined.

²⁷ 1.1.3 $U(1)_{EM}$ Local Gauge Invariance

²⁸ The Lagrangian of Quantum Electrodynamics (QED) describes the electro-
²⁹ magnetic force. QED may be derived by requiring local $U(1)_{EM}$ gauge invariance
³⁰ of the free dirac fermion Lagrangian, ψ :

$$\mathcal{L} = i\bar{\psi}\gamma^\mu\partial_\mu\psi - m\bar{\psi}\psi \quad (1.1)$$

³¹ This symmetry may be represented as a complex number with unit modulus,
³² $e^{i\theta}$. $U(1)$ gauge invariance requires this gauge transformation of ψ will leave the
³³ Lagrangian unchanged.

$$\psi(x) \rightarrow \psi'(x) = e^{i\theta(x)}\psi(x) \quad (1.2)$$

³⁴ NB: This transformation is a local gauge transformation as θ depends on the
³⁵ spacetime coordinate.

³⁶ By requiring this symmetry of the free Dirac fermion Lagrangian:

$$\mathcal{L} = i\bar{\psi}\gamma^\mu\partial_\mu\psi - m\bar{\psi}\psi \quad (1.3)$$

³⁷ The mass term is unaffected, but the kinetic term is modified due to $\theta(x)$.

$$\mathcal{L} \rightarrow \mathcal{L}' = i\bar{\psi}e^{-i\theta(x)}\gamma^\mu\partial_\mu\psi e^{i\theta(x)} - m\bar{\psi}e^{-i\theta(x)}\psi e^{i\theta(x)} \quad (1.4)$$

³⁸

$$= i\bar{\psi}\gamma^\mu(\partial_\mu\psi + i\psi\partial_\mu\theta) - m\bar{\psi}\psi \quad (1.5)$$

³⁹ The $\partial_\mu\theta$ terms breaks the gauge invariance of the Lagrangian. By introducing a
⁴⁰ new field, A_μ we can recover the gauge invariance of the derivative. Now redefining
⁴¹ the derivative as the covariant derivative:

$$D_\mu\psi \equiv (\partial_\mu - iqA_\mu)\psi \quad (1.6)$$

⁴² And letting A_μ transform under U(1) as:

$$A_\mu \rightarrow A_\mu + \delta A_\mu \quad (1.7)$$

⁴³ The transformed covariant derivative becomes:

$$D_\mu\psi \rightarrow D_\mu\psi' = (\partial_\mu - iqA_\mu)\psi' \quad (1.8)$$

⁴⁴

$$= (\partial_\mu - iq(A_\mu + \delta A_\mu))\psi e^{i\theta} \quad (1.9)$$

⁴⁵

$$= e^{i\theta}D_\mu + ie^{i\theta}\psi(\partial_\mu\theta - q\delta A_\mu)) \quad (1.10)$$

⁴⁶ The covariant derivative can be made gauage invariant by setting the last term
⁴⁷ to zero.

$$\delta A_\mu = \frac{1}{q} \partial_\mu \theta \quad (1.11)$$

⁴⁸ So now A_μ transforms as:

$$A_\mu \rightarrow A_\mu + \frac{1}{q} \partial_\mu \theta \quad (1.12)$$

⁴⁹ Finally, replacing the derivative with the covariant derivative the Dirac La-
⁵⁰ grangian we have:

$$\mathcal{L} = i\bar{\psi}\gamma^\mu D_\mu \psi - m\bar{\psi}\psi - \frac{1}{4}F_{\mu\nu}F^{\mu\nu} \quad (1.13)$$

⁵¹

$$= \mathcal{L}_{QED} \quad (1.14)$$

⁵² Here $F_{\mu\nu} \equiv \partial_\mu A_\nu - \partial_\nu A_\mu$. This last term in the Lagrangian is the kinetic
⁵³ energy of the gauge boson field.

⁵⁴ So we have derived the QED Lagrangian. By requiring the free Dirac La-
⁵⁵ grangian to be invariant under U(1) transformations we have generated a new
⁵⁶ field gauge boson field, A_μ , which describes the photon. As expected the photon
⁵⁷ interacts with fermions.

⁵⁸ Stepping back, a global U(1) gauge symmetry of the free Dirac Lagrangian
⁵⁹ implies we cannot measure the absolute phase of a charged particle. A local U(1)
⁶⁰ gauge symmetry changes the phase of fields differently across space time. For this
⁶¹ type of transformation to leave the Lagrangian invariant, we had to introduce an
⁶² additional field, A_μ , which "communicates" these phase changes across space-time.
⁶³ In less formal language this effectively means: if the field at one location changes,
⁶⁴ this change is conferred to other particles via A_μ .

⁶⁵ **1.1.4 Yang-Mills Gauge Theories**

⁶⁶ Requiring $U(1)_{EM}$ gauge invariance of the free Dirac Lagrangian gave us QED.

⁶⁷ Requiring different gauge symmetries we can derive the structure of other interactions.
⁶⁸ Any gauge symmetry may be written as:

$$\psi_i \rightarrow \exp(i\theta^a T_{ij}^a) \psi_j \quad (1.15)$$

⁶⁹ Here θ is a dimensionless real parameter and T is the generator of the gauge
⁷⁰ symmetry group. With this the covariant derivative can be written as:

$$D_\mu \psi_i \equiv \partial_\mu \psi_i + ig A_\mu^a T_{ij}^a \psi_j \quad (1.16)$$

⁷¹ Then the gauge field must transform as:

$$A_\mu^a \rightarrow A_\mu^a - \frac{1}{g} \partial_\mu \theta^a - f^{abc} \theta^b A_\mu^c \quad (1.17)$$

⁷² Here f is the structure constant of the gauge group. The field strength tensor
⁷³ is given by:

$$F_{\mu\nu}^a \equiv \partial_\mu A_\nu^a - \partial_\nu A_\mu^a - g f^{abc} A_\mu^b A_\nu^c \quad (1.18)$$

⁷⁴

$$F_{\mu\nu}^a \rightarrow F_{\mu\nu}^a - f^{abc} \theta^b F_{\mu\nu}^c \quad (1.19)$$

⁷⁵ This gives the Yang-Mills Lagrangian:

$$\mathcal{L}_{YM} = -\frac{1}{4} F^{a\mu\nu} F_{\mu\nu}^a + i \bar{\psi}_i \gamma^\mu D_\mu \psi_i + m \bar{\psi}_i \psi_i \quad (1.20)$$

76 **1.1.5 Particles in the Standard Model**

77 The SM consists of fermions (half-integer spin matter constituents) and bosons
78 (integer spin force mediators). Fermions are spinor representations of the Poincare
79 group and can be further separated into leptons and quarks. Bosons are the result
80 of requiring a particular symmetry among the spinor fields:

$$SU(3)_C \times SU(2)_L \times U(1)_Y \quad (1.21)$$

81 $SU(3)_C$ is the symmetry group of the strong force and generates eight gluon
82 fields, G_μ . $SU(2)_L$ is the symmetry group of the Electroweak force and generates
83 three electroweak boson fields, and $U(1)_Y$ generates the photon field, where Y is
84 the weak-hypercharge:

$$Y = 2(Q - T_3) \quad (1.22)$$

85 Q is the electromagnetic charge, and T_3 is the z-component of the weak isospin.
86 Weak isospin is the charge associated with the $SU(2)_L$ symmetry. The correspond-
87 ing covariant derivative is then:

$$D_\mu \phi \equiv (\partial_\mu + ig_1 B_\mu Y_{L/R} + [ig_2 W_\mu^\alpha T^\alpha]_L + [ig_3 G_\mu^\alpha \tau^\alpha]_C) \psi \quad (1.23)$$

88 It is important to note that the gauge symmetry of the SM yields a particular
89 structure of the fermion representations. So for a given fermion to interact with
90 a given gauge field it must have a non-zero corresponding Noether charge for
91 that gauge symmetry. If the corresponding Noether charge is zero, that fermion
92 transforms as a singlet and does not participate in that gauge interaction.

93 Fermions are divided into quarks and leptons based on their transformations
94 under $SU(3)_C$. Quarks transform as color triplets. Leptons transform as color

singlets and consequently do not interact with gluons. Fermions may be further
 classified by their $SU(2)_L$ interactions. Only the left-chiral part of fermions (denoted by L here) transform as $SU(2)_L$ doublets, the right-chiral part forms singlets under this gauge. Lastly, all these groups of particles come in three generations, each a heavier copy of the previous, but with differing flavor quantum numbers.
 This is summarized in Table 1.1 and shown in Figures 1.1 and 1.2.

SM Fermion Gauge Group	First Generation	Second Generation	Third Generation	$(SU(3)_C, SU(2)_L, U(1)_Y)$ Representations
Left-handed quarks	$\begin{pmatrix} u_L^r & u_L^g & u_L^b \\ d_L^r & d_L^g & d_L^b \end{pmatrix}$	$\begin{pmatrix} c_L^r & c_L^g & c_L^b \\ s_L^r & s_L^g & s_L^b \end{pmatrix}$	$\begin{pmatrix} t_L^r & t_L^g & t_L^b \\ b_L^r & b_L^g & b_L^b \end{pmatrix}$	$(3, 2, \frac{1}{6})$
Right-handed quarks	(u_R^r, u_R^g, u_R^b) (d_R^r, d_R^g, d_R^b)	(c_R^r, c_R^g, c_R^b) (s_R^r, s_R^g, s_R^b)	(t_R^r, t_R^g, t_R^b) (b_R^r, b_R^g, b_R^b)	$(3, 1, \frac{2}{3})$ $(3, 1, -\frac{1}{3})$
Left-handed leptons	$\begin{pmatrix} \nu_e^L \\ e_L \end{pmatrix}$	$\begin{pmatrix} \mu_e^L \\ \mu_L \end{pmatrix}$	$\begin{pmatrix} \tau_e^L \\ \tau_L \end{pmatrix}$	$(1, 2, -\frac{1}{2})$
Right-handed leptons	e_R	μ_R	τ_R	$(1, 1, -1)$

Table 1.1: Representations of the SM fermions under $SU(3)_C \times SU(2)_L \times U(1)_Y$ gauge symmetry group. $SU(2)_L$ gauge transformations allow one to go between rows and $SU(3)_C$ transformations allow one to go between columns in these fermion representations. [REWORD]

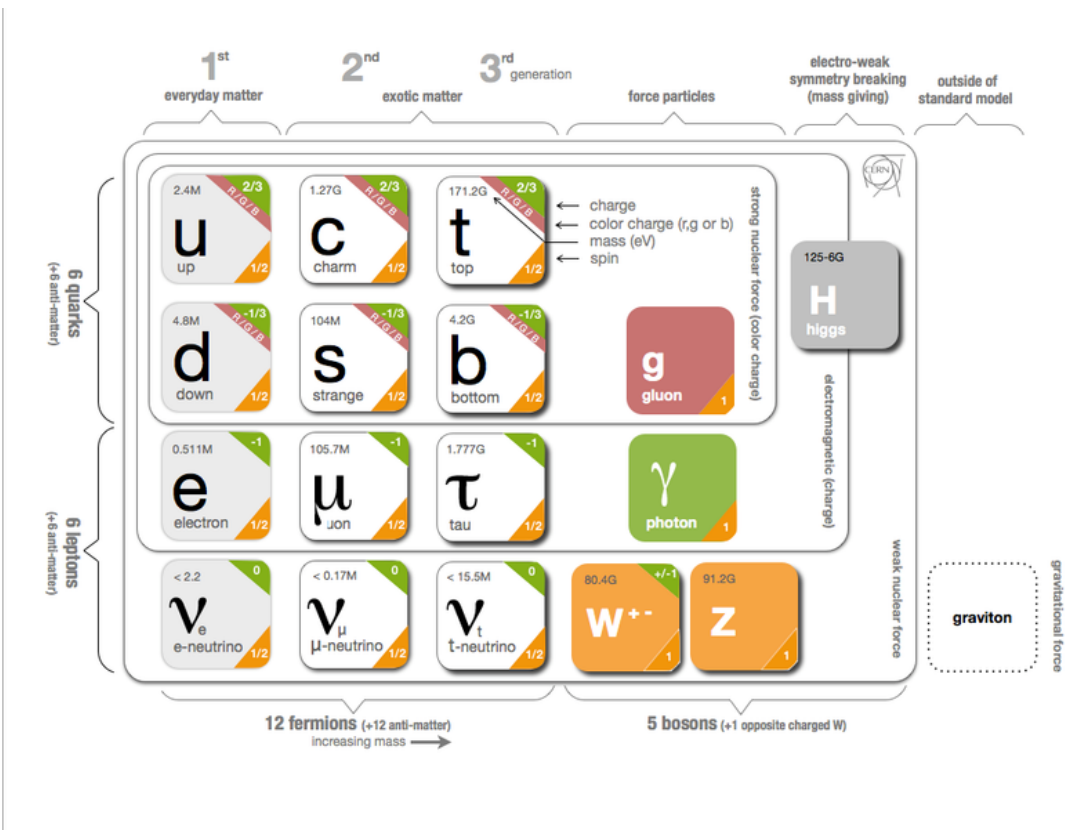


Figure 1.1: The particles of the Standard Model.

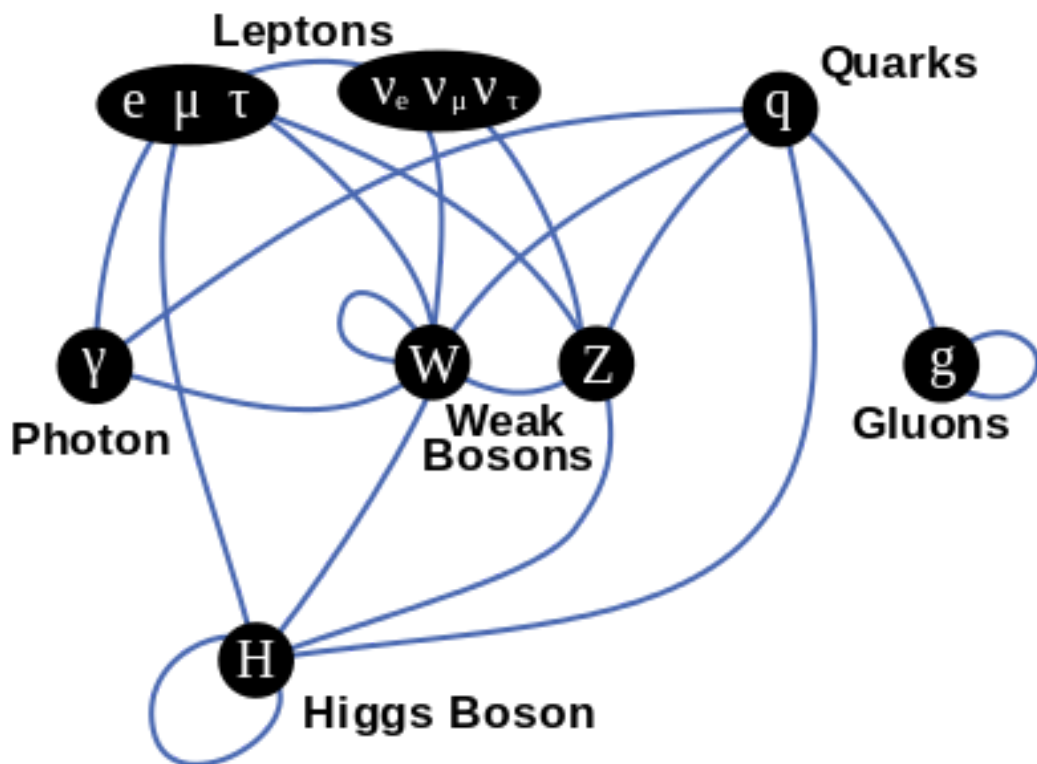


Figure 1.2: Summary of how Standard Model particles interact with other Standard Model particles.

101 Now we can understand the SM Lagrangian density as a Yang-Mills theory
 102 with the gauge group: $SU(3)_C \times SU(2)_L \times U(1)_Y$ with an additional $SU(2)$ complex
 103 scalar Higgs field doublet that will be discussed later.

$$\begin{aligned}
 \mathcal{L}_{SM} = & \underbrace{-\frac{1}{4}B_{\mu\nu}B^{\mu\nu} - \frac{1}{4}W_{\mu\nu}^a W^{a\mu\nu} - \frac{1}{4}G_{\mu\nu}^\alpha G^{\alpha\mu\nu}}_{\text{Kinetic Energies and Self-Interactions of Gauge Bosons}} \\
 & + \underbrace{\bar{L}_i \gamma^\mu (i\partial_\mu - \frac{1}{2}g_1 Y_{iL} B_\mu - \frac{1}{2}g_2 \sigma^a W_\mu^a) L_i}_{\text{Kinetic Energies and EW Interactions of Left-handed Fermions}} \\
 & + \underbrace{\bar{R}_i \gamma^\mu (i\partial_\mu - \frac{1}{2}g_1 Y_{iR} B_\mu) R_i}_{\text{Kinetic Energies and EW Interactions of Right-Handed Fermions}} \\
 & + \underbrace{\frac{ig_3}{2} \bar{Q}_j \gamma^\mu \lambda^\alpha G_\mu^\alpha Q_j}_{\text{Strong Interactions between Quarks and Gluons}} \\
 & + \underbrace{\frac{1}{2} |(i\partial_\mu - \frac{1}{2}g_1 B_\mu - \frac{1}{2}g_2 \sigma^a W_\mu^a)\Phi|^2 - V(\Phi)}_{\text{Electroweak Boson Masses and Higgs Couplings}} \\
 & - \underbrace{(y_{kl}^d \bar{L}_k \Phi R_l + y_{kl}^u \bar{R}_k \tilde{\Phi} L_l + h.c.)}_{\text{Fermion Mass terms and Higgs Couplings}}
 \end{aligned}$$

104 Here several abstract spaces are being spanned:

- 105 – a spans the three $SU(2)_L$ gauge fields with generators expanded in Pauli
 106 matrices, $T^\alpha = \frac{1}{2}\alpha^\alpha$
- 107 – α spans the eight $SU(3)_C$ gauge fields, with generators expanded in Gell-
 108 Mann matrices, $\tau^\alpha = \frac{1}{2}\lambda^\alpha$
- 109 – L/R represent left and right projections of Dirac fermion fields. The Strong
 110 interaction is not chiral, so $Q = L+R$

₁₁₁ – μ and ν are four-vector indices

₁₁₂ – i, j, k are summed over the three generations of SM particles.

₁₁₃ 1.1.6 Higgs Mechanism

₁₁₄ The SM Lagrangian without the addition of a Higgs field does not allow for
₁₁₅ gauge boson and fermion mass terms: $\frac{1}{2}m_A^2 A_\mu A_\mu$ and $m(\bar{\psi}\psi)$, as these terms are
₁₁₆ not gauge invariant. By introducing the Higgs field, mass terms for these particles
₁₁₇ may be included in a gauge invariant way. This field is a complex doublet with a
₁₁₈ potential $V(\Phi)$:

$$\Psi = \begin{pmatrix} \Phi^\dagger \\ \Phi^0 \end{pmatrix} \quad (1.24)$$

₁₁₉ $V(\Phi) = \mu^2 \Phi^\dagger \Phi + \lambda |\Phi^\dagger \Phi|^2 \quad (1.25)$

₁₂₀ The minima of this field occurs for $|\Phi| = \sqrt{\frac{\mu^2}{2\lambda}} \equiv \frac{v}{2}$. This yields degenerate
₁₂₁ minima, this symmetry is broken by choosing a specific minima (a.k.a. sponta-
₁₂₂ neous symmetry breaking). By convention $\Phi_{min} = \frac{1}{\sqrt{2}} \begin{pmatrix} 0 \\ v \end{pmatrix}$ is chosen. This means
₁₂₃ the ground state of the Higgs field (Higgs vacuum) is non-zero, $\sqrt{\frac{-\mu^2}{\lambda}}$. The Higgs
₁₂₄ Field may now be expanded around this new ground state:

$$\Phi(x) = \frac{1}{\sqrt{2}} \begin{pmatrix} 0 \\ v + h(x) \end{pmatrix} \quad (1.26)$$

₁₂₅ This non-zero Higgs vacuum now generates mass terms for the gauge bosons
₁₂₆ from the following term in the Lagrangian:

$$|(-\frac{1}{2}g_1 B_\mu - \frac{1}{2}g_2 \sigma^a W_\mu^a)\Phi|^2 = \frac{1}{2}m_W^2 W_\mu^+ W^{-\mu} + \frac{1}{2}m_Z^2 Z_\mu Z^\mu \quad (1.27)$$

¹²⁷ where:

$$W_\mu^\pm \equiv \frac{1}{\sqrt{2}}(W_\mu^1 \mp iW_\mu^2) \quad (1.28)$$

¹²⁸

$$Z_\mu \equiv \frac{1}{\sqrt{g_1^2 + g_2^2}}(g_2 W_\mu^2 - g_1 B_\mu) \quad (1.29)$$

¹²⁹

$$m_W = \frac{v g_2}{\sqrt{2}} \quad (1.30)$$

¹³⁰

$$m_Z = \frac{v}{\sqrt{2}} \sqrt{g_1^2 + g_2^2} \quad (1.31)$$

¹³¹ The Higgs field also generates a mass term for the Higgs boson and self-
¹³² interactions for the Higgs boson.

¹³³ 1.1.7 Electroweak Theory

¹³⁴ $SU(2)_L$ generates W^\pm, W^0 gauge bosons, which would be massless if $SU(2)_L$
¹³⁵ was a perfect symmetry. These bosons are massive as this symmetry is broken.
¹³⁶ The mass eigenstates, Z and γ given by:

$$\begin{pmatrix} Z_\mu \\ A_\mu \end{pmatrix} = \begin{pmatrix} \cos\theta_W & -\sin\theta_W \\ \sin\theta_W & \cos\theta_W \end{pmatrix} \begin{pmatrix} W_\mu^3 \\ B_\mu \end{pmatrix} \quad (1.32)$$

¹³⁷ Here θ_W is the Weinberg angle given by:

$$\cos\theta_W = \frac{g_2}{\sqrt{g_1^2 + g_2^2}} = \frac{m_W}{m_Z} \quad (1.33)$$

¹³⁸ 1.1.8 Quantum ChromoDynamics

¹³⁹ As mentioned earlier the Strong Force, which binds the proton together, is
¹⁴⁰ mediated by gluons. Quantum Chromodynamics is the QFT which describes the
¹⁴¹ interactions of quarks and gluons via $SU(3)_C$ symmetry. QCD contains features

¹⁴² not present in Electroweak Interactions due to $SU(3)_C$ generators not commuting
¹⁴³ (a.k.a. $SU(3)_C$ is a non-abelian group). For example, in QCD there is color
¹⁴⁴ confinement and asymptotic freedom due to the structure constants being non-
¹⁴⁵ zero. Requiring $SU(3)_C$ local gauge invariance implies:

$$\psi(x) \rightarrow \psi(x)' = \exp[i g_S \alpha(x) \cdot \hat{T}] \psi(x) \quad (1.34)$$

¹⁴⁶ where $\alpha(x)$ is the local phase function, g_S is the strong coupling constant, and
¹⁴⁷ \hat{T} are the eight generators of $SU(3)$ (note $\hat{T}^a = \frac{1}{2}\lambda^a a$, where λ^a are the Gell-Mann
¹⁴⁸ matrices). As the Gell-Mann matrices are 3x3, this means ψ has three degrees of
¹⁴⁹ freedom under these $SU(3)$ rotations. So we represent ψ under $SU(3)$ rotations
¹⁵⁰ as:

$$\psi = \begin{pmatrix} \psi_{red} \\ \psi_{green} \\ \psi_{blue} \end{pmatrix} \quad (1.35)$$

¹⁵¹ Consequently, particle fields transforming under $SU(3)$ rotations have three
¹⁵² components which physicists describe as color components (red, green, and blue).
¹⁵³ A particle's corresponding antiparticle has the corresponding anticolor. This color
¹⁵⁴ is the "charge" of QCD and is conserved under $SU(3)$ rotations. Combining colors,
¹⁵⁵ color neutral states (e.g. red and antired, or red, green and blue) may be created.
¹⁵⁶ For the Free Dirac Lagrangian to remain invariant under $SU(3)$ transformations,
¹⁵⁷ we must again postulate a boson field that modifies the derivative. The gluon
¹⁵⁸ field tensor is given by ($\alpha = 1, \dots, 8$):

$$G_{\mu\nu}^k = \partial^\mu G_\alpha^\nu - \partial^\nu G_\alpha^\mu - g_S f^{\alpha\beta\gamma} G_\beta^\mu G_\gamma^\nu \quad (1.36)$$

¹⁵⁹ Here $f^{\alpha\beta\gamma}$ are the structure constants of $SU(3)$. Combining all this gives the

₁₆₀ QCD Lagrangian:

$$\mathcal{L}_{QCD} = \bar{\psi}_q i\gamma^\mu (D_\mu)_{ij} \psi^{qj} - m \bar{\psi}_q \psi_q - \frac{1}{4} F_{\mu\nu}^\alpha F^{\alpha\mu\nu} \quad (1.37)$$

₁₆₁ Here i are the color indices, and q are the quark flavors. It is important to
₁₆₂ note that quarks transform under the fundamental representation of $SU(3)$, while
₁₆₃ gluons transform under the adjoint representation. This means quarks carry a
₁₆₄ single color charge (red, green, blue, antired, antigreen, antiblue) and gluons to
₁₆₅ carry a color and anticolor charge.

₁₆₆ Figure 1.3 shows the three dominant QCD interactions. Single gluons carry
₁₆₇ color charge, they interact with one another. This does not occur in QED, as pho-
₁₆₈ tons do not have electric charge and therefore do not interact with each other.
₁₆₉ In QED, a bare electron's effective charge is largest closest to the electron and
₁₇₀ decreases as a function of distance. This is because the QED vacuum fills with
₁₇₁ particle antiparticle pairs spontaneously, which screen the charge of the bare elec-
₁₇₂ tron. The larger the distance from the electron, the smaller the effective charge
₁₇₃ and therefore the weaker the force. So for a pair of electrons, as the distance
₁₇₄ between them increases the repulsive force decreases and they may be observed
₁₇₅ separately.

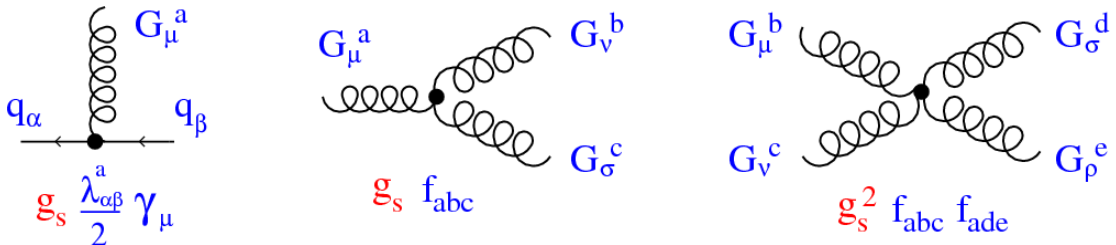


Figure 1.3: This figure shows the three dominant QCD interactions. From Ref. [14]

₁₇₆ Bare quarks and gluons have not been observed. These particles have not

177 been directly observed as they have not been found in isolation. Quarks and
178 gluons group together to form color neutral objects, like baryons and mesons (qqq
179 and $q\bar{q}$, respectively). This is because gluons have color charge and interact with
180 each other. As the distance from a quark increases it's effective color charge
181 increases due to the vacuum polarization in QCD. Color charge grows as the
182 distance from the source increases (a.k.a. color is anti-screened in QCD). A quark's
183 color charge increases with distance, so strong interactions become stronger at
184 large distances (low momenta interactions). At small distances (large momenta
185 interactions) strong interactions are significantly weaker and considered free. This
186 effect of referred to as asymptotic freedom. At large distances, a quark's effective
187 charge is large and the strong force is more significant. This force becomes so
188 strong that quarks form colorless bound states instead of remaining free particles.
189 This effect is known as color confinement. This running of all SM fields is shown
190 in Figure 1.4.

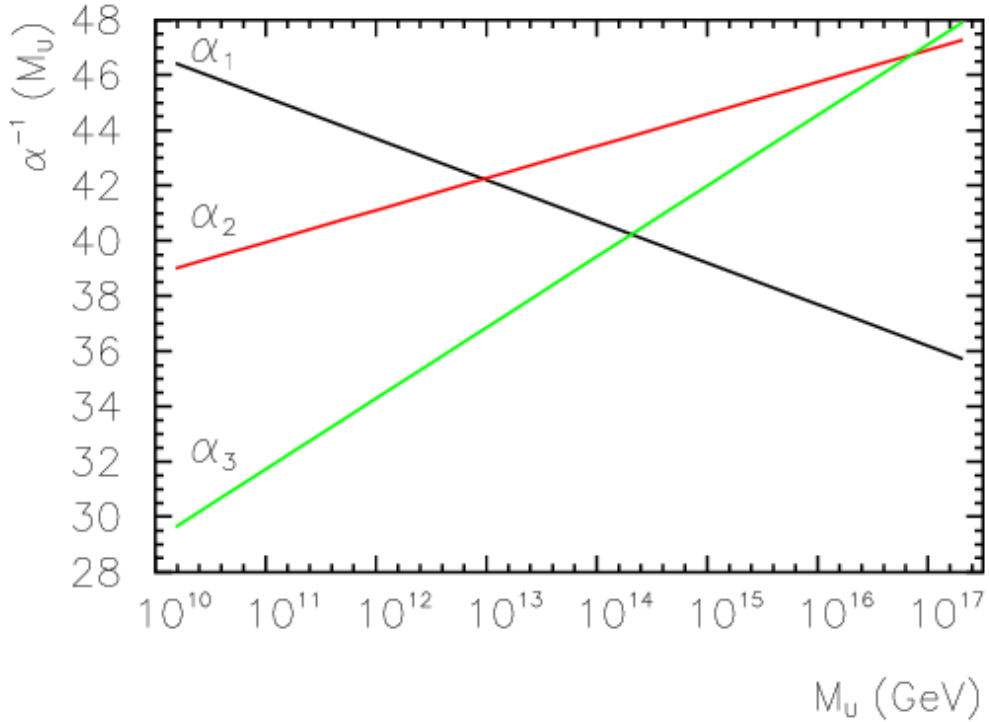


Figure 1.4: Strength of the U(1), SU(2), and SU(3) gauge couplings as a function of the energy scale of the interaction (Q). From Ref. [10]

Commonly the change in a particle's effective charge under a given force is quantified with $\beta(r) \equiv -\frac{de(r)}{d\ln r}$, where $e(r)$ is the effective charge of a given particle under a force. In QED this function is positive but in QCD this function is negative leading to confinement and asymptotic freedom. Moreover, one can calculate how the coupling (α) of a force varies with energies. (More deeply this amounts to incorporating renormalization and vacuum polarization in the boson propagators).

For QCD this is:

$$\alpha_S(x) = \frac{\alpha_S(\mu^2)}{1 + \beta_0 \alpha_S(\mu^2) \ln(Q^2/\mu^2)} \quad (1.38)$$

198

$$\beta_0 = \frac{11N_c - 2n_f}{12\pi} \quad (1.39)$$

199 where Q^2 is the energy level the force is probed at, μ^2 is the renormalization
 200 scale.

201 As stated previously, quarks and gluons have not been observed in isolation.
 202 Instead they form bound colorless states. Hadronization is the process by which
 203 quarks and gluons form hadrons. The process of hadronization is still an active
 204 area of research. One qualitative description is show in Figure BLAH. In this
 205 figure, as two quarks separate the color field between them is restricted to a tube
 206 with energy density of $1\text{GeV}/\text{fm}$. As they separate further, the energy in the color
 207 field increases, until there is enough energy to produce $q\bar{q}$ pairs, which breaks the
 208 color field. This process repeats until quarks and antiquarks have low enough
 209 energy to form colorless hadrons. The resulting spray of hadrons is called a jet.

210 Since quarks and gluons carry different color charges, their respective jets have
 211 different properties. As quarks carry only a single color charge (vs. gluons which
 212 have color and anticolor charge), so their jets have less constituent particles. More
 213 precisely, the Altarelli-Parisi splitting functions [3] contain a factor C_A for gluon
 214 radiation off a gluon and C_F for gluon radiation off a quark ($C_A/C_F = 9/4$).
 215 These color factors are the prefactor in the Feynman diagrams for these processes
 216 [1]. leads to gluon jets having more constituents and therefore more tracks than
 217 quark jets. Gluon jets also tend to have a larger radius with lower momentum
 218 constituents than quarks. There are many novel techniques to distinguish quarks
 219 from gluons. For this study the number of charged particles will be focused on.

220 1.2 Standard Model Successes and Limitations

221 The Standard Model has consistently described much of reality to an extreme
222 degree of accuracy. It has predicted cross sections for strong and electroweak pro-
223 cesses that span over ten order of magnitude correctly [see Fig 1.5] and contains
224 no known logical inconsistencies. Despite the strength and reality of the Stan-
225 dard Model, it still fails to describe aspects of reality and suffers from aesthetic
226 issues. To date, dark matter and energy comprise 95% of the universe, but are
227 not accounted for in the SM. Additionally, neutrinos are known to have mass but
228 are massless in the SM. There are mechanisms for introducing massive neutrinos
229 in the SM, but these mechanisms create hierarchy problems.

230 Possibly the most significant aesthetic issue is the hierarchy between the elec-
231 troweak and Planck scales. The electroweak scale is the scale of electroweak
232 symmetry breaking. The Planck scale is the scale where the gravitational force
233 is comparable in strength to the other forces. (This is also the scale where the
234 gravitational potential energy of two objects separated by a distance r is equal to
235 the energy of a photon with a wavelength r .) The Planck scale is where the SM
236 breaks down, as there is not an experimentally verified theory of quantum gravity,
237 and at this scale gravity cannot be ignored (like it can at the electro-weak scale).
238 These scales differ by ~ 30 orders of magnitude. Understanding this difference in
239 scales would not only explain the weakness of gravity at electroweak scales, but
240 also hopefully lead to a QFT for gravity. (NB: This hierarchy can also be framed
241 in terms of the corrections to the Higgs mass, which depend on the UV cutoff
242 scale - where the SM is suppose to break, which is taken at the Planck scale. This
243 leads the quantum corrections to the Higgs mass to force the Higgs mass to 10^{18}
244 TeV.)

245 These stark contrasts in scales may indicate that a more fundamental theory

exists. It is hoped that such a theory would explain and motivate some of the ad-hoc features of the SM. In particular, there currently are no experimentally verified explanations of why there are three generations of fermions, the values of the 19 SM parameters (6 quark masses, 3 charged lepton masses, 3 gauge couplings, Higgs parameters (μ^2 , λ)), the structure of the fermion representations, etc.

Standard Model Production Cross Section Measurements

Status: July 2018

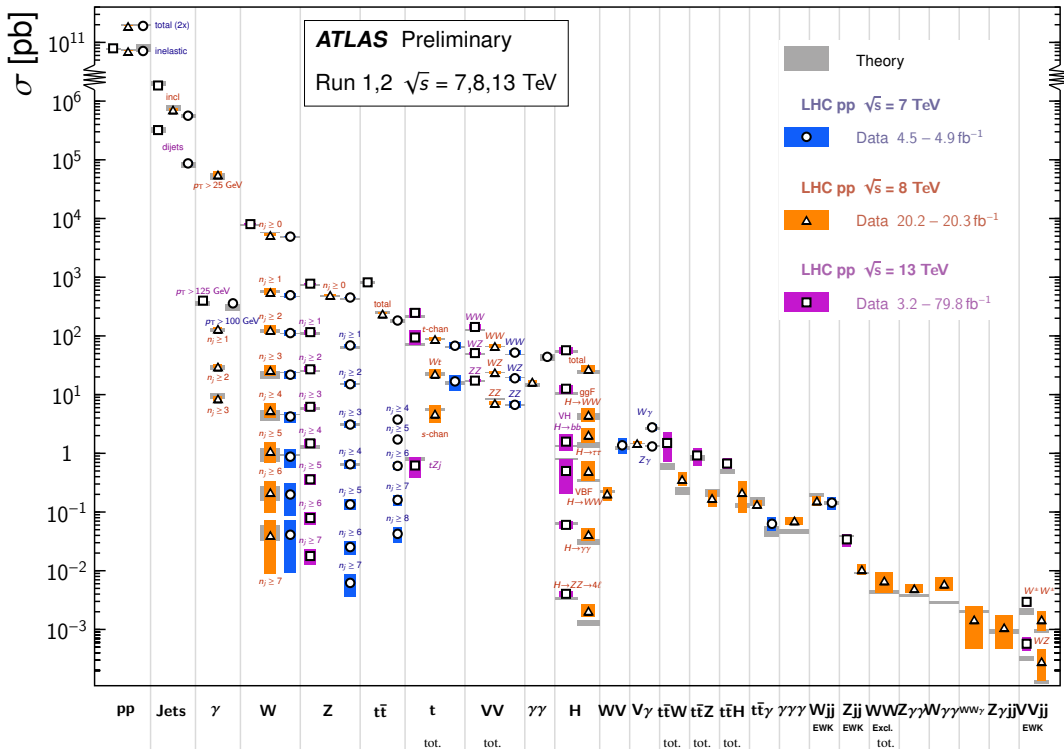


Figure 1.5: A comparison of cross section measurements at $\sqrt{s} = 7, 8, 13$ TeV from ATLAS compared to theoretical measurements. From Ref. [5]

251 **1.3 New Physics Models with Diboson Resonances**

252 **1.3.1 Randall Sundrum Bulk Model**

253 The electroweak-planck hierarchy may be explained by the existence of extra
254 dimensions, like the 5D Randall Sundrum Bulk Model ([15], [2]). In this model,
255 there is one extra warped spatial dimension, y , with a metric:

$$ds^2 = e^{-2k|y|} \eta_{\mu\nu} dx^\mu dx^\nu + dy^2 \quad (1.40)$$

256 where $e^{-k|y|}$ is the warp factor of the extra dimension, which is compactified on
257 a S^1/Z_2 orbifold (a.k.a. a circle where $y \rightarrow -y$). This can be visualized as every
258 point in space time having a line extending from it a distance L , representing
259 this fifth dimension. At the end of this line is the Planck brane. This fourth
260 spatial dimension separates two 4-D branes: Planck brane and TeV brane. We
261 live on the TeV brane, as shown in Figure 1.6. The Higgs field (and to a lesser
262 degree the top quark and graviton fields) is localized near the TeV Brane, while
263 the light fermion fields are localized more near the Planck brane. Fundamental
264 parameters are set on the Planck brane. The warp factor may be scaled away from
265 all dimensionless SM terms by field redefinitions. However, the only dimensionful
266 parameter, $m_H^2 = v^2$ is rescaled by $\tilde{v} \sim e^{-kL} M_{Pl} \sim 1\text{TeV}$ for $kL \sim 35$, explaining
267 why gravity is so weak on the TeV brane. Also, by localizing the light fermion
268 fields near the Planck brane and top and graviton fields near the TeV brane, the
269 light quarks will have smaller masses.

270 The two free parameters of this theory are M_{Pl} and k . Based on this RS Bulk
271 model, all SM particles should have Kaluza-Klein (KK) excitations. In particular,
272 the graviton would have KK excitations that prefer to decay to WW or ZZ, which
273 is why this analysis searches for RS Gravitons.

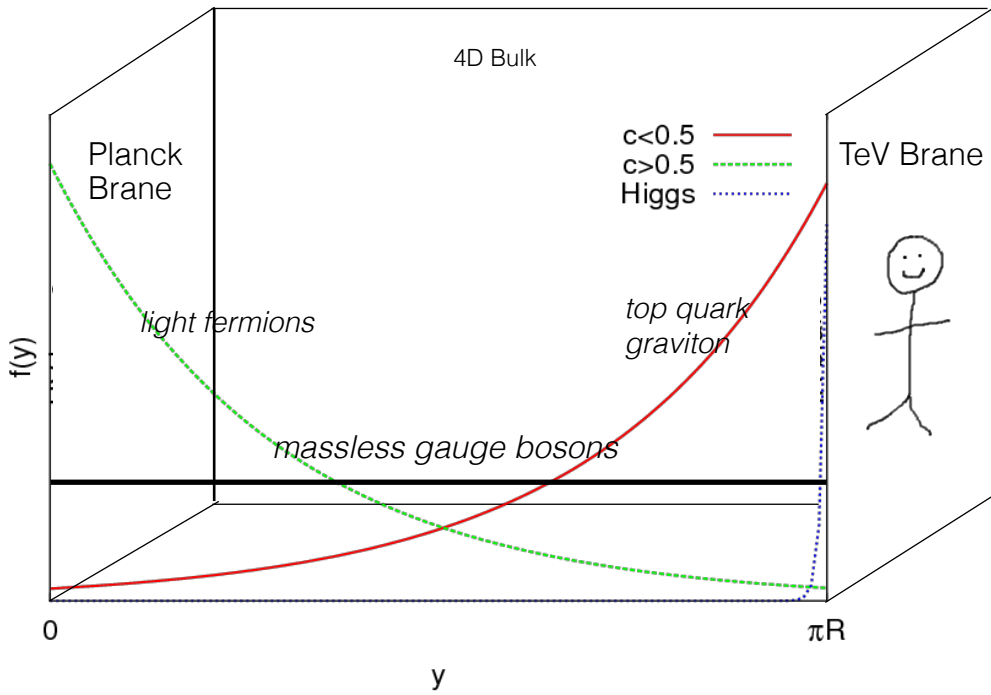


Figure 1.6: Cartoon of RS Bulk Model

274 1.3.2 Extended Scalar Sector

275 A further striking asymmetry of the SM is the simplicity of the scalar sector in
 276 comparison to the boson and fermion sectors. To date, the scalar sector has only
 277 one member, the Higgs boson. Therefore, it is natural to posit an extension to the
 278 scalar sector. From a theoretical standpoint this could also help generate baryon
 279 asymmetry through additional sources of CP violation. This analysis searches for
 280 a simple extension to the scalar sector as proposed in Ref. [16]. The extended
 281 scalar sector includes a real Higgs singlet (S) and complex $SU(2)_L$ doublet (Φ)
 282 (the SM Higgs), where mass eigenstates are mixtures of the fields. S has a vev of
 283 v and Φ has a vev of x . This then gives a Lagrangian of:

$$\mathcal{L} \supset (D^\mu \Phi)^\dagger D_\mu \Phi + \partial^\mu S \partial_\mu S - m^2 \Phi^\dagger \Phi - \mu^2 S^2 + \lambda_1 (\Phi^\dagger \Phi)^2 + \lambda_2 S^4 + \lambda_3 \Phi^\dagger \Phi S^2 \quad (1.41)$$

²⁸⁴ The mass eigenstates of the scalar sector are then mixtures of S and Φ and
²⁸⁵ the free parameters of the theory are m_H , $\sin\alpha$, and $\tan\beta = v/x$. The fields are
²⁸⁶ then given by:

$$\Phi \equiv \begin{pmatrix} 0 \\ \frac{\tilde{h}+v}{\sqrt{2}} \end{pmatrix} \quad (1.42)$$

²⁸⁷

$$S \equiv \frac{h' + x}{\sqrt{2}} \quad (1.43)$$

²⁸⁸ Diagonalizing the mass matrix leads to the mass eigenstates h (discovered
²⁸⁹ Higgs boson) and H (the physical particles):

$$\begin{pmatrix} h \\ H \end{pmatrix} = \begin{pmatrix} \cos\alpha & -\sin\alpha \\ \sin\alpha & \cos\alpha \end{pmatrix} \quad (1.44)$$

²⁹⁰ This suppressed h and H production and SM H couplings:

$$BR_{H \rightarrow SM} = \sin^2\alpha \times \frac{\Gamma_{SM, H \rightarrow SM}}{\Gamma_{tot}} \quad (1.45)$$

²⁹¹ Moreover, in the case that $m_H > m_h$, $H \rightarrow hh$ is possible. This further suppresses
²⁹² $H \rightarrow VV/ff$. This search is most sensitive to $H \rightarrow WW$.

²⁹³ 1.3.3 Simple Standard Model Extensions

²⁹⁴ The RS Bulk model is motivated by resolving the hierarchy problem. Ex-
²⁹⁵ tending the Scalar sector is a natural space to look for new physics due to the
²⁹⁶ complexity of fermion and boson groups. There are many other interesting and

well motivated frameworks, but there is a lack of completely predictive models,
 due to model flexibility (free parameters). Therefore it is hard for experimentalists
 to know which theories to search for in data. However, as seen in 3[13], a "Sim-
 plified Model" approach may be taken. In the search for reasonably narrow width
 particles, as in this search, the search is not sensitive to all the details and free
 parameters of the theory. Generally such searches are only sensitive to the reso-
 nance mass and its interactions. Therefore, a theory's Lagrangian may be reduced
 to only retain this information (mass parameters and couplings). Experimental
 results using this framework may then be reinterpreted in a given theory.

In the simplified approach, a real vector field may be represented under $SU(2)_L$
 with vanishing hypercharge. This results in two charged and one neutral bosons.
 Defined as:

$$V^\pm = \frac{V_\mu^1 \mp i V_\mu^2}{\sqrt{2}} \quad (1.46)$$

$$V_\mu^0 = V_\mu^3 \quad (1.47)$$

The Lagrangian is then:

$$\mathcal{L} \supset -\frac{1}{4} D_{[\mu} V_\nu^a D^{[\mu} V^{\nu]a} + \frac{m_V^2}{2} V_\mu^a V^{a\mu} + ig_V c_H V_\mu^a H^\dagger \tau^a \overset{\leftrightarrow}{D}^\mu H + \frac{g_F^2}{g_V} c_F V_\mu^a J_F^{\mu a} \quad (1.48)$$

In order the terms represent: the kinetic, V mass, Higgs- V interaction, and
 V -left-handed fermion interaction terms. Phenomenologically the three physical
particles this predicts are degenerate, where V couples most strongly to VV , via
the g_V coupling factor. The dominant production modes are DY and VBF.

Two versions of HVT are considered, Model A and B. Model A is a weakly
coupled model where $g_V \ll 1$, like the extended gauge symmetry discussed in Ref .
[16]. Model B is a strongly coupled model, where $1 < g_V < 4\pi$. The width of the

318 resonance grows with g_V so for this narrow resonance search only g_V is chosen to
319 be less than 6 (so $\Gamma/M < 10\%$). More precisely, the coupling of these resonances
320 to fermions scales as $g_f = g^2 c_F/g_V$, where g is the SM $SU(2)_L$ gauge coupling
321 and c_F is the free parameter (expected to be of order 1 for Model A and B). This
322 then means that for Model B the coupling is to fermions is more suppressed than
323 for Model A, leading to a smaller DY production rate and BR to fermionic final
324 states. The coupling of V to SM bosons scales as $g_H = g_V c_H$, where c_H is a
325 free parameter on the order of 1 for Model A and B. So for small values of g_V
326 (i.e. Model A - weakly coupled theories) the BR to gauge boson is smaller than
327 for Model B. So weakly coupled vectors have large production cross sections and
328 decay predominantly to leptons or jets, while strongly coupled vectors are produced
329 less and decay predominantly to gauge bosons.

330 Vectors in Model A and B are generally produced via quark-anti-quark annihi-
331 lation. The more rare production via vector-boson-fusion is considered by setting
332 $g_H = 1$ and $g_F = 0$. In Model B diboson final states are enhanced as stated
333 previously due to g_H and moreover the BR to WZ, WH, WW, and ZH are the
334 same.

335 In summary, V couples most strongly to left-handed fermions and VV depen-
336 dent on g_V .

337 **Chapter 2**

338 **LHC and ATLAS Detector**

339 **2.1 LHC**

340 The Large Hadron Collider (LHC) is the highest-energy particle collider in the
341 world. It was designed to expand the frontier of high energy particle collisions in
342 energy and luminosity. This enables LHC experiments to test the Standard Model
343 and search for new physics at higher energies than tested with previous colliders.
344 Collisions at higher energies not only produce more massive particles but also
345 more weakly interacting particles. Fig. 2.1 shows production cross sections for
346 various processes at hadron colliders. The rate for electroweak physics pcoesses
347 including W and Z scale with the center-of-momentum energy, \sqrt{s} .

348 The LHC consists of a 26.7 km (17 miles) ring, approximately 100 m un-
349 derground, outside Geneva, Switzerland. Counter-circulating proton (and occa-
350 sionally heavy ions) beams collide inside four experiments along the beam line:
351 ATLAS, CMS, LHCb, ALICE. ATLAS and CMS are general purpose detectors
352 designed to explore high energy frontier. LHCb is designed to study the physics
353 of b -quarks. ALICE specializes in studying heavy ion collisions.

proton - (anti)proton cross sections

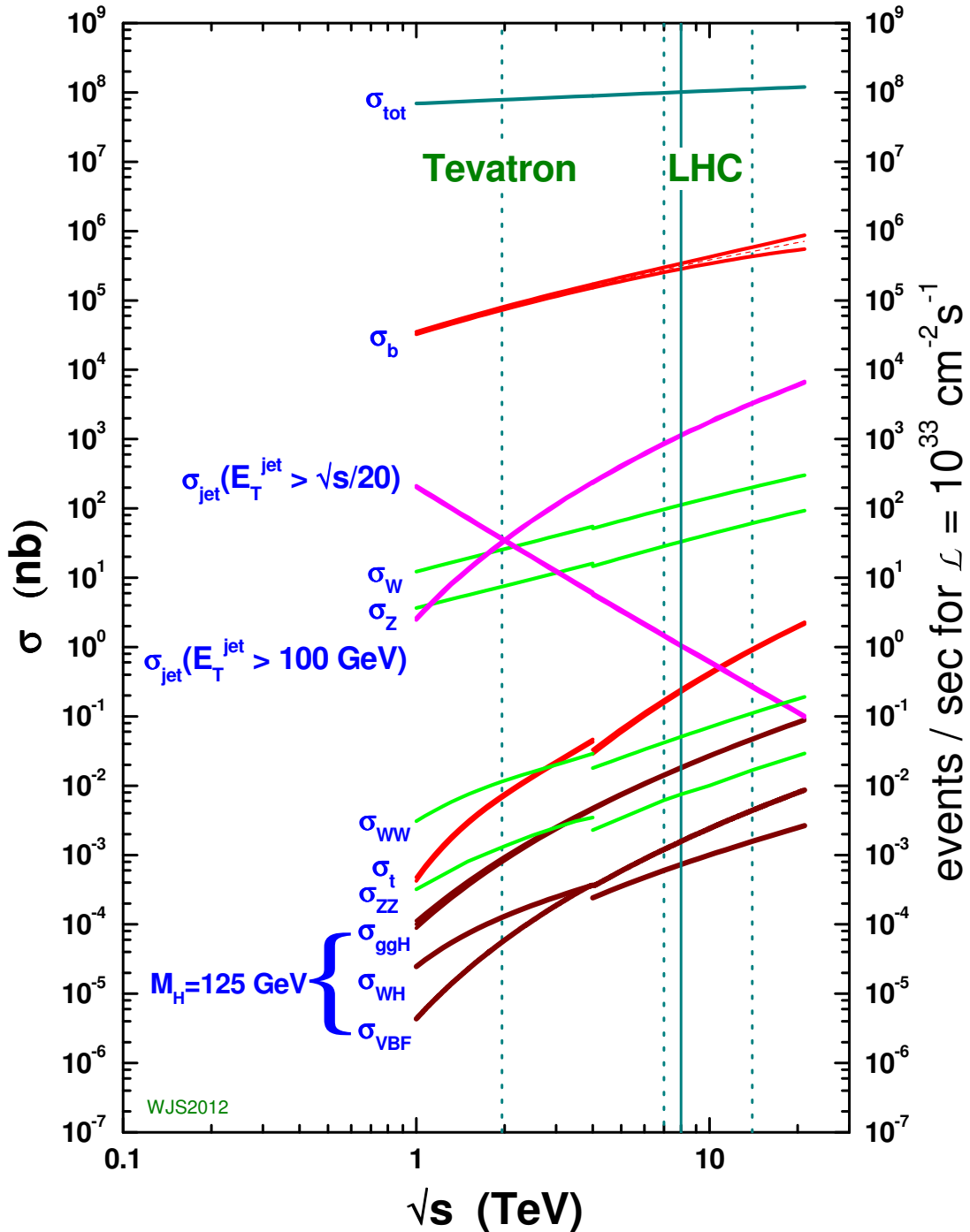


Figure 2.1: Scaling of cross sections with \sqrt{s} . Natasha: write more here

354 The first proton beams circulated in September, 2008. Nine days later an
355 electrical fault lead to mechanical damage and liquid helium leaks in the collider.
356 This incident delayed further operation until November 2009, when the LHC be-
357 came the world's highest energy particle collider, at 1.18TeV per beam. This first
358 operational run continued until 2013, reaching 7 and 8 TeV collision energies. Dur-
359 ing this run a particle who's properties were consistent with the Standard Model
360 Higgs boson was discovered. The next operational began after a two year shut-
361 down after upgrades to the LHC and experiments. This run lasted from 2013 to
362 2018 reaching 13 TeV collision energies. This analysis uses data from the second
363 operational run.

364 **LHC Layout and Design**

365 The layout of the LHC is shown in Figure 2.2. The red and blue lines in the
366 figure represent the counter-circulating proton beams. The LHC is divided into
367 eight octants. Octant 4 contains the RF cavities that accelerate the protons and
368 octant 6 contains the beam dump system. Octants 3 and 7 house the collimation
369 systems for beam cleaning. The beams collide inside the four aforementioned
370 experiments. Each octant contains a curved and straight section. The LHC
371 magnets are built with NbTi superconductors cooled with super-fluid Helium to
372 2K, creating a 8.3T magnetic field to bend the proton beams.

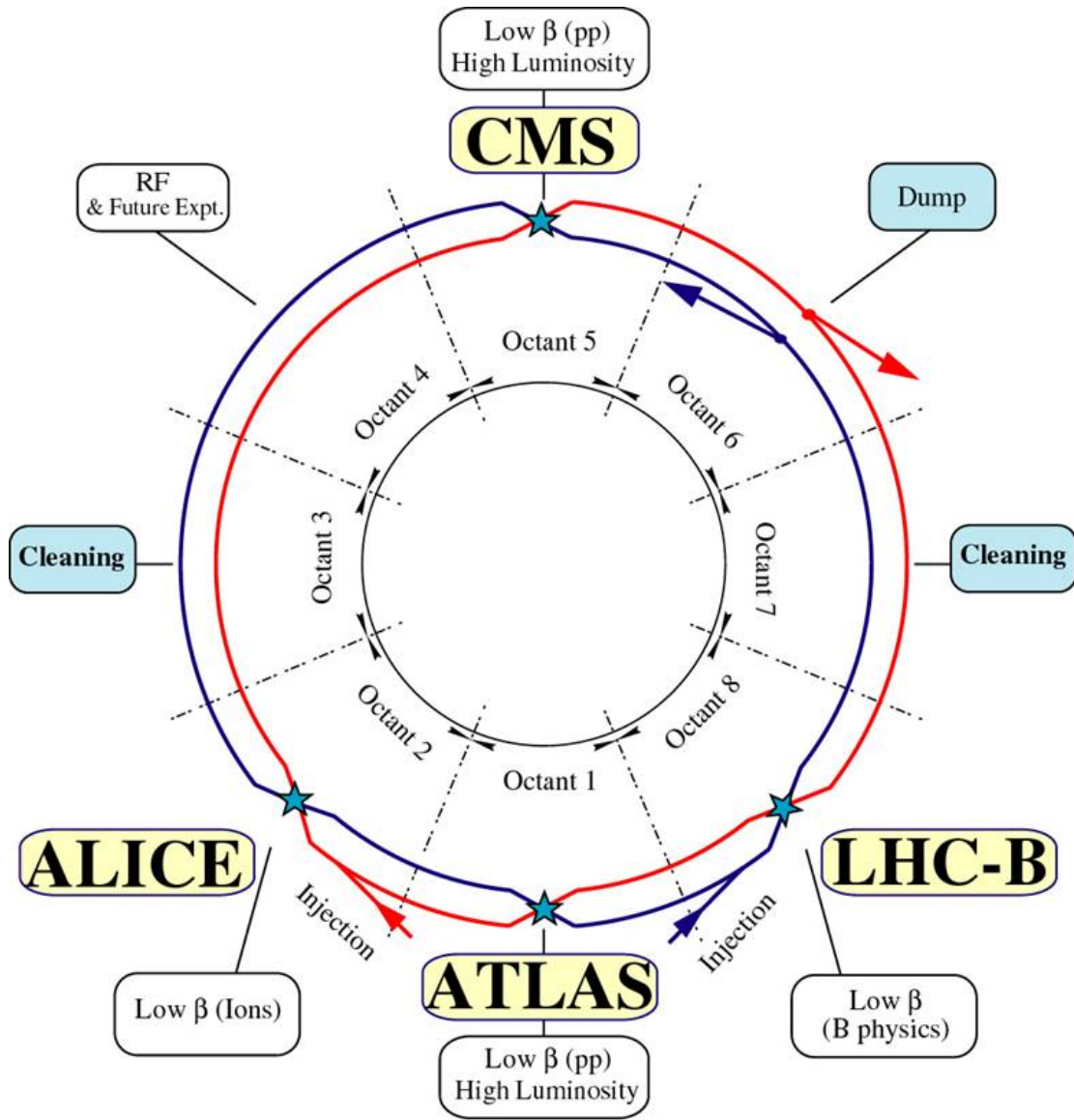
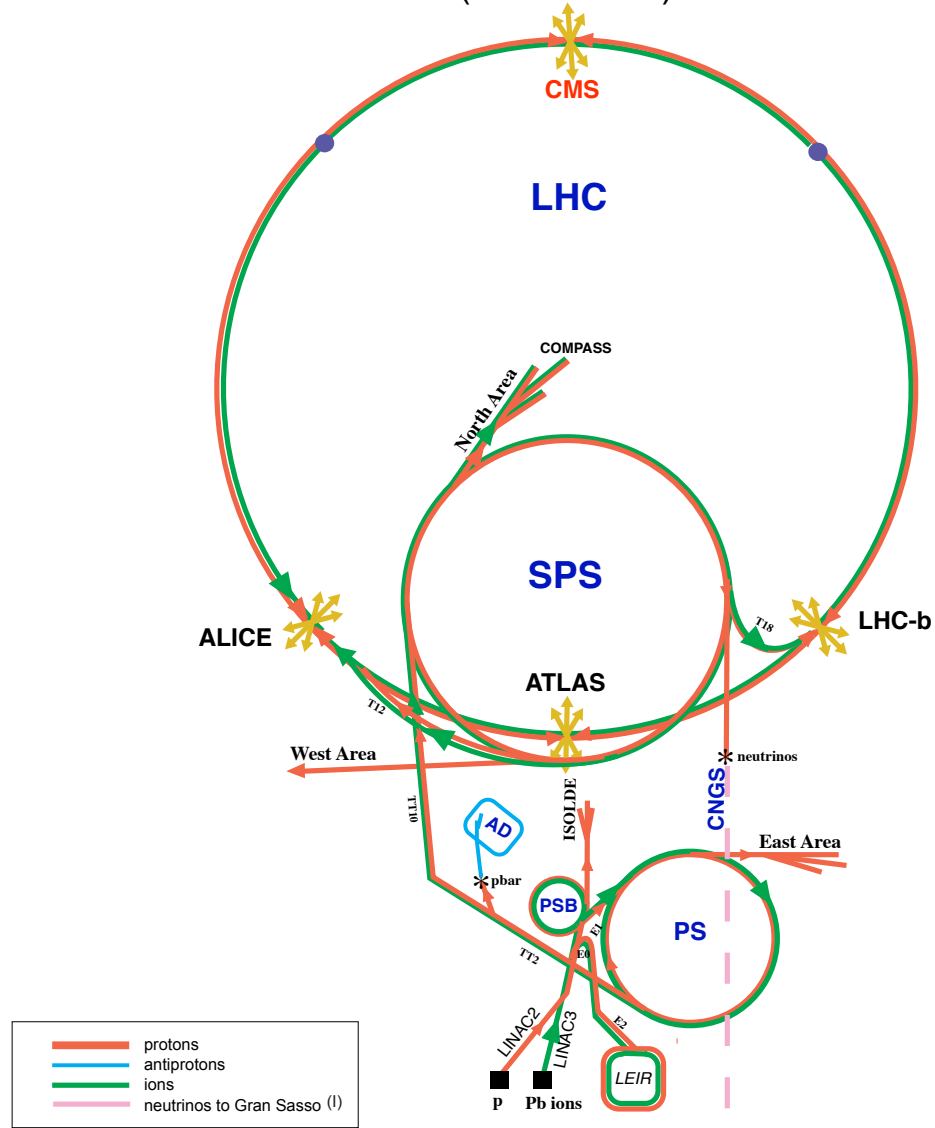


Figure 2.2: LHC Layout. Natasha write more

373 Four sequential particle accelerators are used to accelerate proton from rest as
 374 shown in Figure 2.3. First, Hydrogen gas is ionized to produce protons which
 375 are then accelerated to 50 MeV using Linac 2, a linear accelerator. The result-
 376 ing proton beam is then passed to three circular particle accelerators: Proton
 377 Synchrotron Booster, Proton Synchrotron, and Super Proton Synchrotron (SPS),

³⁷⁸ accelerating protons to 1.4, 25, and 450 GeV, respectively. Once the protons exit
³⁷⁹ SPS, they are injected into the LHC at octant 2 and 8. Each proton bunch contains
³⁸⁰ 10^{11} protons. The spacing between bunches is 25 ns, which means each beam con-
³⁸¹ tains 3564 bunches. However, some bunches are left empty due to injection and
³⁸² safety requirements, yield 2808 bunches per beam. Once the proton beams are
³⁸³ injected they are accelerated to 13 TeV.

CERN Accelerators (not to scale)



LHC: Large Hadron Collider

SPS: Super Proton Synchrotron

AD: Antiproton Decelerator

ISOLDE: Isotope Separator OnLine DEvice

PSB: Proton Synchrotron Booster

PS: Proton Synchrotron

LINAC: LINear ACcelerator

LEIR: Low Energy Ion Ring

CNGS: Cern Neutrinos to Gran Sasso

Rudolf LEY, PS Division, CERN, 02.09.96
Revised and adapted by Antonella Del Rosso, ETT Div.,
in collaboration with B. Desforges, SL Div., and
D. Manglunki, PS Div. CERN, 23.05.01

Figure 2.3: LHC Accelerator. Natasha write more

384 As many new physics models predict cross-sections below the weak scale it was
385 important to design the LHC to be capable of collecting enough data, by running
386 in high luminosity conditions. The machine luminosity depends only on beam
387 parameters:

$$L = \frac{N_p^2 f}{4\epsilon\beta^*} F \quad (2.1)$$

388 where N_p is the number of protons per bunch, f is the bunch crossing frequency,
389 ϵ is the transverse beam emittance, β^* is the amplitude function at the collision
390 point, and F is the geometric luminosity reduction factor due to the beams crossing
391 at an angle (rather than head-on).

392 This analysis uses data from Run 2, totally 139/fb. The peak luminosity was
393 [Natasha add info here]. [Natasha add lumi and integrated lumi figures].

394 2.2 The ATLAS Detector

395 The ATLAS detector measures the position, momentum and energy of parti-
396 cles produced in the proton collisions by using magnetic fields, silicon detectors,
397 sampling calorimeters, and gaseous wire detectors. It is located approximately
398 100 m underground at Point-1 around the LHC beam line and weighs 7000 metric
399 tons. The detector is 46 m long, 25 m high, 25 m wide as shown in Figure 2.5.
400 The detector can be divided into three subsystems: the Inner Detector (ID), the
401 Calorimeters, and the Muon Spectrometer (MS). Figure 2.6 shows an overview of
402 how different particles interact in the detector.

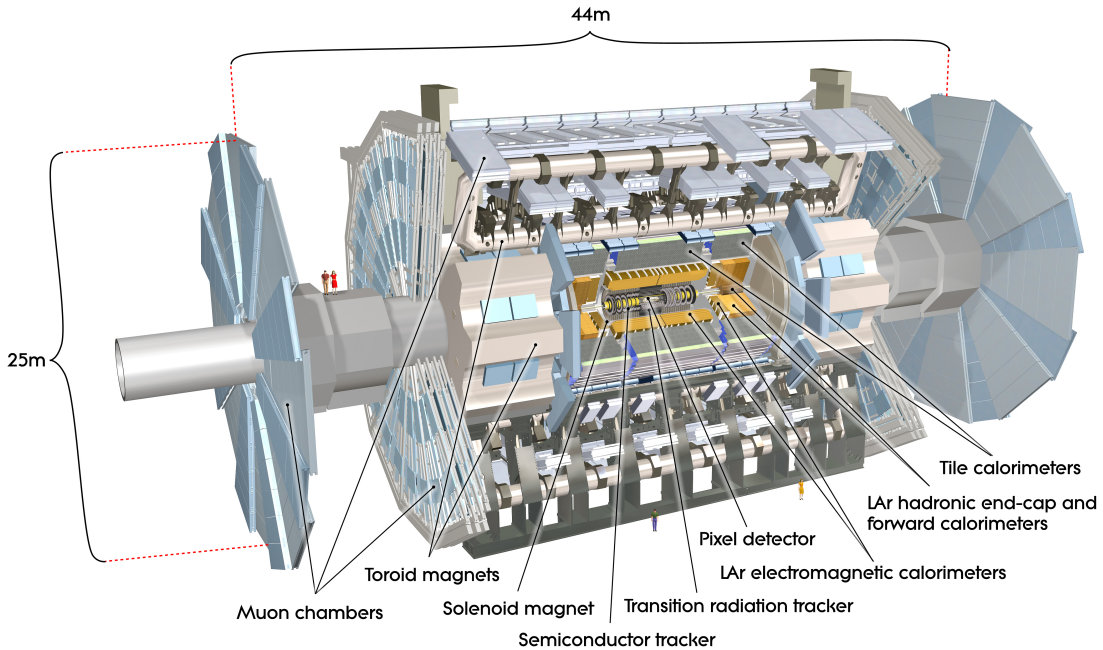


Figure 2.4: Big picture layout of ATLAS detector. Natasha: write more

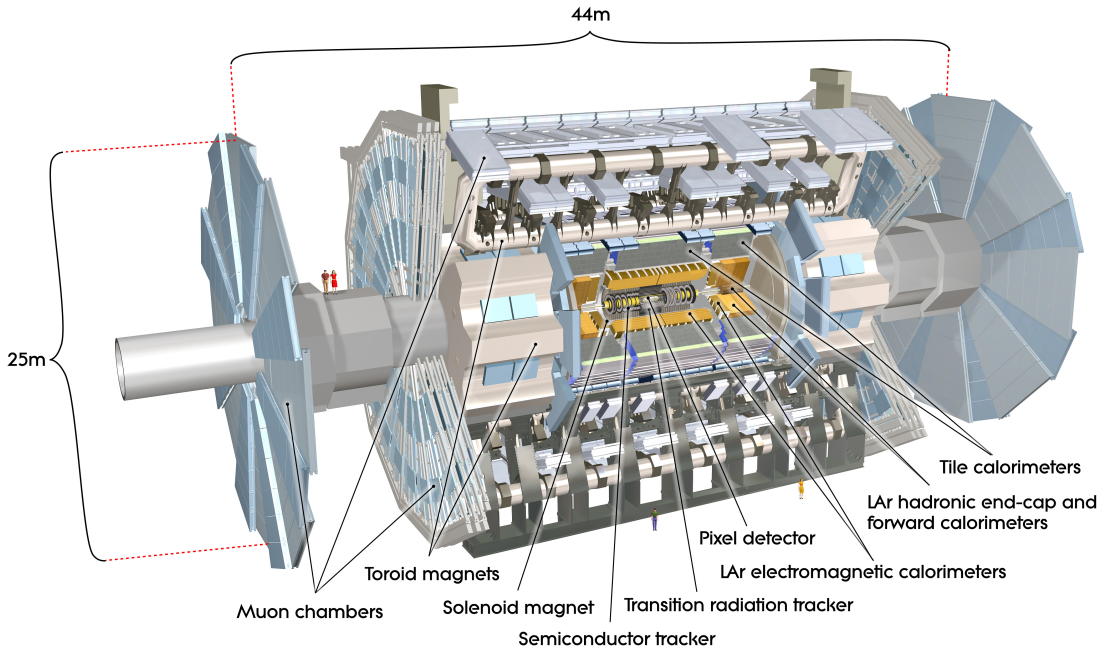


Figure 2.5: Big picture layout of ATLAS detector. Natasha: write more

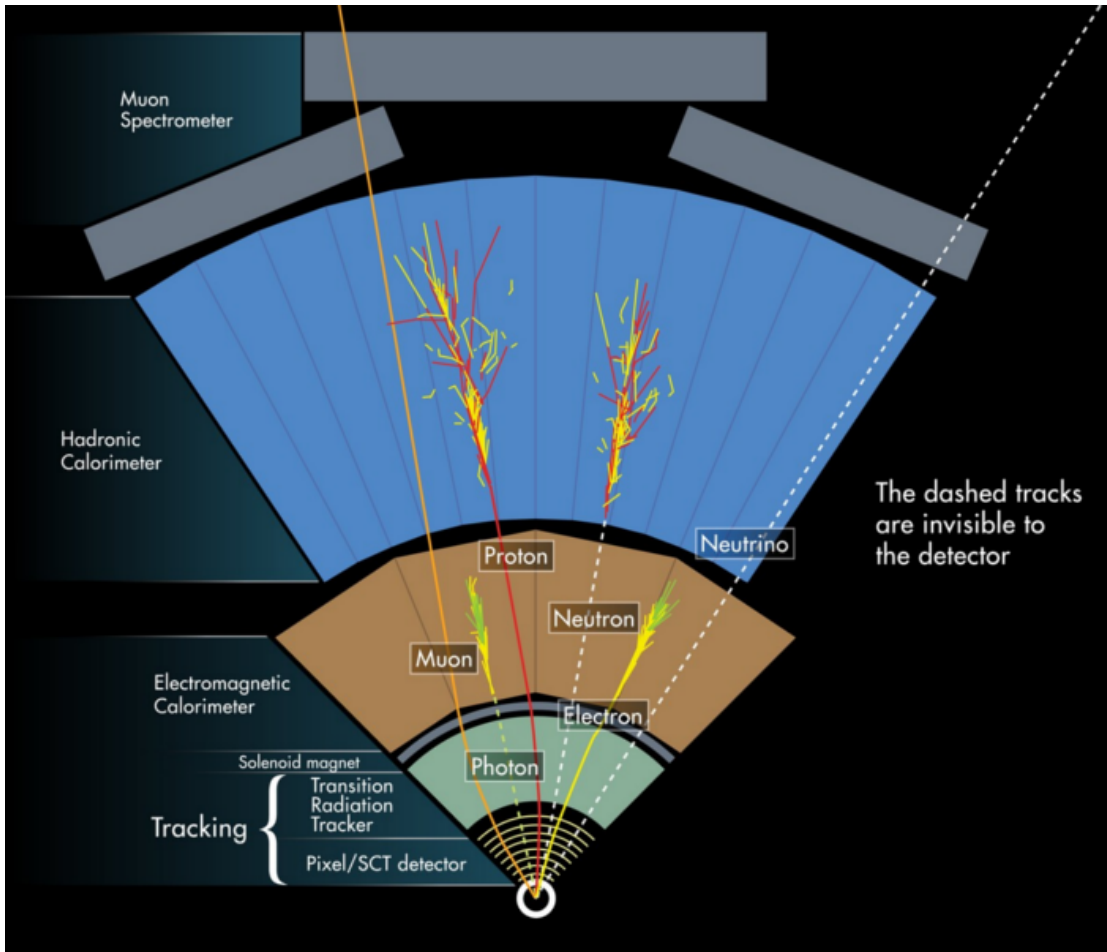


Figure 2.6: A simplified schematic of how different particles interact and are detected within ATLAS.

403 2.2.1 Coordinate System

404 The trajectory of particles within ATLAS is measured relative to the nominal
 405 interaction point. The z -axis points along the beam line, such that when the
 406 LHC is viewed from above, the counter-clockwise circulating beam points along
 407 the positive- z direction. The $x - y$ plane is transverse to the beam line, with
 408 the positive x -axis pointing towards the center of the LHC ring. The positive
 409 y -axis points vertically upward. The azimuthal angle, ϕ , is the angular distance

about the z -axis, with $\phi = 0$ along the x -axis. The polar angle from the z -axis is denoted as θ . The polar angle is usually replaced by pseudo-rapidity, $\eta = -\ln \tan(\frac{\theta}{2})$. Pseudo-rapidity is preferred as $\Delta\eta$ is invariant under boosts along z and particle production is approximately invariant under η . Angular separation between particles in ATLAS are given by $\Delta R = \sqrt{\Delta\eta^2 + \Delta\phi^2}$. The distance from the beamline is given by $r = \sqrt{x^2 + y^2}$

2.3 Inner Detector

The Inner Detector (ID) was designed to identify and reconstruct vertices, distinguish pions from electrons, and measure the momentum of charged particles. The ID uses three different technologies for particle reconstruction: the Pixel Detector, Semiconductor Tracker (SCT), and the Transition Radiation Tracker (TRT), shown in Figure 2.7 and 2.8. The entire ID is immersed in a 2T solenoidal magnetic field parallel to z , causing charged particles to bend in the transverse-plane, allowing particle momentum measurements.

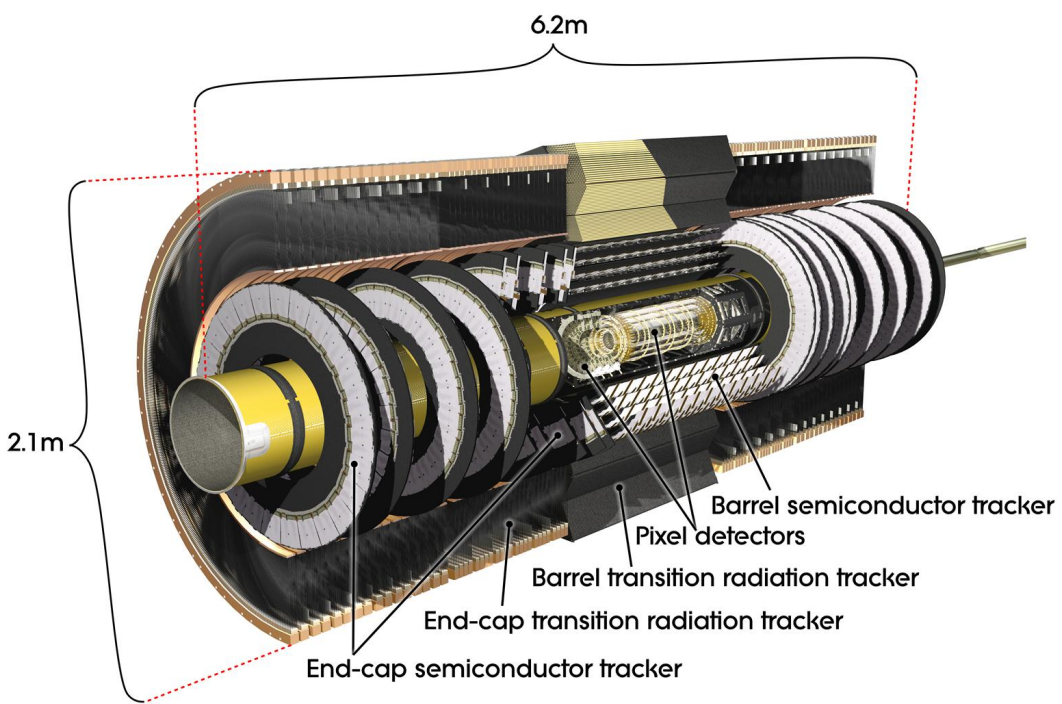


Figure 2.7: Layout of ATLAS Inner Detector

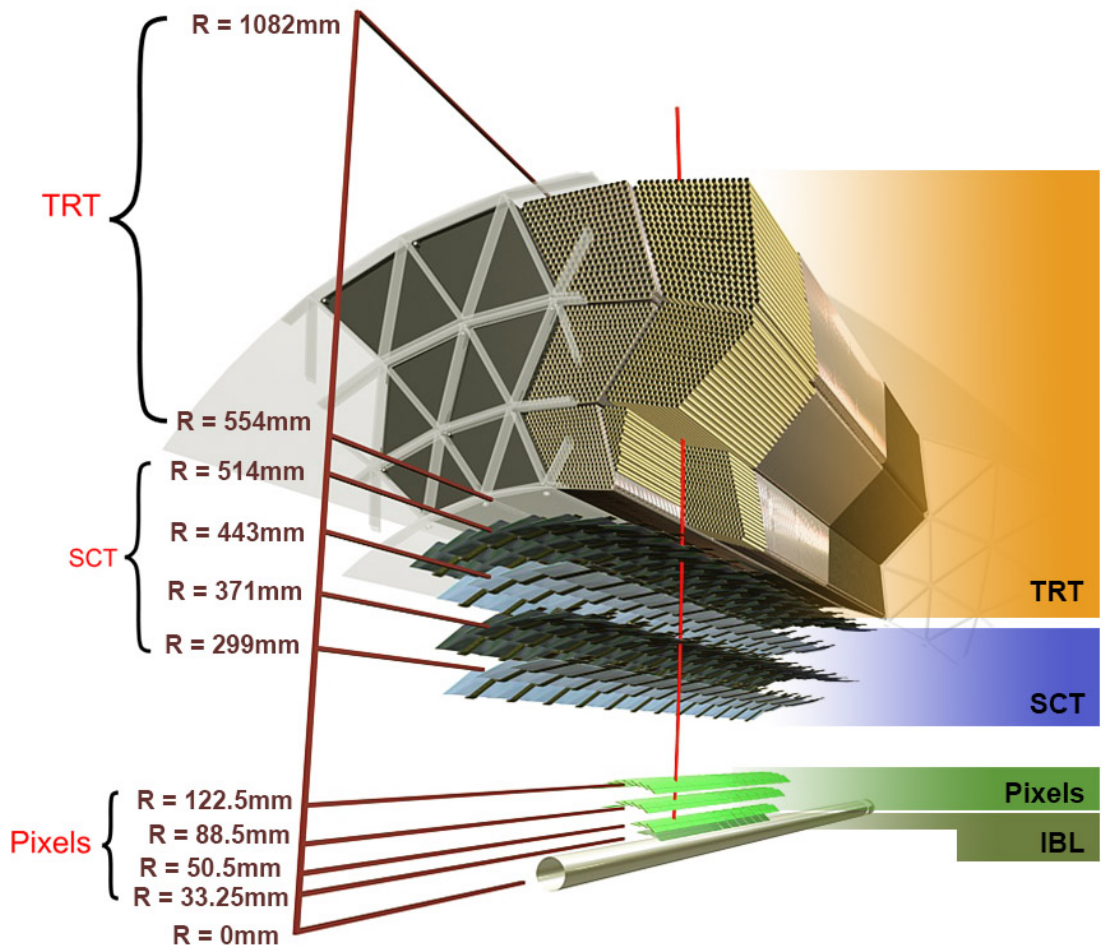


Figure 2.8: Layout of ATLAS ID Barrel System.

424 **2.3.1 Pixel Detector**

425 The pixel detector consists of four barrel layers between $r = 32.7$ and 122.5
426 mm, extending to $|z| = 400.5$ mm. The innermost pixel barrel, the Insertable
427 b-Layer (IBL), only extends to $|z| = 332$ mm. The pixel detectors closer to the
428 beam line (larger η values) consists of six parallel cylindrical rings of pixel de-
429 tectors transverse to the beam line. The entire pixel detector consists of 1744
430 identical pixel sensors each with 46080 readout channels, totaling about 80 mil-
431 lion individual pixels. Most of the pixel sensors are $50 \times 400 \mu\text{m}^2$. The intrinsic
432 measurement accuracy of a individual pixel detector in the barrel (end-cap) in
433 $r - \phi$ is $10 \mu\text{m}$ and $115 \mu\text{m}$ in $z(r)$.

434 **2.3.2 Semiconductor Tracker**

435 The SCT is located outside the pixel detector and has the same barrel and
436 endcap geometry as the pixel detector. SCT sensors are $80 \mu\text{m} \times 12$ cm ($80 \mu\text{m}$
437 strip pitch). In the barrel the strips are parallel to the z -axis and are segmented
438 in ϕ . In the endcaps, the strips extend radially. Sensors are grouped in modules
439 containing two layers of strips rotated 40 mrad with respect to each other. This
440 offset allows for the two-dimensional position of a track to be determined by
441 identifying the crossing point of the strips that registered a hit. SCT modules
442 measure tracks with an accuracy of $17 \mu\text{m}$ in $r - \phi$ and $580 \mu\text{m}$ in $z(r)$ in the
443 barrel (end-cap) region.

444 **2.3.3 Transition Radiation Tracker**

445 The transition radiation tracker (TRT), enveloping the SCT, is a gaseous
446 straw-tube tracker mainly used for electron/pion track separation. Each straw
447 is 4 mm in diameter and filled with a Xe- CO_2 - O_2 gas mixture. An anode wire at

448 the center of the straw is held at ground potential, while the walls of the straw are
449 kept at -1.4kV. When a charged particle passing through the TRT ionizing the
450 gaseous mixture, and the resulting ions form an avalanche on the anode wire with
451 a grain of 10^4 . The resulting signal from the anode wire is then digitized and
452 amplified. Signals passing a low threshold cutoff are used to distinguish noise from
453 tracks. Signals passing a high threshold cutoff are sensitive to transition radiation
454 (TR). TR photons are emitted when charged particles pass between materials
455 with different dielectric constants. The probability that a charged particle with
456 energy E and mass m passing between two materials emits a TR photon in the keV
457 range is proportional to $\gamma = E/m$. In the TRT straws these often then convert via
458 the photoelectric effect, causing a large avalanche triggering the high-threshold.
459 Since electrons have a smaller mass than pions, tracks from electrons are more
460 likely to trigger the high threshold. Consequently, the high threshold TRT trigger
461 provides electron identification information that is uncorrelated with calorimeter
462 shower-shape information.

463 The barrel region of the TRT extends from $r = 563\text{-}1066$ mm and $|z| < 712$
464 mm. Barrel Straws are 144 cm long (divided $\eta \approx 0$) and orientated parallel to
465 the beam direction. End-cap straws extend radially and are 37 cm long. There
466 are 53,544 straws in the barrel and 160,000 straws in the end-caps. Radiator mats
467 of polypropylene/polyethylene fibers in the barrel are aligned perpendicular to the
468 barrel straws (with holes for the straws to pass through). In the end-cap region,
469 radiator foils are layered between the radial TRT straws.

470 The width of the signal pulse is sensitive to the distance between the charged
471 particle track and the anode wire and allows for a hit resolution of $130\mu\text{m}$. The
472 TRT extends to $|\eta| = 2.0$ and provides about 36 hits per track.

473 2.4 Calorimeters

474 The ATLAS electromagnetic and hadronic calorimeters (EMC and HCAL,
475 respectively) absorb and measure the energy of high energy hadrons, photons,
476 and electrons with $|\eta| < 4.9$. Both systems use sampling calorimeters which
477 consist of alternating layers of dense absorbing and active layers. In the absorbing
478 layer particles interact and lose energy, creating showers. These showers are then
479 detected and measured in the active layer. The amount of charge measured in the
480 active material scales with the energy of the incident particle, and thus provides a
481 measurement of the particle's energy. An overview of the layout of the calorimeter
482 system is shown in Figure 2.9.

483 The EMC measures and contains the energy of electromagnetically interacting
484 particles with 170k channels. It consists of layered accordion-shaped Lead ab-
485 sorber plates and electrodes immersed in liquid Argon. Using accordion-shaped
486 electrode and absorbers ensures ϕ symmetry and coverage. The EMC is com-
487 posed of a barrel part ($|\eta| < 1.475$), two end-caps ($1.375 < |\eta| < 3.2$), and a
488 presampler ($|\eta| < 1.8$). The presampler, containing only liquid Argon, corrects
489 for upstream energy losses of electrons and photons. The EMC barrel is segmented
490 into three layers. The first layer has finest segmentation with readout cells ex-
491 tending $\Delta\eta \times \Delta\phi = 0.025/8 \times 0.1$. This provides a precise shower measurements
492 used to separate prompt photons from $\pi^0 \rightarrow \gamma\gamma$ decays. The second layer has
493 coarser segmentation and is approximately 16 radiation lengths long. A radiation
494 length is the average distance an electron travels before losing all but $1/e$ of its
495 energy to bremsstrahlung. The last layer is the most coarse and measures the tail
496 of the electromagnetic shower. A schematic of the ECAL is shown in Figure ??.

497 The hadronic calorimeter located outside the EMC and is used to contain
498 and measure the energy of hadronically interacting particles. It consists of a tile

499 calorimeter (TileCal), hadronic end-cap calorimeter (HEC), and liquid Argon for-
 500 ward calorimeter (FCAL). TileCal is located behind the LAr EMC and uses steel
 501 absorbers and liquid Argon as the active material. TileCal consists of three barrel
 502 layers in the central and forward regions, extending up to $|\eta| < 1.7$. Radiated
 503 photons from the steel tiles are collected via wavelength-shifting fibers connected
 504 to photomultiplier tubes, as shown in Figure 2.11. The HEC lies behind the EMC
 505 endcap wheels. It uses copper absorbers and liquid Argon as the active material
 506 and covers $1.5 < |\eta| < 3.2$. Finally, the FCAL covers $3.1 < |\eta| < 4.9$ and consists
 507 of three modules all using liquid Argon as the active material. The first module
 508 uses copper absorber and was designed for electromagnetic measurements. The
 509 second and third modules consist of tungsten absorber and are used to measure
 510 the kinematics of hadronically interacting particles. A schematic of the HCAL is
 511 shown in Figure 2.11.

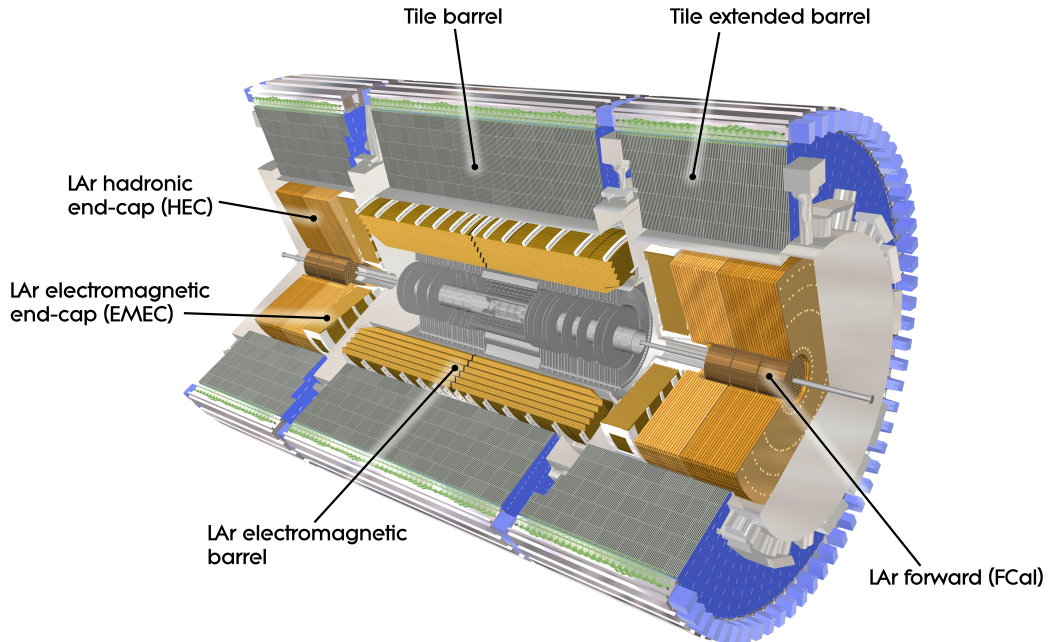


Figure 2.9: Overview of ATLAS electromagnetic and hadronic calorimeters.

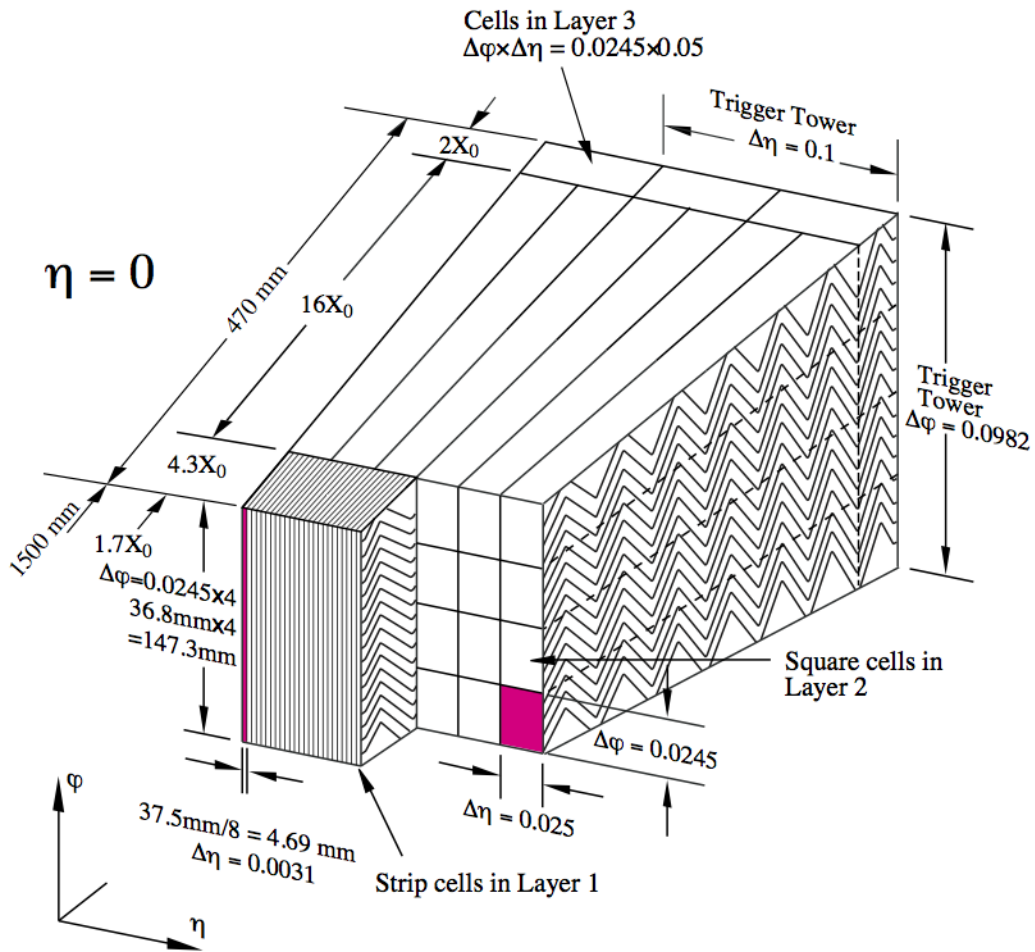


Figure 2.10: Schematic of ECAL.

Figure 2.11: Schematic of HCAL.

512 The energy resolution of the calorimeter subsystems are:

513
$$\frac{\sigma_E}{E} = \frac{10\%}{\sqrt{E}} \oplus 0.7\% \text{ EMC}$$

514
$$\frac{\sigma_E}{E} = \frac{50\%}{\sqrt{E}} \oplus 3\% \text{ hadronic barrel -Natasha check if barrel and end-cap truly}$$

515 have same energy resolution

516
$$\frac{\sigma_E}{E} = \frac{50\%}{\sqrt{E}} \oplus 3\% \text{ hadronic end-cap}$$

517
$$\frac{\sigma_E}{E} = \frac{100\%}{\sqrt{E}} \oplus 10\% \text{ hadronic end-cap}$$

518 2.5 Muon Spectrometer

519 The muon spectrometer (MS) is the outermost detector system in ATLAS.
520 Muons with a $p_T > 4$ GeV are energetic enough to reach the MS. To measure the
521 momentum of these muons two barrel and end-cap toroid magnets are used covering
522 $|\eta| < 1.4$ and $1.6 < |\eta| < 2.7$. For $1.4 < |\eta| < 1.6$, a combination of the barrel
523 and end-cap toroidal magnetic fields bend muon trajectories. The detector in the
524 barrel region form three concentric rings at $R = 5, 7.5, 10$ m and are segmented
525 in ϕ to accommodate the magnets. The end-cap region consists of three circular
526 planes perpendicular to z and located at $|z| = 7.4, 14, 21.5$ m from the interaction
527 region. An additional detector at $|z| = 10.8$ m covers the transition region between
528 the barrel and end-cap.

529 The MS consists of four subsystems: Monitored Drift Tubes (MDT), Cathode
530 Strip Chambers (CSC), Resistive Plate Chambers (RPC), and Thin Gap Cham-
531 bers (TGC). The first two subsystems are used primarily for measuring muon track
532 parameters, while the RPC and TGC subsystems are used for muon triggering.
533 A schematic of this system is shown in Figure 2.12.

534 The MDT subsystem consists of precision tracking chambers for $|\eta| < 2.7$,
535 except for the inner most end-cap layer ($2.0 < |\eta| < 2.7$), where CSCs are used.
536 The basic unit of MDT chambers are thin walled Aluminum tubes with a diameter
537 of 3 cm and length of 0.9-6.2 m. These tubes are filled with a mixture of Ar-CO₂
538 gas with a 50μm W-Rn wires running down the center of the tube which is kept at
539 3080 V. Since the maximum drift time of these chambers is 700 ns, they are not
540 used for triggering. MDT chambers consist of 3-4 layers of tubes mounted on a
541 rectangular support system, as seen in Figure 2.13, orientated along ϕ to measure
542 the coordinate in the bending plane of the magnetic field with a resolution of 35
543 μm.

544 The MDT subsystem can only handle hit rate below $150\text{Hz}/\text{cm}^2$. For this
545 reason, CSCs are used in the innermost end-cap layer where hit rates are larger.
546 CSCs can handle hit rates up to $1000\text{Hz}/\text{cm}^2$. CSC are multiwire proportional
547 chambers. These chambers are filled with a Ar- CO_2 gas mixture and evenly spaced
548 wires kept at 1900 V. These wires are orientated in the radial direction but not
549 read out. Instead on one side of the cathode are copper strips parallel to the wires,
550 measuring η , while on the other side of the cathode are strips parallel to the wires
551 measuring ϕ . The width between strips is approximately 1.5 mm providing a
552 resolution of $60\ \mu\text{m}$ in the bending-plane and 5 mm in the non-bending plane.

553 Since the CSC and MDT systems do not poor time resolution, the RPC and
554 TGC systems are used for triggering. The RPC system is used in the barrel region
555 ($|\eta| < 1.05$). RPC consist of two parallel resistive plates separated by a 2 mm
556 insulated spacer with 100 mm spacing kept at 9.8 kV 2.14. A gaseous mixture of
557 $\text{C}_2\text{H}_2\text{F}_4$, C_4H_{10} , and SF_6 fills the space between the two plates. Metallic strips
558 on the outer faces of the plates are used to read out signals produced by the
559 gas ionizing. The middle barrel layer consists of two layers of RPCs on either
560 side of the MDT layer and one layer on the outermost MDT layer. Each layer
561 contains two orthogonal sets of metallic strips providing η and ϕ measurements.
562 The timing resolution of RPCs is 1.5 ns, and therefore may be used to identify
563 bunch crossings.

564 Finally, the TGCs are used in the end-cap regions and primarily used to pro-
565 vide L1 trigger decisions and ϕ measurements. TGCs are multi-wire proportional
566 chambers consisting of arrays of gold-coated tungsten wires placed between two
567 cathode planes. These wires are separated by 1.8 mm and cathodes are 1.4 mm
568 from the wires. Orthogonal to the wires, on the opposite side of the cathode plane
569 are copper strips held at 2900 V. The chambers are filled with a mixture of CO_2

570 and n-pentane gas, the latter acts as a quenching gase to prevent avalances initiated
571 by secondary γ -rays from the primary avalanche. Figure 2.15 is a schematic
572 of a TGC. The timing resolution of TGCs is less than 25 ns and therefore are used
573 for bunch crossing measurements.

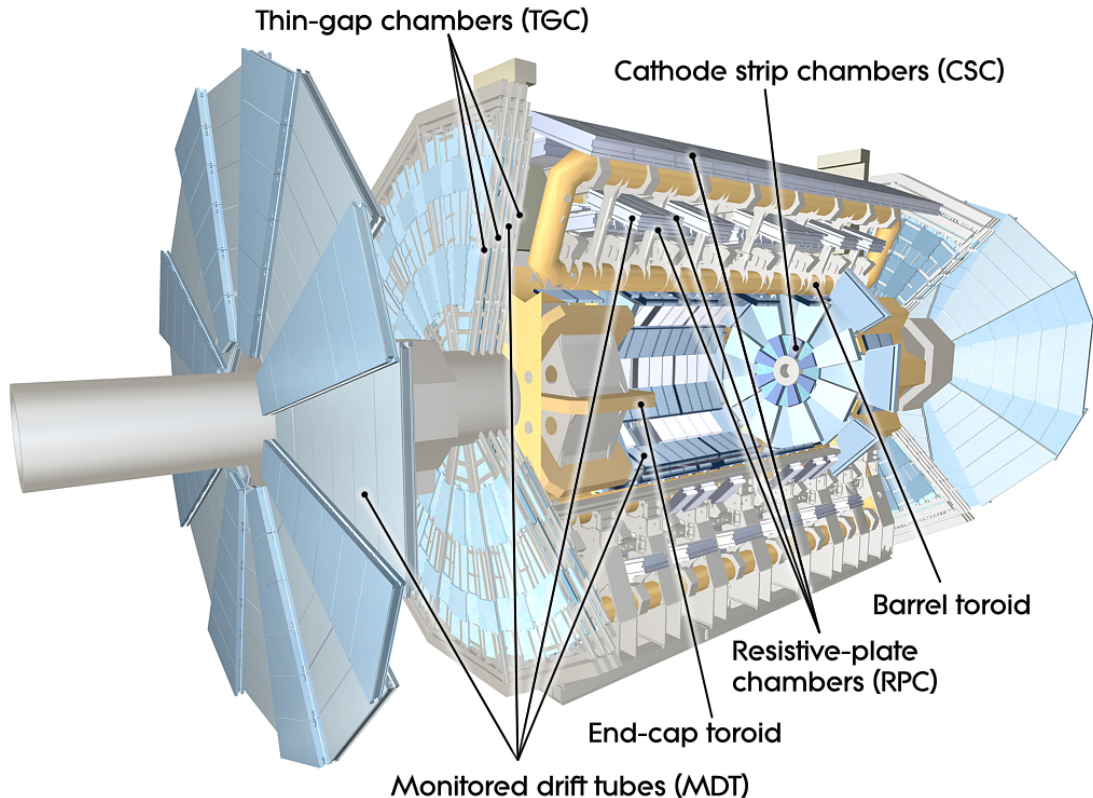


Figure 2.12: Schematic of Muon Spectrometer [cite G35]

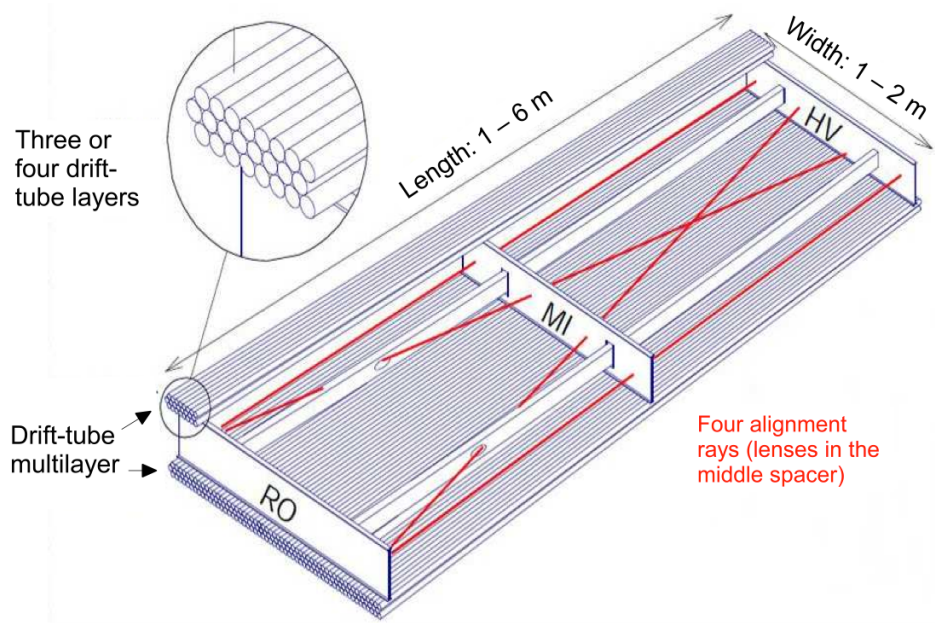


Figure 2.13: Schematic of MDT chamber. [cite G35]

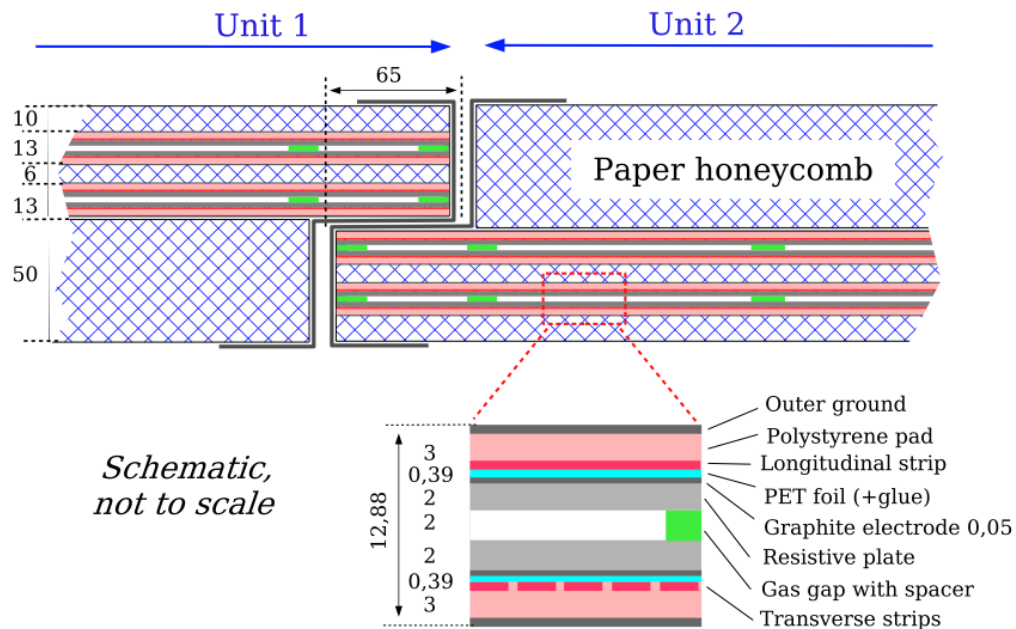


Figure 2.14: Schematic of RPC chamber, which is used for triggering in the central region of the detector [cite G35].

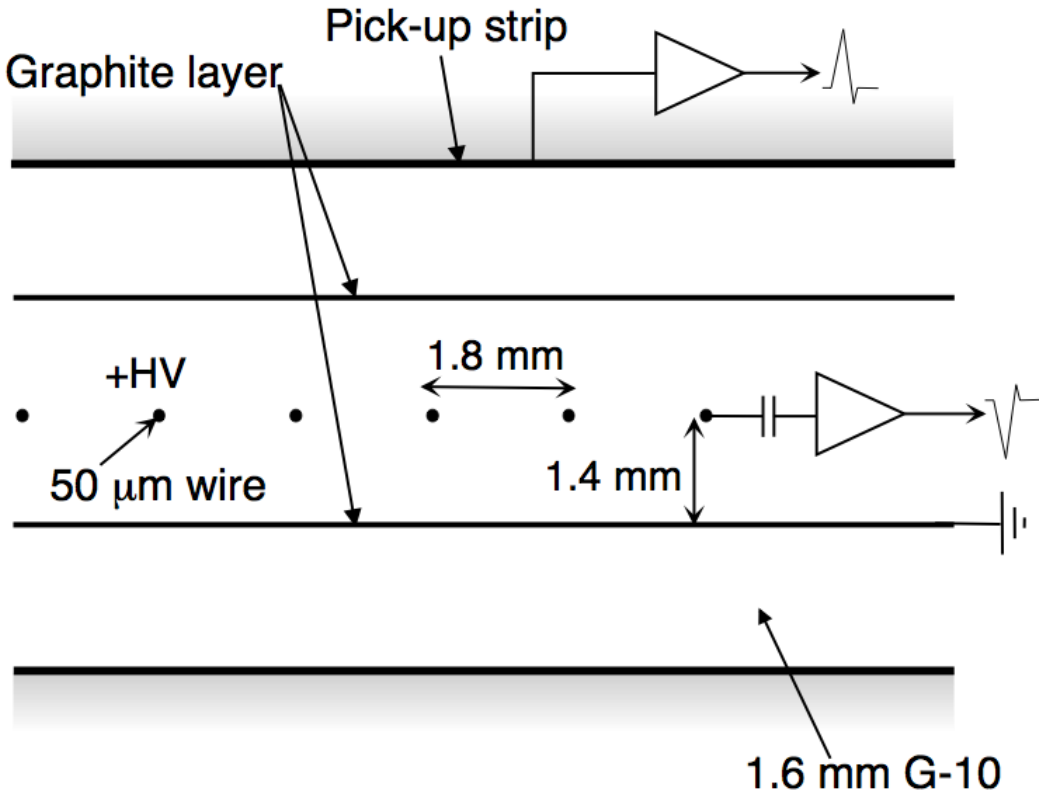


Figure 2.15: Schematic of TGC chamber, which is used for triggering in the muon end-cap region. [cite G35]

574 2.6 Magnet System

575 A particles with charge, q , and velocity v , moving in magnetic field, B , ex-
 576 periences a force, $F = qv \times B$. This force can cause charged particles to have a
 577 curved trajectory in magnetic fields, which the ID and MS use to determine the
 578 particles p_T . The central solenoid provides the magnetic field for the ID and the
 579 toroidal magnets provide the magnetic field for the MS.

580 The layout of the magnet system is shown in Figure 2.16. The central solenoid
 581 consists of a single-layer Al-stabilized NbTi conductor coil wound inside an Al

582 support cylinder. The solenoid is 5.8 m long, 50 cm thick and has an inner radius
583 of 1.23 m. It is cooled to 4.5 K to reach superconducting temperatures and shares
584 the liquid argon calorimeter vacuum vessel to minimize material in the detector.
585 A current of 7.730kA produces a 1.998 T solenoidal magnetic field, pointing in
586 the $+z$ direction.

587 The toroidal magnet system consists of a barrel and two end-cap toroidal
588 magnets used to a magnetic field outside the calorimeters that is orientated along
589 ϕ . Each barrel toroid is 25.3 m long with an inner and outer diameter of 9.4 and
590 20.1 m and weighs 830 tonnes. Endcap toroids are 5 m long with an inner and
591 outer radius of 1.65 and 10.7 m. Both toroid systems use Al-stabilized Nb/Ti/Cu
592 conductors. The magnetic field strength of the barrel and endcap regions are 0.5
593 and 1 T.

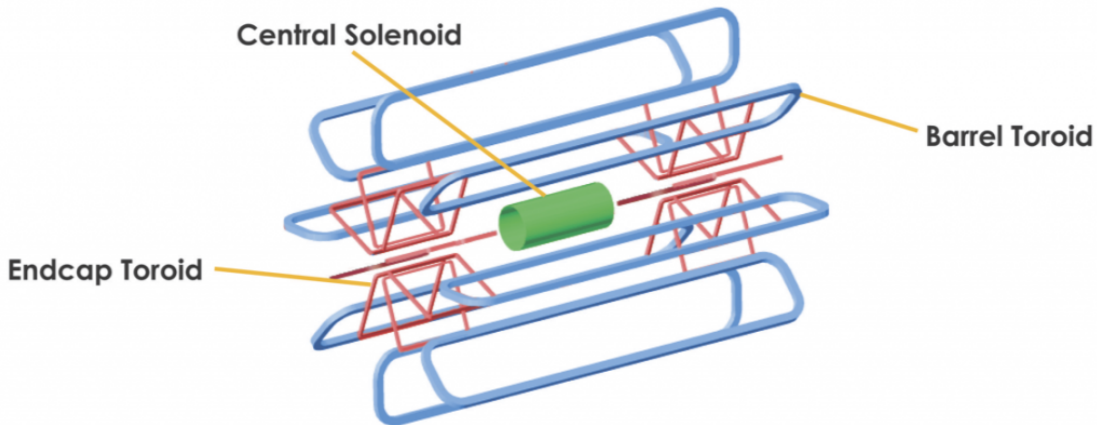


Figure 2.16: Layout of ATLAS magnet systems.

594 2.7 Trigger System

595 Since collisions occur every 25 ns and reading out all detector channels and
596 storing that information is not currently feasible (saving 60 million megabytes per

597 second), the majority of events are not kept for analysis. ATLAS uses a multi-
598 stage trigger system to select approximately 1,000 of the 1.7 billion collisions that
599 occur each second (corresponding to a rate of 1 kHz from the 40 MHz proton
600 collision rate). The first stage of the trigger system is the hardware level (L1)
601 trigger. This trigger reduces the event rate to 100 kHz by identifying Regions-
602 of-Interest (ROIs) containing high p_T leptons, photons, jets, or E_T^{miss} by using
603 information from RPCs, TGCs, and calorimeters to make a 2.5 μ s decision. This
604 information is then passed to a high-level trigger (HLT) which further decreases
605 event rates to 1 kHz. The HLT uses finer granularity measurements from the
606 MS and ID to perform simplified offline reconstruction to decide which events to
607 keep.

608 **Chapter 3**

609 **Analysis**

610 **3.1 Dataset and Simulated Samples**

611 **3.1.1 Dataset**

612 This analysis uses pp collision data collected from 2015 to 2018 at $\sqrt{s} = 13$
613 TeV, corresponding to 139/fb of data as shown in Figure 3.1 and 3.2. From this
614 dataset, only those events in which the tracker, calorimeters, and muon spectrom-
615 eter have good data quality are used. For a given event, the solenoid and toroidal
616 magnets must also be operating at their nominal field strengths. In addition to
617 this, events must pass further quality checks to reject events where detector sub-
618 systems may have failed. These selections reject events that containing LAr noise
619 bursts, saturation in the electromagnetic calorimeter, TileCal errors, and failures
620 in event recovery due to tracker failures. Events with information missing from
621 subsystems (usually due to busy detector conditions) are rejected. Events must
622 also contain a primary vertex with at least two associated tracks, where the pri-
623 mary vertex is selected as the vertex with the largest $\sum p_T^2$ over tracks associated
624 with the vertex and $p_T > 0.5$ GeV.

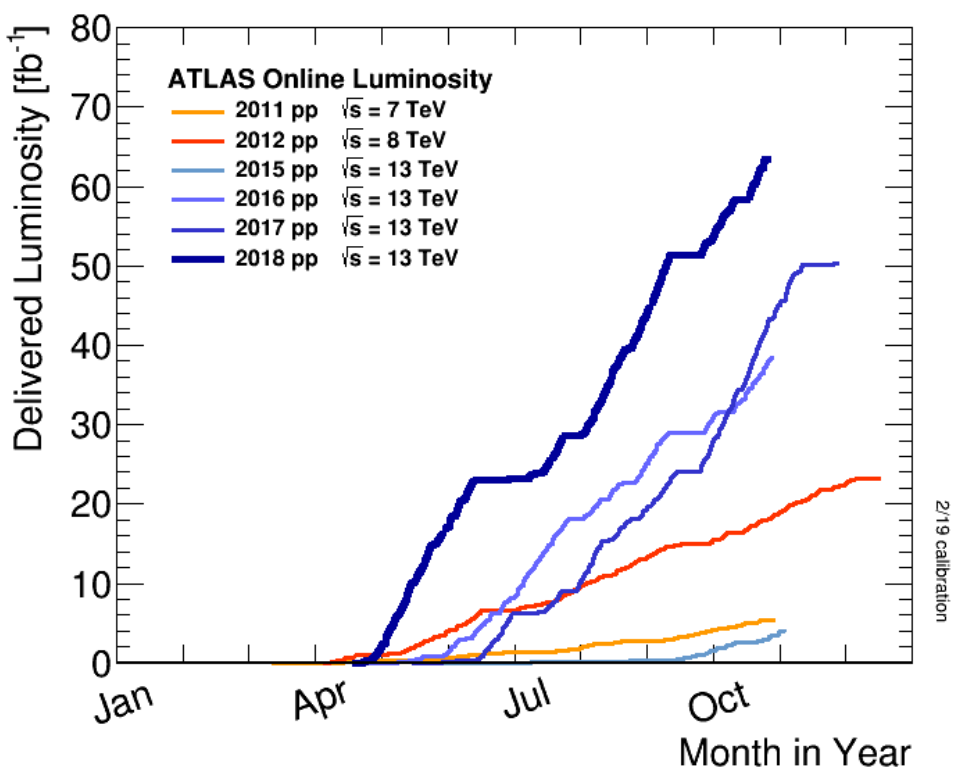


Figure 3.1: Integrated luminosity for data collected from ATLAS from 2011 - 2018

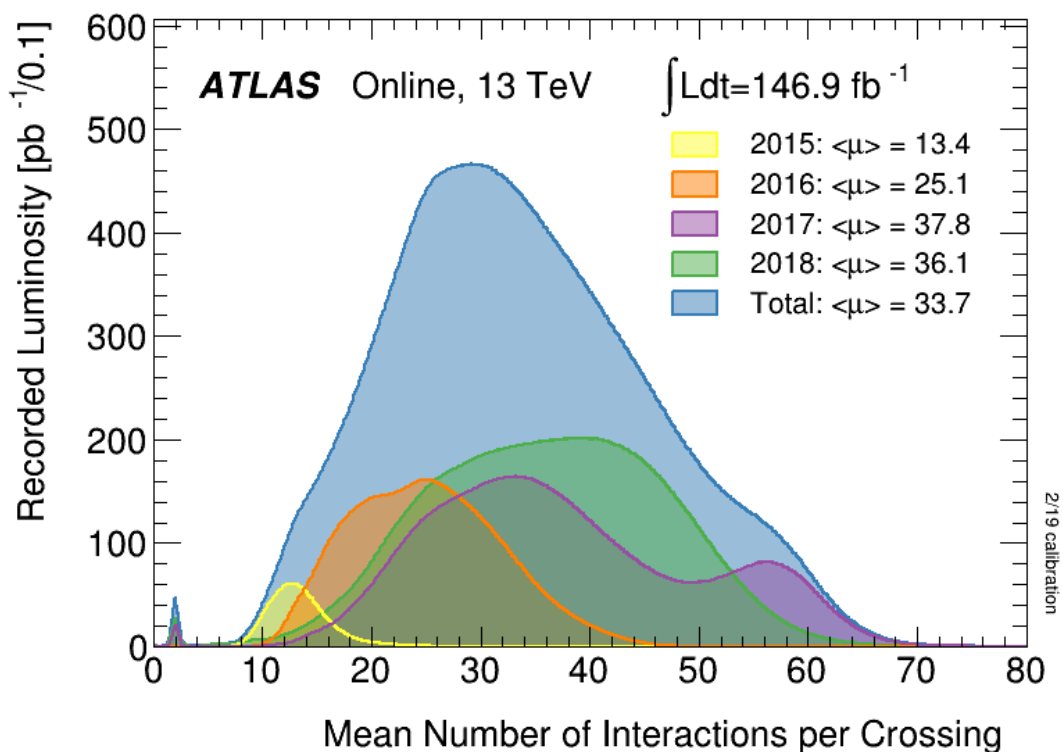


Figure 3.2: Mean number of interactions per crossing for data collected from ATLAS from 2011 - 2018

625 **3.1.2 Simulated Samples**

626 Samples are simulated in order to model backgrounds, evaluate signal ac-
627 ceptance, optimize event selection and estimate systematic and statistical uncer-
628 tainties. The dominant backgrounds for this analysis are $W/Z + \text{jets}$, diboson
629 (WZ/WW), $t\bar{t}$, single top and multijet production.

630 $W/Z + \text{jet}$ events are simulated using Sherpa 2.2.1 at NLO [cite [29]] and merged
631 with the Sherpa parton shower using the ME+PS prescription [11]. These events
632 are then normalized to NNLO cross sections. The $t\bar{t}$ and single-top backgrounds
633 are generated with Powheg-Box with NNPDF3.0NLO PDF sets in the matrix
634 element calculation [cite[35]]. Top quarks are decayed using MadSpin [cite[36]].
635 For all processes, the parton shower, fragmentation, and underlying event are
636 simulated using Pythia 8.320 with the A14 tune set[cite[ATL-PHYS-PUB-2014-
637 02]]. Diboson processes are generated using Sherpa 2.2.1.

638 Signal samples are simulated using MadGraph 5-2.2.2 [cite 42] and Pythia
639 8.186 with NNPDF230LO. RS Graviton samples are generated with $k/M_{PL}=1$.
640 HVT Model A and B samples are simulated with $g_H = -0.56$ and $g_f = -0.55$,
641 as the difference in the width of the samples is smaller than detector resolution.
642 Model C is generated by setting $g_H = 1$ and $g_f = 0$ to model VBF production of
643 HVT bosons. Signals are generated for masses between 300 GeV and 6 TeV.

644 **3.2 Object Selection**

645 **3.2.1 Electrons**

646 Electrons are reconstructed from electromagnetic showers in the LAr EM
647 calorimeter. During reconstruction cells of $\Delta\eta \times \Delta\phi = 0.025 \times 0.025$ are grouped
648 into 3×5 clusters. These clusters are then scanned for local maxima that seed elec-

tron clusters. These clusters must then be matched to ID track from the PV. This requirement minimizes non-prompt electron and fake electron backgrounds. Electrons must pass identification and isolation requirements. Electron identification (loose, medium, tight) classification is based on the discriminant of the multivariate analysis that identifies electrons using a likelihood based method. For this analysis tight electrons are used. Electrons are also required to be isolated. The electron isolation is calculated by comparing the sum of the transverse momentum in a cone around the electron of size $\Delta R = 0.2$ to the transverse momentum of the electron. This quotient must be less than 3.5, to further reject non-prompt photons and other fake backgrounds (multijet). Electrons in this analysis are also required to have $p_T > 30$ GeV and $|\eta| < 2.47$. Electrons are also required to have $p_T > 30$ GeV.

Electrons are calibrated to determine a data-driven scale factors from $J/\Psi \rightarrow ee$, $Z \rightarrow ee$, $Z \rightarrow \ell\ell\nu$ processes. These corrections account for the non-uniform response of the detector by introducing modeling and reconstruction uncertainties.

3.2.2 Muons

As muons traverse the entire detector, they are reconstructed from ID and MS tracks. For this analysis the muon identification and isolation working points are chosen to minimize the contributions from non-prompt muons. Towards this end, the medium muon identification working point is used. For this working point, two types of reconstructed muons are used: combined and extrapolated muons (CB and ME, respectively). For CB muons, ID and MS tracks are reconstructed independently and a combined track fit is performed by adding or removing MS tracks to improve the fit quality. ME muons are reconstructed from only MS tracks with hits in at least two layers, which ensures the track originates from the

674 PV. ME muons extend the acceptance for muon reconstruction outside the ID
675 from $2.5 < |\eta| < 2.7$. The medium identification working point uses CB and ME
676 tracks. CB tracks must have at least 3 hits in two MDT layers. ME tracks are
677 required to have at least three MDT/CSC hits. To further minimize contributions
678 from fake muons, the selected muons are required to be isolated from other tracks,
679 as muons from W, Z decays are often isolated from other particles. To insure the
680 selected muons are isolated, the scalar sum of the transverse momentum of tracks
681 in a cone of $\Delta R = 0.3$ compared to the transverse momentum of the muon must
682 be less then 0.06. Muons are also required to have $p_T > 30$ GeV.

683 Muons are calibrated using well-studied resonances $J/\Psi \rightarrow \mu\mu$ (low- p_T), $Z \rightarrow$
684 $\mu\mu$ (high- p_T). Figure 3.3 shows the combined muon p_T uncertainty from this
685 calibration. The total systematic uncertainty is less then 1% for all p_T ranges
686 considered in this analysis.

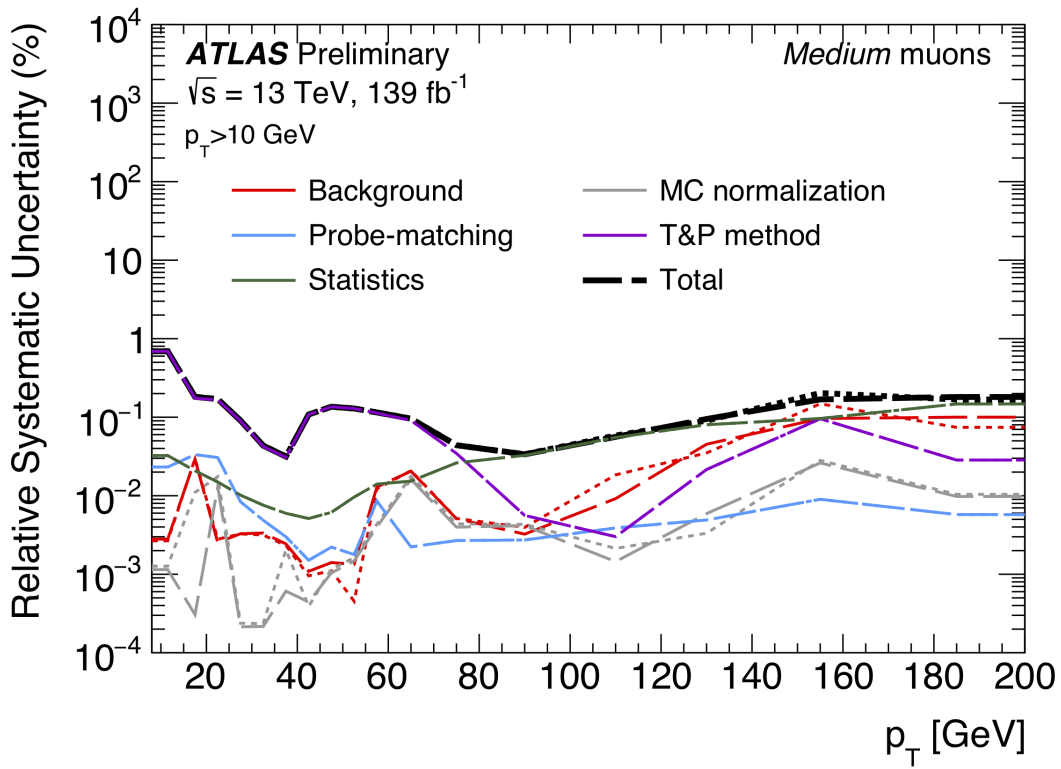


Figure 3.3: [4] This figure show the breakdown of the muon reconstruction efficiency scale factor measured in $Z \rightarrow \mu\mu$ as a function of p_T

687 3.2.3 small-R jets

688 Calorimeter jets are used to reconstruct the hadronically decaying W/Z candi-
 689 dates in the resolved analysis. These jets are less boosted and therefore spatially
 690 separated and reconstructed separately. These jets are constructed from topologi-
 691 cally connected clusters of calorimeter cells (topoclusters), seeded from calorimeter
 692 cells with energy deposits significantly above the noise threshold. These cells are
 693 then used as inputs to the $anti - k_T$ algorithm [12] with a distance = 0.4, here
 694 called small-R jets. These jets are calibrated to compensate and account for biases
 695 from jet reconstruction.

696 The jet energy is calibrated sequentially as shown in Figure 3.4. After the

697 jet direction is corrected to point to the PV, the energy of the jet is corrected.

698 First, the jet energy is corrected to account for pileup contributions based on the
699 p_T and area of the jet (these corrections are extracted from a $pp \rightarrow jj$ sample).

700 Following this, another pileup correction is applied that scales with μ and N_{PV} .

701 Then, MC-based corrections are applied that are meant to transform the jet
702 energy and η back to truth level. Therefore, these corrections account for the
703 non-compensating nature of the ATLAS calorimeters and inhomogeneity of the
704 detector. Following this the Global sequential calibration is applied that reduces
705 flavor dependence and jet that deposit energy outside the calorimeters. Finally,
706 in-situ corrections are applied that account for differences in jet responses between
707 data and simulation ($\gamma/Z+jet$ and multijet samples are used). These differences
708 can be due to mismodelling of the hard scatter event, pile-up, jet formation, etc.

709 Jet used in this analysis must have $p_T > 30$ GeV and $|\eta| < 2.5$. To further
710 reduce fake jets the jet-vertex-tagger (JVT) is used to reject pile-up jets [cite 43
711 P]. The JVT uses two track-based variables, corrJVF and R_{p_T} to calculate the
712 likelihood that the jet originated from the PV. The corrJVF compares the scalar
713 sum of the p_T of tracks associated with the jet and PV to the scalar sum of the
714 p_T of tracks associated with the jet. This variable also includes a correction that
715 reduces the dependency of corrJVF with the number of reconstructed vertices in
716 the event. R_{p_T} is given by the ratio of the scalar sum of the p_T of tracks associated
717 with the jet and PV to the p_T of the jet. Both of these variables peak around zero
718 for pileup jets, as these jets are unlikely to have tracks associated with the PV.
719 JVT cuts are applied to all jets with $p_T > 120$ GeV. Central jets ($|\eta| < 2.4$) are
720 required to have a $JVT > 0.59$ and forward jets ($2.4 < |\eta| < 2.5$) are required to
721 have $JVT > 0.11$.

722 To further reject fake jets, jets must pass quality requirements based on the

723 following variables ([cite P42]):

- 724 - f_Q^{LAr} : fraction of energy of jet's LAr cells with poor signal shape
 - 725 - f_Q^{HEC} : fraction of energy of jet's HEC cells with poor signal shape
 - 726 - E_{neg} : sum of cells with negative energy
 - 727 - f_{EM} : fraction of jet's energy deposited in EM calorimeter
 - 728 - f_{HEC} : fraction of jet's energy deposited in HEC calorimeter
 - 729 - f_{max} : maximum energy fraction in any single calorimeter layer
 - 730 - f_{ch} : ratio of the scalar sum of the p_T of a jet's charged tracks to the jet's p_T
- 731 Jets selected for the resolved analysis must pass one of the following criteria:
- 732 - $f_{HEC} > 0.5$ and $|f_Q^{HEC}| > 0.5$ and $\langle Q \rangle > 0.8$
 - 733 - $|E_{neg}| > 60$ GeV
 - 734 - $f_{EM} > 0.95$ and $f_Q^{LAr} > 0.8$ and $\langle Q \rangle > 0.8$ and $|\eta| < 2.8$
 - 735 - $f_{max} > 0.99$ and $|\eta| < 2$
 - 736 - $f_{EM} < 0.05$ and $f_{ch} < 0.05$ and $|\eta| < 2$
 - 737 - $f_{EM} < 0.05$ and $|\eta| > 2$

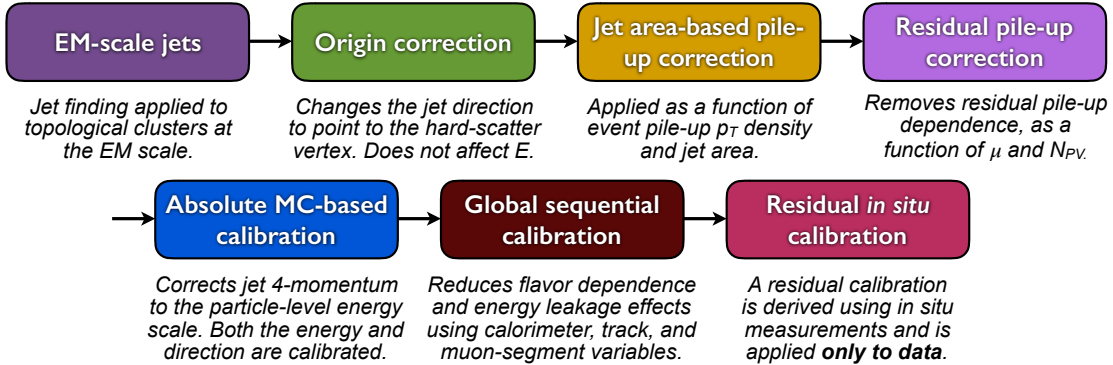


Figure 3.4: [6] This diagram shows the calibration stages for EM jets.

738 3.2.4 large-R jets

739 Large-R ($\Delta R = 1.0$) jets are used to reconstruct the high- $p_T W/Z \rightarrow qq$ candi-
 740 dates in the merged analysis. Track-Calorimeter Clusters (TCCs) are used to reconstruct
 741 these jets [cite ANA 50]. These jets are constructed via a pseudo particle flow
 742 method using ID tracks matched to calorimeter clusters. The angular resolution
 743 of the calorimeter degrades sharply with jet p_T , but the jet energy resolution im-
 744 proves. The tracker has excellent angular resolution improves with p_T . Therefore,
 745 by matching tracks to jets, TCCs have more precise energy and angular resolution
 746 the jets constructed from calorimeter information only. These jets are required to
 747 have $p_T > 200$ GeV, $|\eta| < 2.0$ and $m_J > 50$ GeV.

748 TCC jets are trimmed as detailed in [cite ANA 45], which suppresses pileup
 749 and soft radiation in the jet, the jet mass is calculated as the four-vector sum
 750 of the jet's constituents (assuming massless constituents). The jet mass peaks
 751 around the W/Z boson mass for $W/Z \rightarrow qq$ jets, and more broadly for quark and
 752 gluon induced jets.

753 These jets are then tagged as W/Z jets if they pass the jet mass and D_2
 754 cuts. The jet substructure variable D_2 is given by the ratio of energy correlation
 755 functions based on energies and pair-wise angles of a jet's constituents [cite ANA

756 46, 47]:

$$D_2^{\beta=1} = E_{CF3} \left(\frac{E_{CF1}}{E_{CF2}} \right)^3 \quad (3.1)$$

757 Where the energy correlation functions are defined as:

$$E_{CF1} = \sum_i p_{T,i} \quad (3.2)$$

758

$$E_{CF2} = \sum_{ij} p_{T,i} p_{T,j} \Delta R_{ij} \quad (3.3)$$

759

$$E_{CF3} = \sum_{ijk} p_{T,i} p_{T,j} p_{T,k} \Delta R_{ij} \Delta R_{jk} \Delta R_{ki} \quad (3.4)$$

760 A two-dimensional optimization of the jet mass and D_2 thresholds was per-
761 formed to provide maximum sensitivity for this analysis. Figure ?? shows the
762 optimized thresholds on D_2 and jet mass as a function of p_T . Figure 3.6 shows
763 the efficiency of the optimized W/Z taggers as a function of jet p_T .

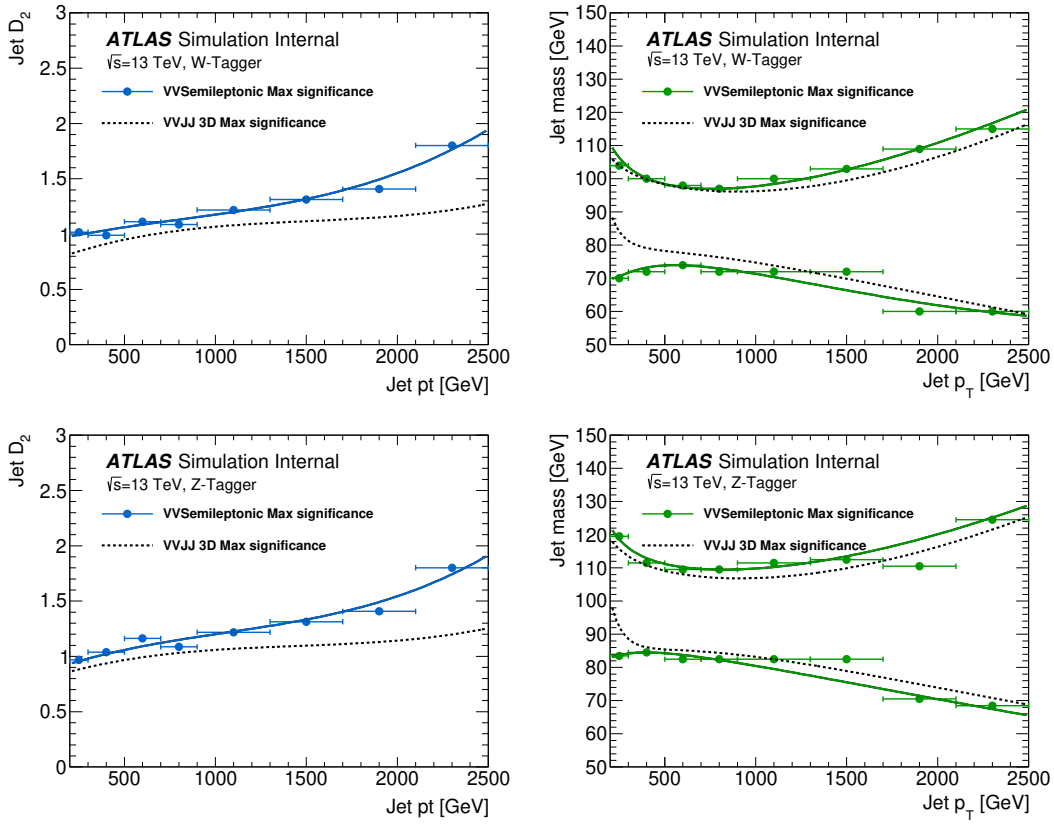


Figure 3.5: The upper cut on D_2 (a) and jet mass window cut i.e. the upper and lower boundary of the mass (b) of the W -tagger as a function of jet p_T . Corresponding values for Z -tagger are shown in (c) and (d). The optimal cut values for maximum significance are shown as solid markers and the fitted function as solid lines. Working points from $VV \rightarrow JJ$ [ATLAS-HDBS-2018-31-002] is also shown as dashed lines as a reference. Natasha reword?

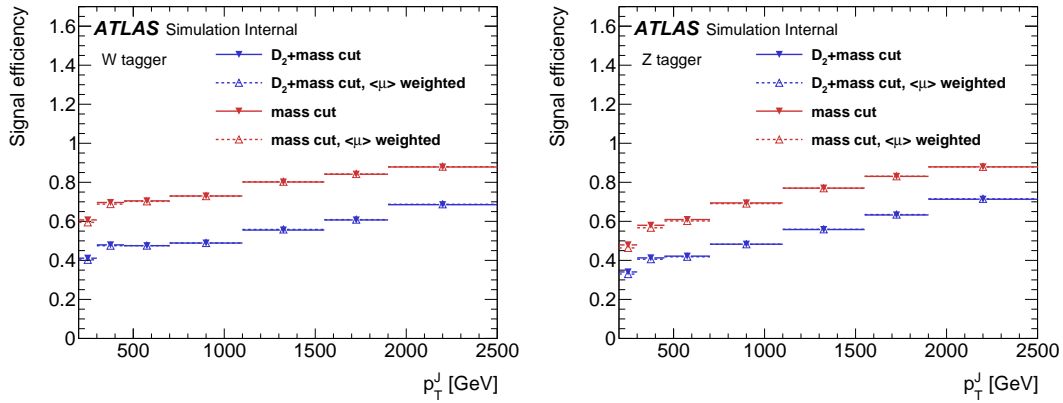


Figure 3.6: Natasha write caption

764 **3.2.5 Variable Radius jets**

765 Variable-radius (VR) track jets are used to identify b-quark induced jets in
766 large-R jets [cite ANA 52]. These jets use a p_T dependent cone size defined as:

$$R_{eff}(p_{T,i} = \frac{\rho}{p_{T,i}}) \quad (3.5)$$

767 for building jets from ID tracks with an anti-kt algorithm. For this analysis
768 $\rho = 30$ GeV and an upper and lower limit on cone size are set to 0.02 and 0.4,
769 respectively. Collinear VR jets are possible, so track jets that are not separated
770 by the the smaller jet's cone size are not used. These jets are also required to
771 have $p_T > 10$ GeV and $|\eta| < 2.5$.

772 **3.2.6 MET/neutrinos**

773 As neutrinos are uncharged and color less they do not leave tracks or jets in
774 the detector. For this reason, neutrinos are reconstructed calculated the E_T^{miss} .
775 This quantity is defined as negative vector sum of p_T all the physics objects and
776 an extra "soft" term. The "soft" term accounts for energy depsoits not associated
777 with any of the objects in the event. For this analysis the soft term is given by
778 the summing the p_T of all ID tracks not associated with objects in the event. The
779 selected tracks must be matched to the primary vertex, which decreases pile-up
780 contamination [cite G 217 218]. The tight working point is used [Natasha look up
781 what this means].

782 **3.2.7 Jet Flavor Tagging**

783 To further classify events, the small radius jets are identified as originated
784 for a b-quark or not using the multivariate b -tagging algorithm (BDT), MC2c10

[cite G 210 199]. This algorithm uses the impact parameters of the jet's ID tracks, secondary vertices (if they exist), and reconstructed flight paths of b and c hadrons in the jet to determine if the jet was induced by a b -quark. For this analysis the 85% efficient working point of this algorithm is used to a fixed cut on the BDT discriminant that yields an 85% tag rate, and c , τ , and light-flavor jet rejection of 3, 8, and 34 respectively in a simulated $t\bar{t}$.

3.2.8 Overlap Removal

The reconstructed jets and leptons in this analysis can arise from the same energy deposits. For instance, a jet may radiate an electron that is then reconstructed separately as the signal lepton in the event. To mitigate this confusion of multiple objects originating from a single jet or lepton overlapping objects are removed via a procedure referred to as overlap removal. In this procedure the separation of the two objects, $\Delta(R) = \sqrt{(\Delta\eta)^2 + (\Delta\phi)^2}$ determines which object is removed from the event.

The overlap selections used in this analysis are:

- when an electron shares a track the electron with the lower p_T is rejected, as it is more likely to be a fake electron
- when a muon and electron share a track the muon is rejected if it is a calo-muon, otherwise the electron is rejected
- when $\Delta R < 0.2$ for an electron and jet, the jet is rejected to maximize signal acceptance
- when $\Delta R > 0.2$ for an electron and jet, the electron is rejected as likely originated from decays within the jet

- 808 - when $\Delta R < \min(0.4, 0.04 + 10\text{GeV}/p_T^\mu)$ the muon is rejected, again maxi-
 809 mizing signal acceptance, otherwise the jet is rejected
- 810 - when $\Delta R < 1.0$ for the a large-R jet and electron, the jet is rejected

811 3.3 Event Selection and Categorization

812 3.3.1 Pre-selection

813 Before applying topological cuts to suppress backgrounds and reduce data
 814 size in this search, preselection cuts are applied which include trigger and event
 815 requirements. Events must contain exactly one tight lepton (no additional loose
 816 leptons), the $p_T^{\ell\nu} > 75$ GeV, and there must be at least two small-R jets or one
 817 large-R jet.

818 3.3.2 Trigger

819 The data was collected using the lowest unprescaled single-lepton or E_T^{miss}
 820 triggers, as summarized in Table [natasha add table]. Since the muon term is not
 821 considered in the trigger E_T^{miss} calculation, the E_T^{miss} trigger is fully efficient to
 822 events with high- p_T muons. For this reason, the E_T^{miss} trigger is used for events
 823 where $p_T^\mu > 150$ GeV, to compensate for the poor efficiency of the single muon
 824 trigger below 150 GeV (due to detector coverage).

Table 3.1: The list of triggers used in the analysis.

Data-taking period	$e\nu qq$ channel	$\mu\nu qq$ ($p_T(\mu\nu) < 150$ GeV) channel	$\mu\nu qq$ ($p_T(\mu\nu) > 150$ GeV) channel
2015	HLT_e24_lhmedium_L1EM20 OR HLT_e60_lhmedium OR HLT_e120_lhloose	HLT_mu20_iloose_L1MU15 OR HLT_mu50	HLT_xe70
2016a (run < 302919) $(L < 1.0 \times 10^{34} \text{ cm}^{-2} \text{ s}^{-1})$	HLT_e26_lhtight_nod0_ivarloose OR HLT_e60_lhmedium_nod0 OR HLT_e140_lhloose_nod0 HLT_e300_etcut	HLT_mu26_ivarmedium OR HLT_mu50	HLT_xe90_mht_L1XE50
2016b (run ≥ 302919) $(L < 1.7 \times 10^{34} \text{ cm}^{-2} \text{ s}^{-1})$	same as above	same as above	HLT_xe110_mht_L1XE50
2017	same as above	same as above	HLT_xe110_pufit_L1XE55
2018	same as above	same as above	HLT_xe110_pufit_xe70_L1XE50

825 **3.3.3 GGF/VBF RNN**

826 To classify events as originating from GGF/DY or VBF production a recursive
827 neural network (RNN) is used. This approach is more powerful than a cut-based
828 classification as it improves signal efficiency and analysis sensitivity by exploit-
829 ing correlations between variables that the RNN learns. In particular, a RNN
830 architecture is ideal as it can handle variable numbers of jets in the events.

831 The RNN uses the four-momentum of candidate VBF jets to classify events
832 as VBF or GGF topologies. As sometimes jets will be incorrectly reconstructed
833 the number of jets in the event are expected to vary across the inputs samples.
834 VBF candidate jets are identified by removing jets from the event that are likely
835 from $W/Z \rightarrow qq$. For the resolved regime this means removing the two leading
836 small-R jets from the VBF candidate jet list. For the merged regime this means
837 removing small-R jets that are $\Delta R < 1.0$. Also the VBF candidate jets are also
838 required to be within $|\eta| < 4.5$. From the list of remaining VBF candidate jets,
839 the two highest- p_T jets are chosen.

840 The architecture of the RNN is show in Figure 3.7. LSTMs are a type of
841 RNN that extract meaningful information and can retain it (unlike other neural
842 networks architectures). This is useful for VBF event classification for events with
843 two jets, where using the kinematic properties of both jets (and their correlations)
844 will lead to more efficient event classification.

845 In this RNN architecture, the VBF candidates are first passed to a masking
846 layer which checks the number of jets in the event. If there is only one jet, only
847 one LSTM layer is used. The output of masking is then passed to a LTSM cell
848 (with a tanh activation) [natasha cite LSTM], and then to a dropout layer, that
849 has a probability of 0.3 to completely forget the output of the LSTM. Dropout
850 is a regularization method, that prevents overfitting. The output of the dropout

851 layer is then passed to the second LSTM and then through another dropout layer
852 with a probability of 0.3.

853 The weights and other parameters of the network are learned by training the
854 network with VBF and GGF signals over 200 epochs with an Adam Optimizer
855 [natasha add reference]. The training is truncated if the network parameters are
856 unchanged after ten iterations. The training, testing and validation sets are 56,
857 30, and 14 percent of the input samples, respectively. Figure [add INT figure
858 32] shows the loss function of the network as a function of training epochs. The
859 validation test set has a smaller loss function as dropout was not applied. Figure
860 3.9 shows the ROC curve for the RNN using k-fold cross validation.

861 Finally this output is passed to a dense layer [natasha ask antonio about this]
862 and then to a sigmoid activation layer, leading to an overall RNN score. Figure 3.8
863 shows the RNN discriminant for shows modeling of the discriminant. The RNN
864 score is 0 for GGF and background processes and 1 for VBF processes. Figure
865 ?? shows the limits for various signal processes based on the RNN cut applied.
866 The most efficient cut was found to be RNN Score > 0.8, for VBF classification.

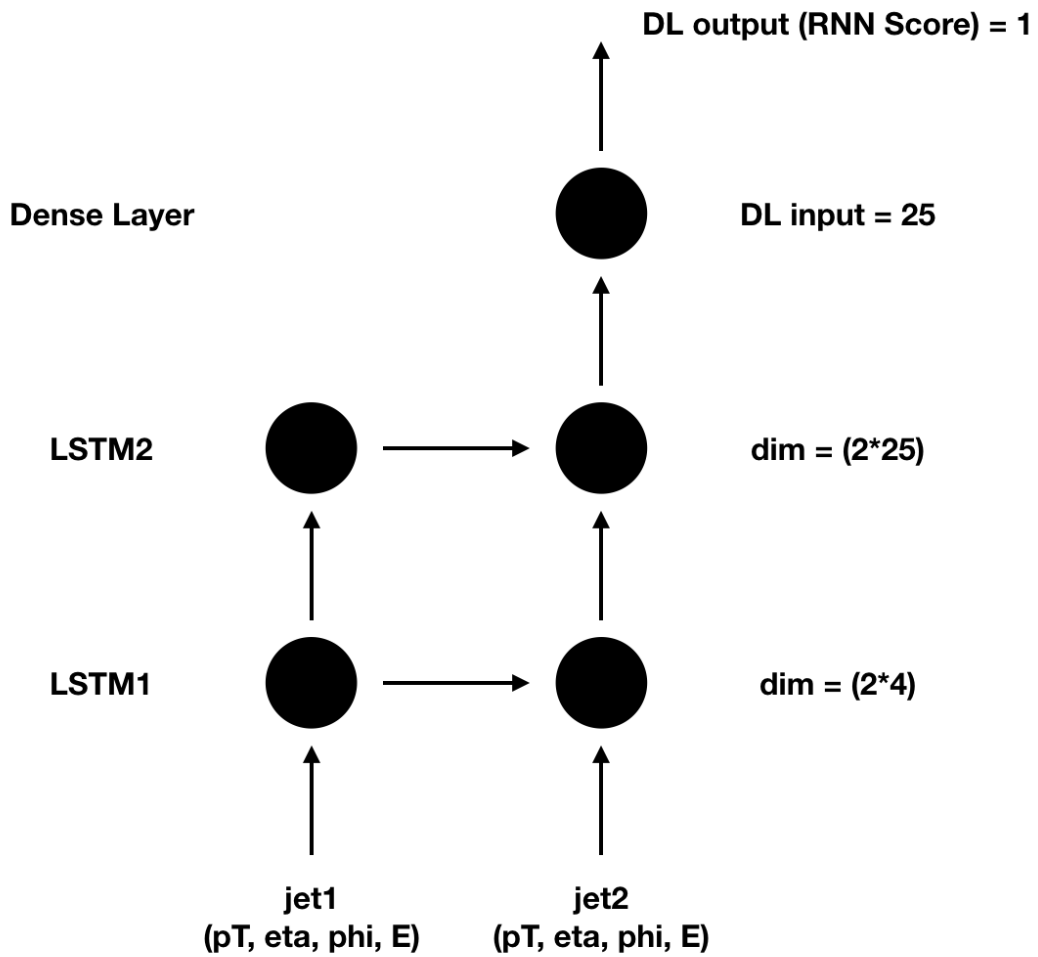


Figure 3.7: RNN architecture. Natasha add caption

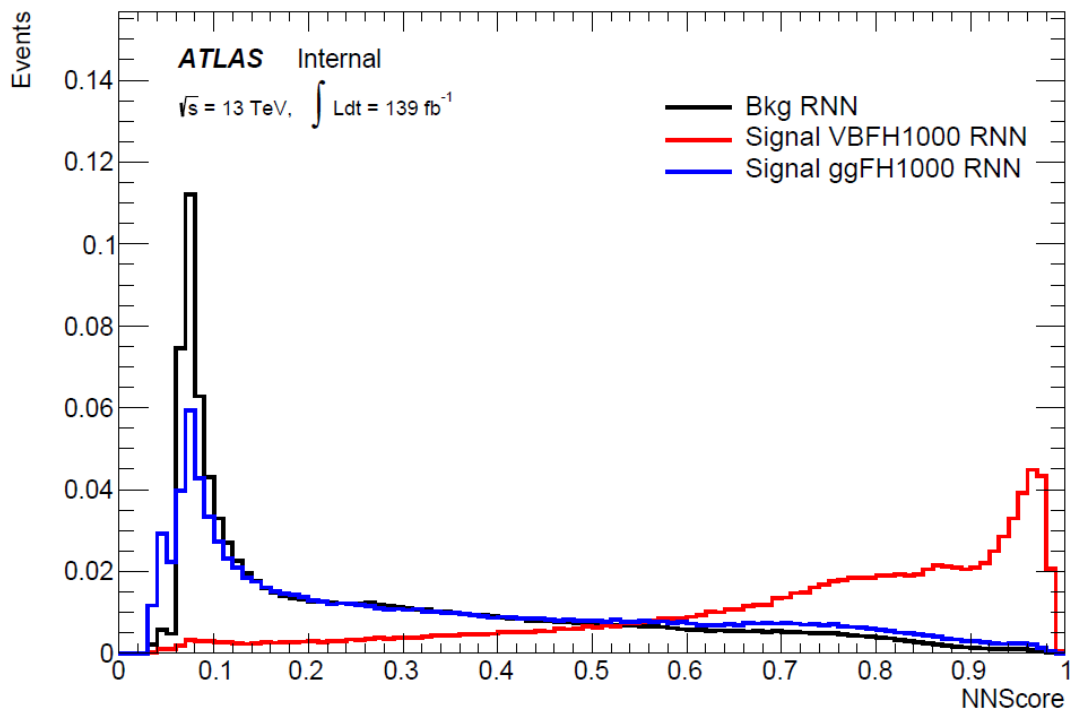


Figure 3.8: RNN Score distribution for ggF and VBF signals and backgrounds.

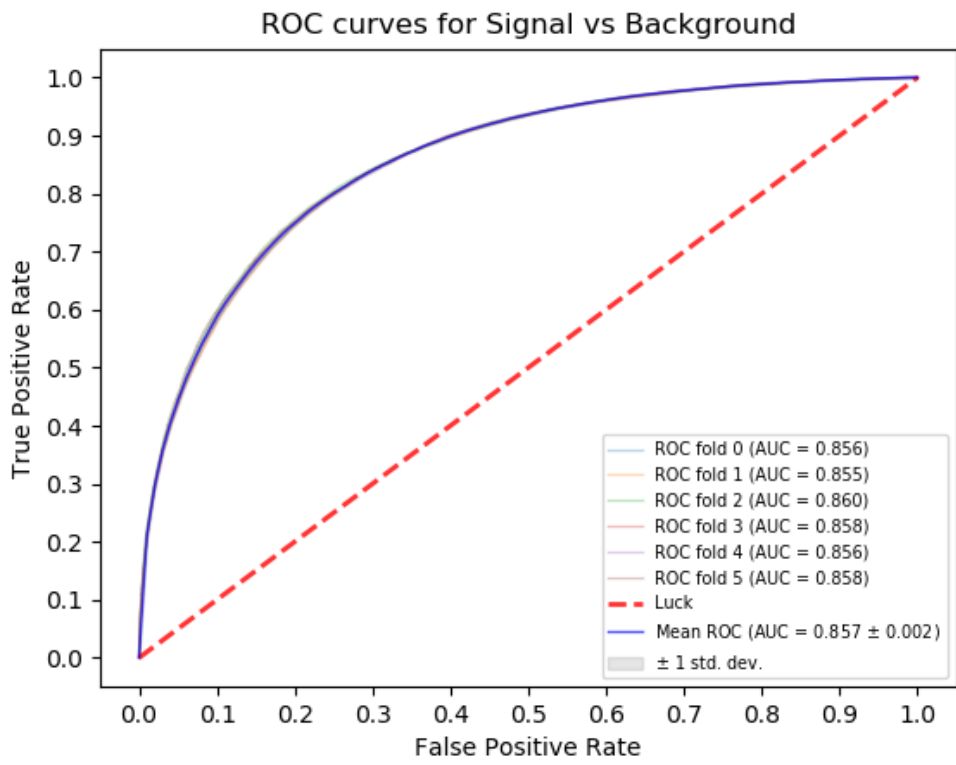


Figure 3.9: ROC curve using k-fold validation for RNN.

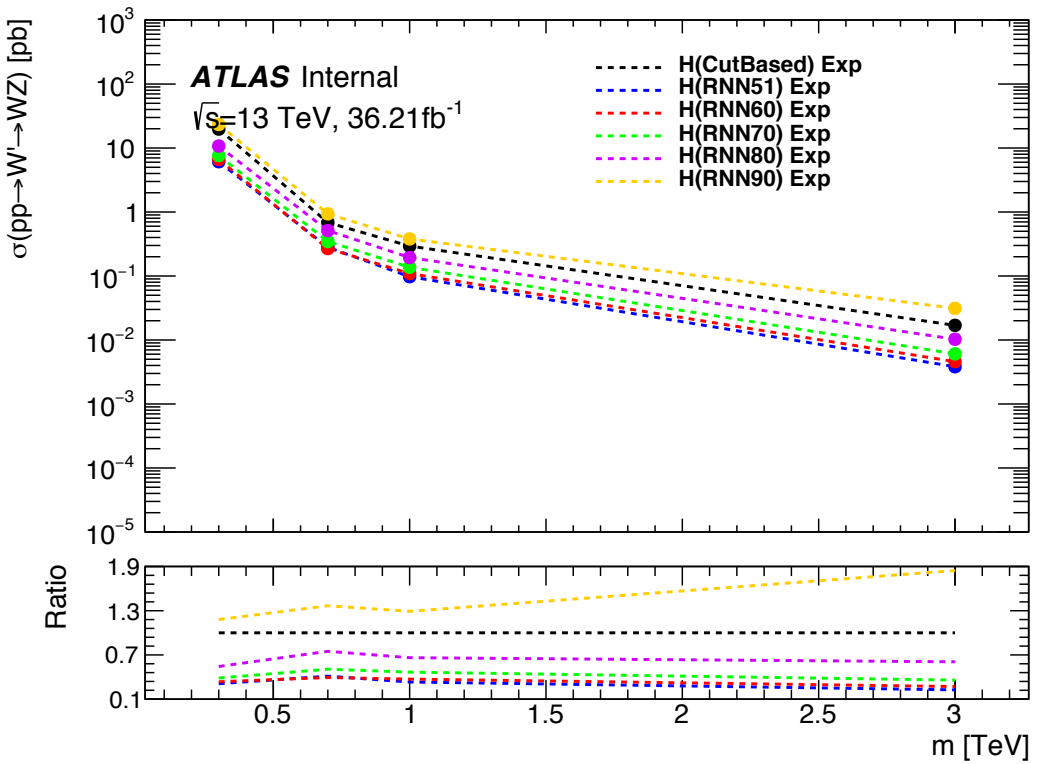


Figure 3.10: Comparison of GGF Z' limits for different RNN score selections.

867 3.3.4 Topological Cuts

868 Once an event is classified as VBF or GGF via the RNN it must pass other
 869 topological cuts that maximize signal efficiency and background rejection. First,
 870 to efficiently select events with $W \rightarrow \ell\nu$ candidate exactly one tight lepton is
 871 required and $E_T^{miss} > 100(60)$ GeV and $p_{T,\ell\nu} > 200(75)$ GeV in the merged (re-
 872 solved) analysis to suppress the multi-jet background. To more accurately model
 873 the two dominant backgrounds in this analysis, $W + \text{jets}$ and $t\bar{t}$, control regions are
 874 used constructed for each. These control regions are dominated by these processes
 875 and used to extract normalization factors that are then used in the signal region
 876 estimates.

877 For the merged analysis, in addition to the $W \rightarrow \ell\nu$ and $W/Z \rightarrow J$ selections

above, the relative boson p_T is cut to enhance signals, i.e. $\min(p_{T,\ell\nu}, p_{T,J})/m_{WV} > 0.35(0.25)$ for the GGF (VBF) category. To minimize $t\bar{t}$ contamination the signal region and $W+\text{jets}$ control region events with at least one b jet with $\Delta R > 1.0$ from the large-R jet are excluded. For the $t\bar{t}$ control region the event must contain at least one such b jet. High purity signal regions require the D_2 and W/Z mass window cut to be passed, whereas the low purity region only requires the W/Z mass window cut to be passed. Finally for events to be classified as tagged the large-R jet must contain exactly two b-tagged jets. Untagged events must have no more than one b-tagged jet matched to the large-R jet. These selections are shown in Table 3.2. The distributions for the variables used in merged analysis for top control regions are shown in Figure 3.12- 3.15.

Events failing the merged selection are then re-analyzed in the resolved category. To enhance resolved signals, the event should contain two high- p_T boson that are back-to-back in the x-y plane as shown by the cuts in Table 18. Again to suppress the $t\bar{t}$ background in the WCR and SR events are required to have no additional b-jets.

The WV system mass, m_{WV} is reconstructed from the lepton, neutrino, and hadronically-decaying boson candidate. The momentum of the neutrino along the z -direction is obtained by constraining the $W((Z))$ boson mass of the lepton neutrino system to be 80.3 (91.8) GeV/c^2 . For complex solutions to this constraint, p_Z is taken as either the real component of the complex solutions or the one with the smaller absolute value of the two real solutions. For the resolved analysis, m_{WV} is reconstructed by constraining the $W(Z)$ dijet system:

$$p_{T,jj}^{corr} = p_{T,jj} \times \frac{m_{W/Z}}{m_{jj}} \quad (3.6)$$

$$m_{jj}^{corr} = m_{W/Z} \quad (3.7)$$

Table 3.2: Summary of selection criteria used to define the signal region (SR), W +jets control region (W CR) and $t\bar{t}$ control region ($t\bar{t}$ CR) for merged 1-lepton channel.

Selection		SR		W CR (WR)		$t\bar{t}$ CR (TR1)	
		HP	LP	HP	LP	HP	LP
$W \rightarrow \ell\nu$	Num of Tight leptons	1					
	Num of Loose leptons	0					
	E_T^{miss}	$> 100 \text{ GeV}$					
	$p_T(\ell\nu)$	$> 200 \text{ GeV}$					
$W/Z \rightarrow J$	Num of large- R jets	≥ 1					
	D_2 cut	pass	fail	pass	fail	pass	fail
	W/Z mass window cut	pass	pass	fail	fail	pass	pass
	Numb. of associated VR track jets b -tagged	For $Z \rightarrow J$: ≤ 1 ($= 2$) for untagged (tagged) category					
	$\min(p_{T,\ell\nu}, p_{T,J}) / m_{WV}$	$> 0.35(0.25)$ for DY/ggF (VBF) category					
	Top-quark veto	Num of b -tagged jets outside of large- R jet	0		≥ 1		
Pass VBF selection			no (yes) for DY/ggF (VBF) category				

902 where m_{jj} and $m_{W/Z}$ are the reconstructed invariant mass of the hadronically-
903 decaying W/Z boson and the PDG values of the W/Z boson masses, respectively.
904 A summary of the resolved selections is shown in Table 3.3. The distributions for
905 the variables used in the resolved analysis in the TCR are shown in Figure 3.16,
906 3.17.

907 Events classified as VBF events are classified as Merged High purity, low
908 purity or resolved signal region selections sequentially. If the event does not pass
909 any of these selections but passes a VBF control region selection it is classified as
910 a VBF CR event. If the event fails the VBF selection it is then checked if it passes
911 the Merged High purity, Low purity or resolved signal region selections (NB: for
912 the WZ decay modes all the region have tagged and untagged categories). If the
913 event fails all the GGF signal region selections, it is then kept for GGF control
914 region selections, if it passes those selections. This cutflow is shows in Figure
915 3.11.

Table 3.3: The list of selection cuts in the resolved analysis for the WW and WZ signal regions (SR), $W+\text{jets}$ control region (WR) and $t\bar{t}$ control region (TR).

cuts	SR	W CR (WR)	$t\bar{t}$ CR (TR1)
$W \rightarrow \ell\nu$	Number of Tight leptons	1	
	Number of Loose leptons	0	
	E_T^{miss}	$> 60 \text{ GeV}$	
	$\cancel{p}_T(\ell\nu)$	$> 75 \text{ GeV}$	
$W/Z \rightarrow jj$	Number of small-R jets	≥ 2	
	Leading jet p_T	$> 60 \text{ GeV}$	
	Subleading jet p_T	$> 45 \text{ GeV}$	
	$Z \rightarrow q\bar{q}$ $W \rightarrow q\bar{q}$	$78 < m_{jj} < 105 \text{ GeV}$ $68 < m_{jj} < 98 \text{ GeV}$	$50 < m_{jj} < 68 \text{ GeV}$ or $105 < m_{jj} < 150 \text{ GeV}$
Topology cuts	Num. of b -tagged jets	For $Z \rightarrow jj$: ≤ 1 ($= 2$) for untagged (tagged) category	
	$\Delta\phi(j, \ell)$	> 1.0	
	$\Delta\phi(j, E_T^{\text{miss}})$	> 1.0	
	$\Delta\phi(j, j)$	< 1.5	
	$\Delta\phi(\ell, E_T^{\text{miss}})$	< 1.5	
Top vetos	$\min(p_{T,\ell\nu}, p_{T,jj}) / m_{WW}$	$> 0.35(0.25)$ for DY/ggF (VBF) category	
	Number of additional b -tagged jets	0	≥ 1
Pass VBF selection		no (yes) for DY/ggF (VBF) category	

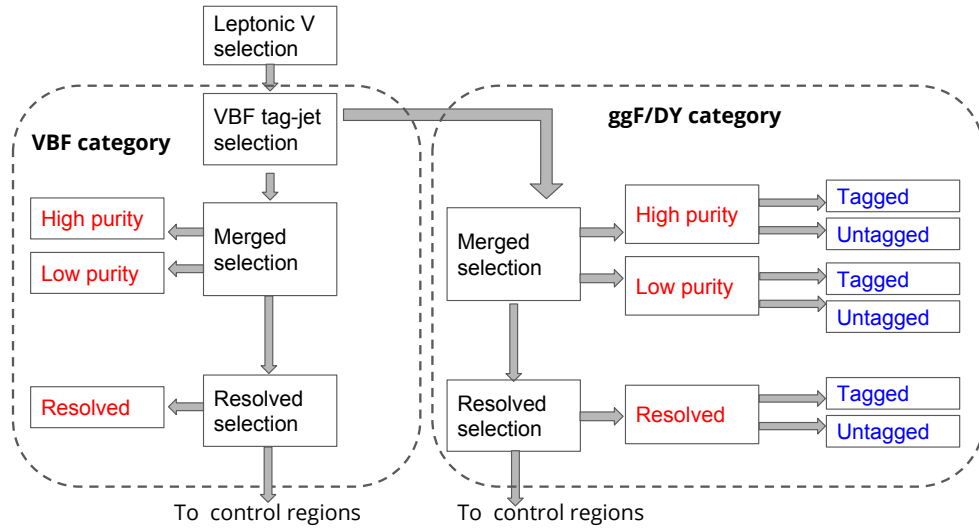


Figure 3.11: Event Categorization. Natasha write more.

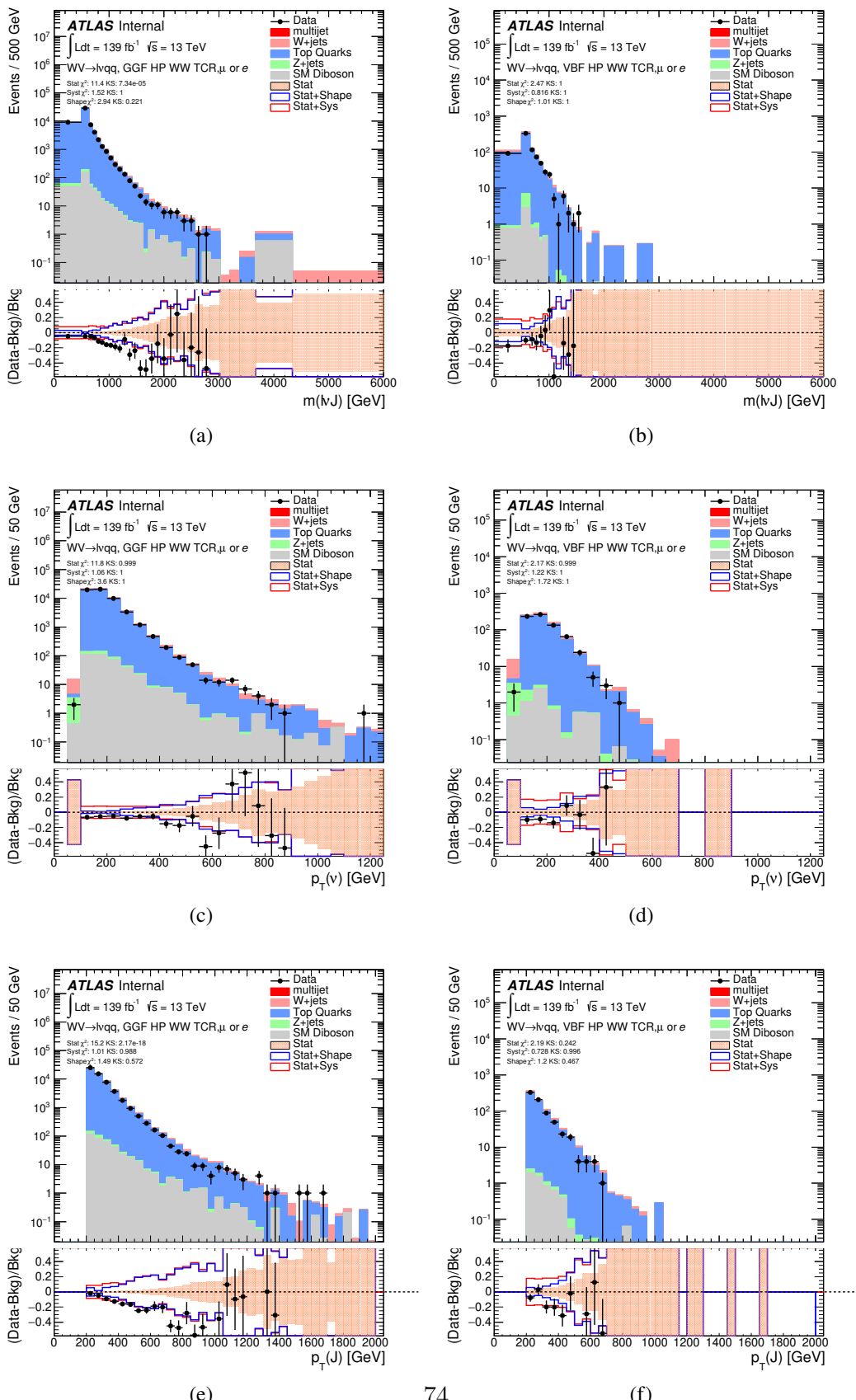


Figure 3.12: Data MC comparison for the merged WW HP TCR.

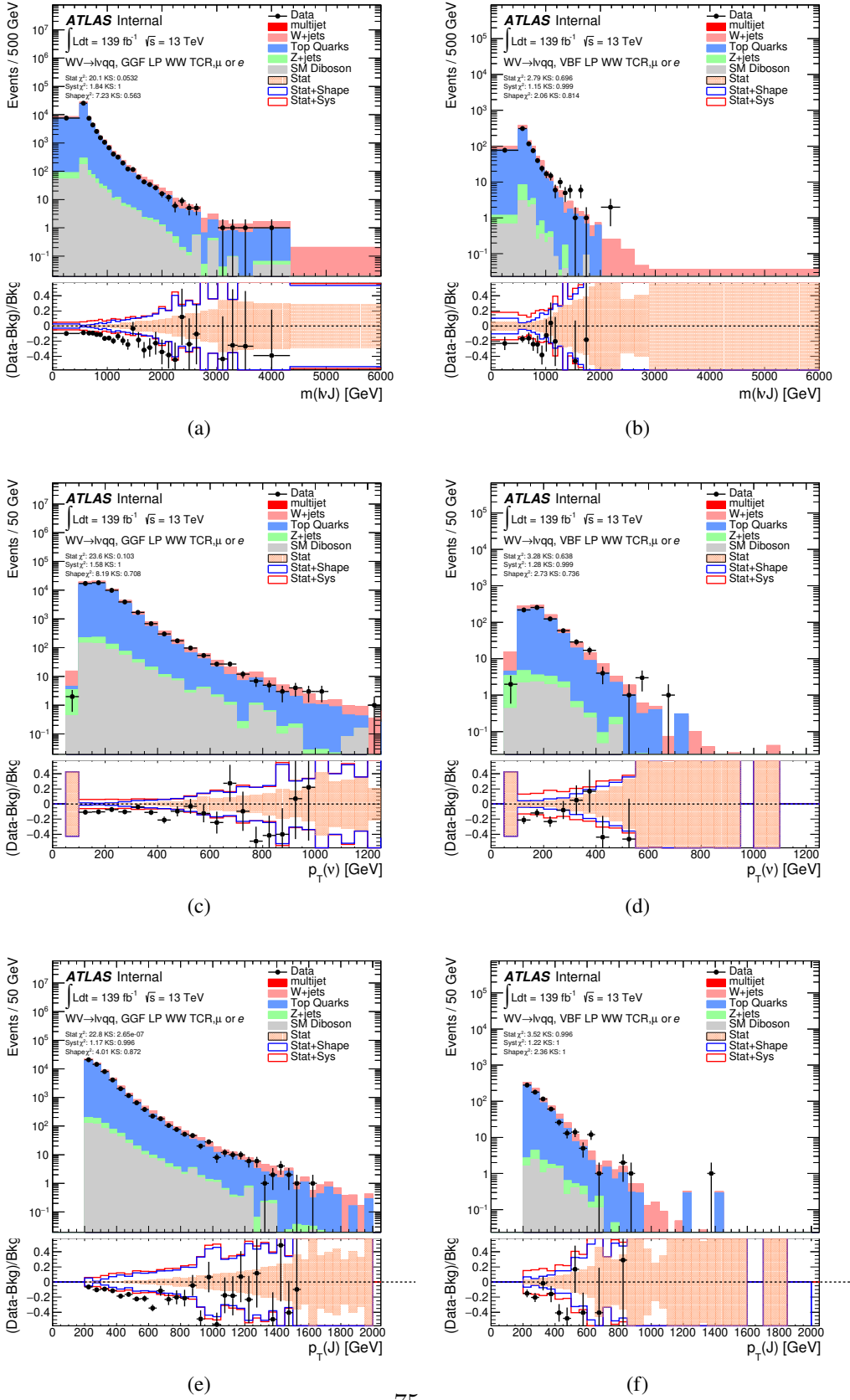


Figure 3.13: Data MC comparison for the merged WW LP TCR.

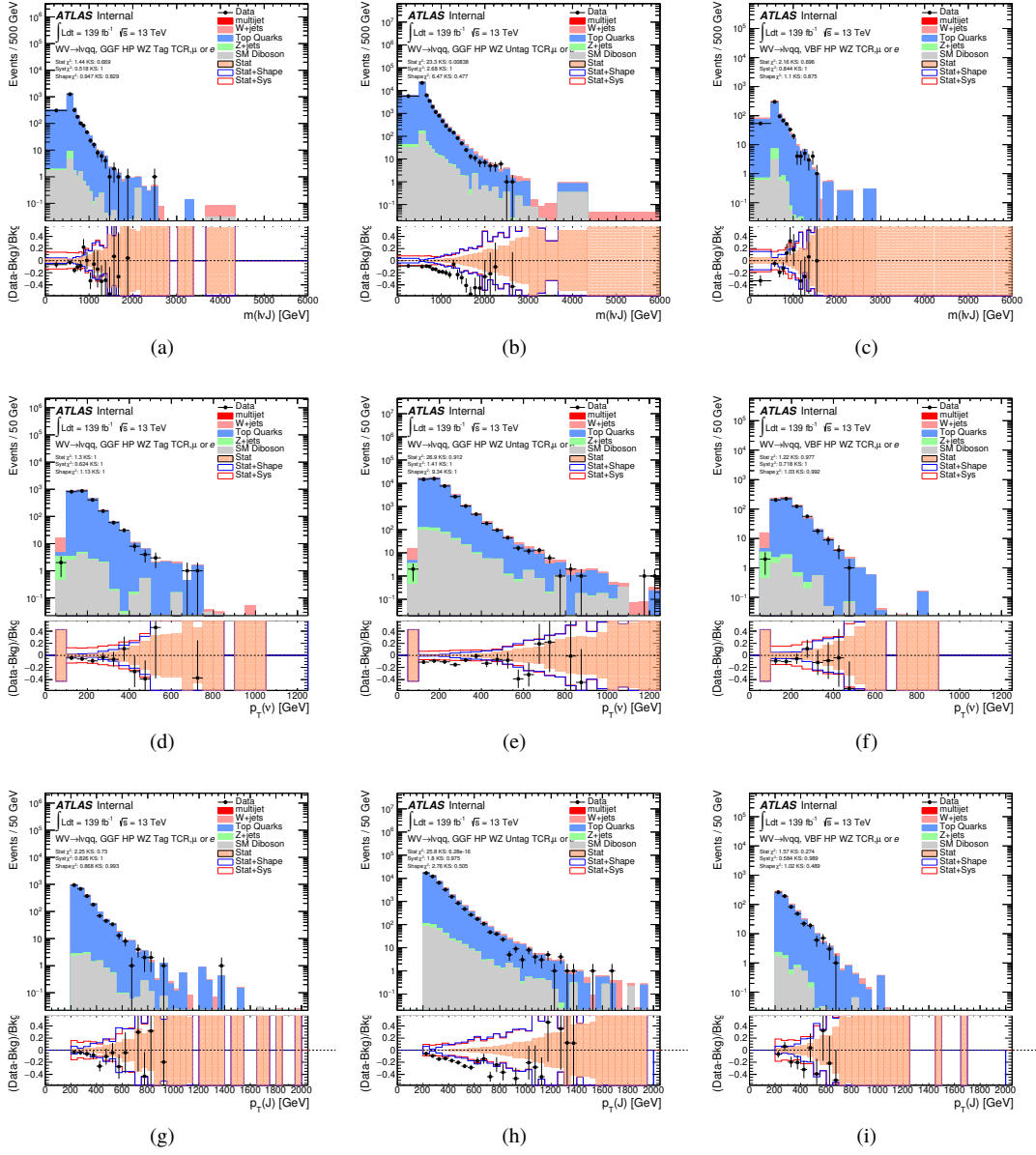


Figure 3.14: Data MC comparison for the merged WZ HP TCR.

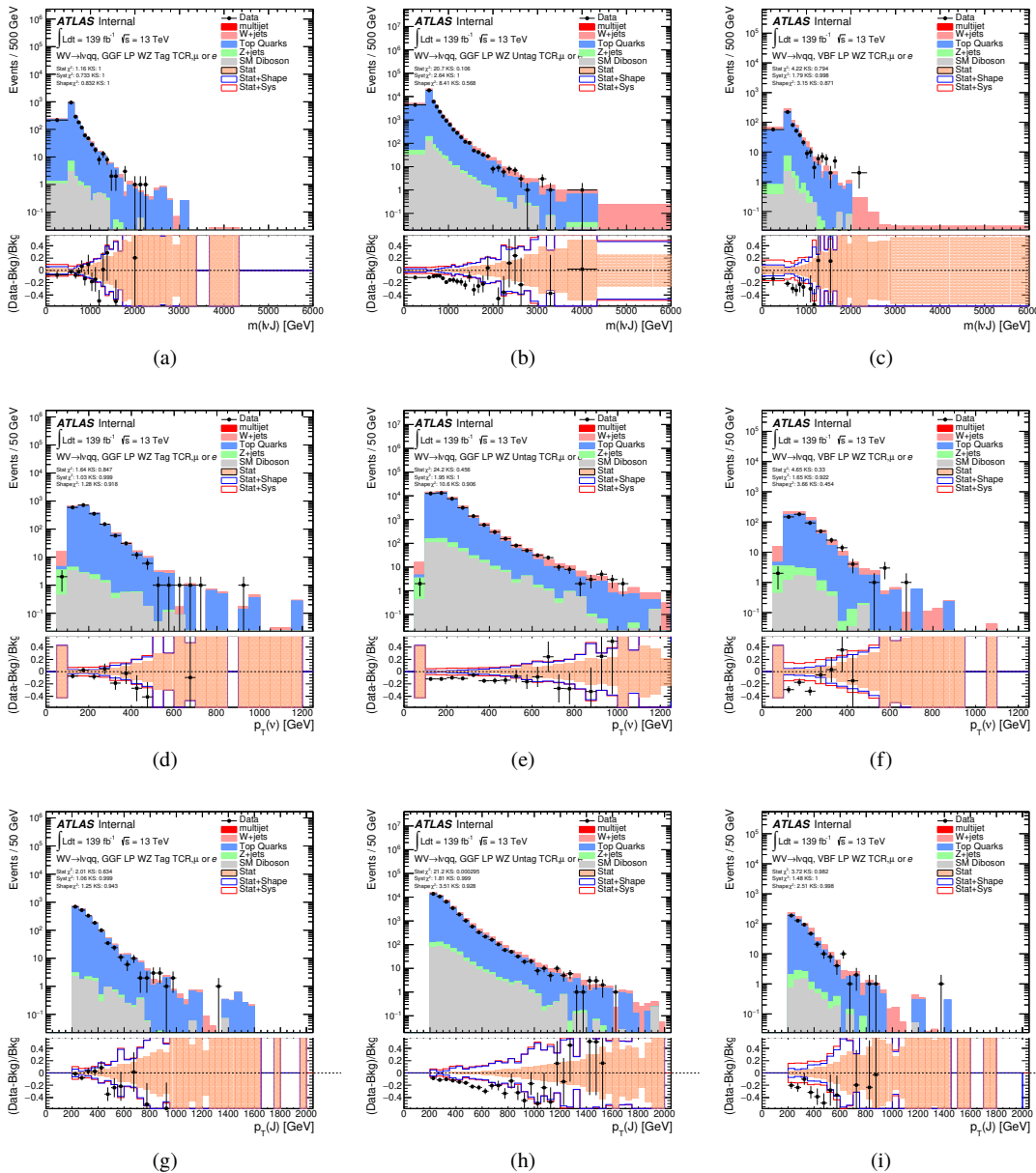


Figure 3.15: Data MC comparison for the merged WZ LP TCR.

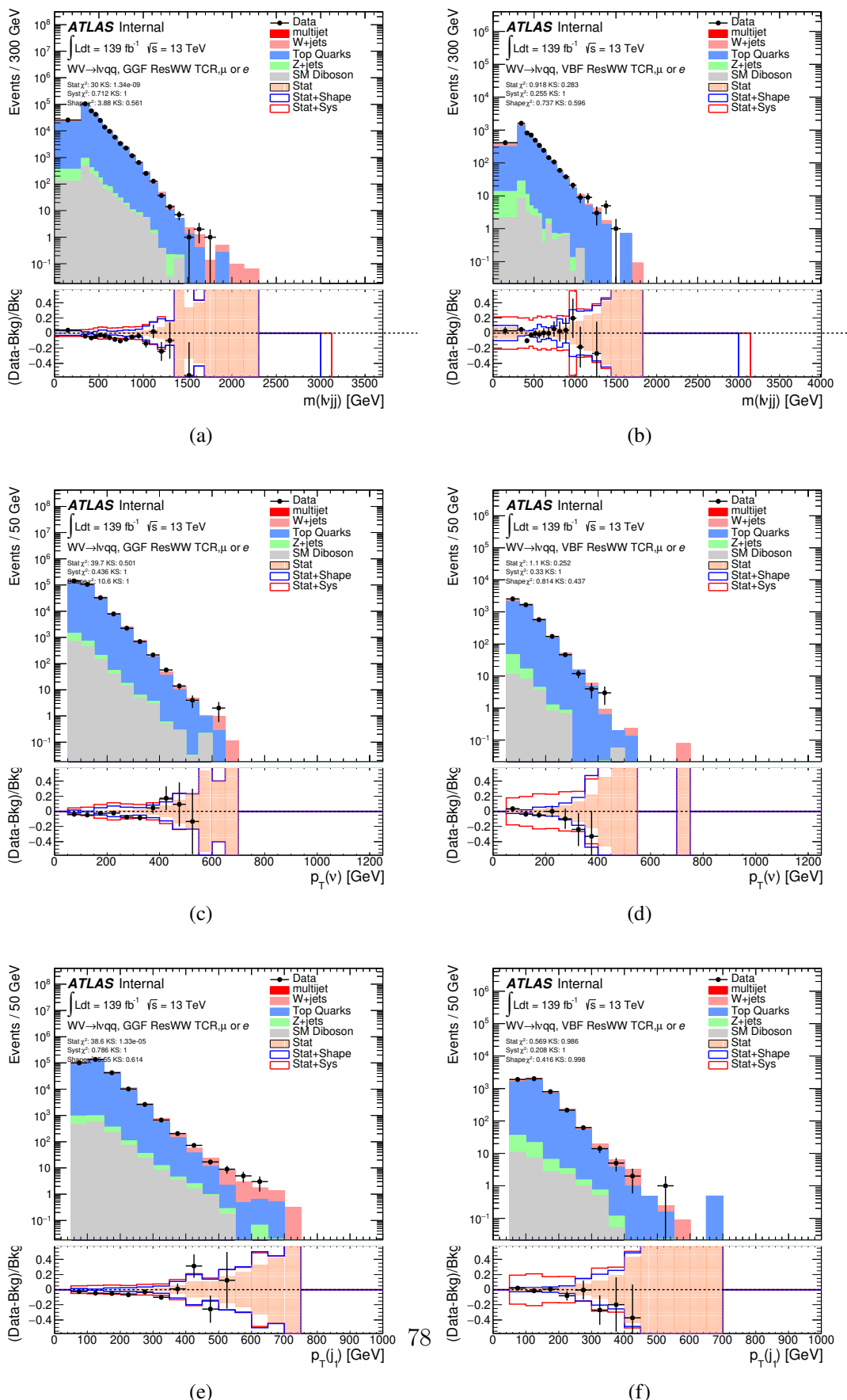


Figure 3.16: Data MC comparison for the resolved WW TCR.

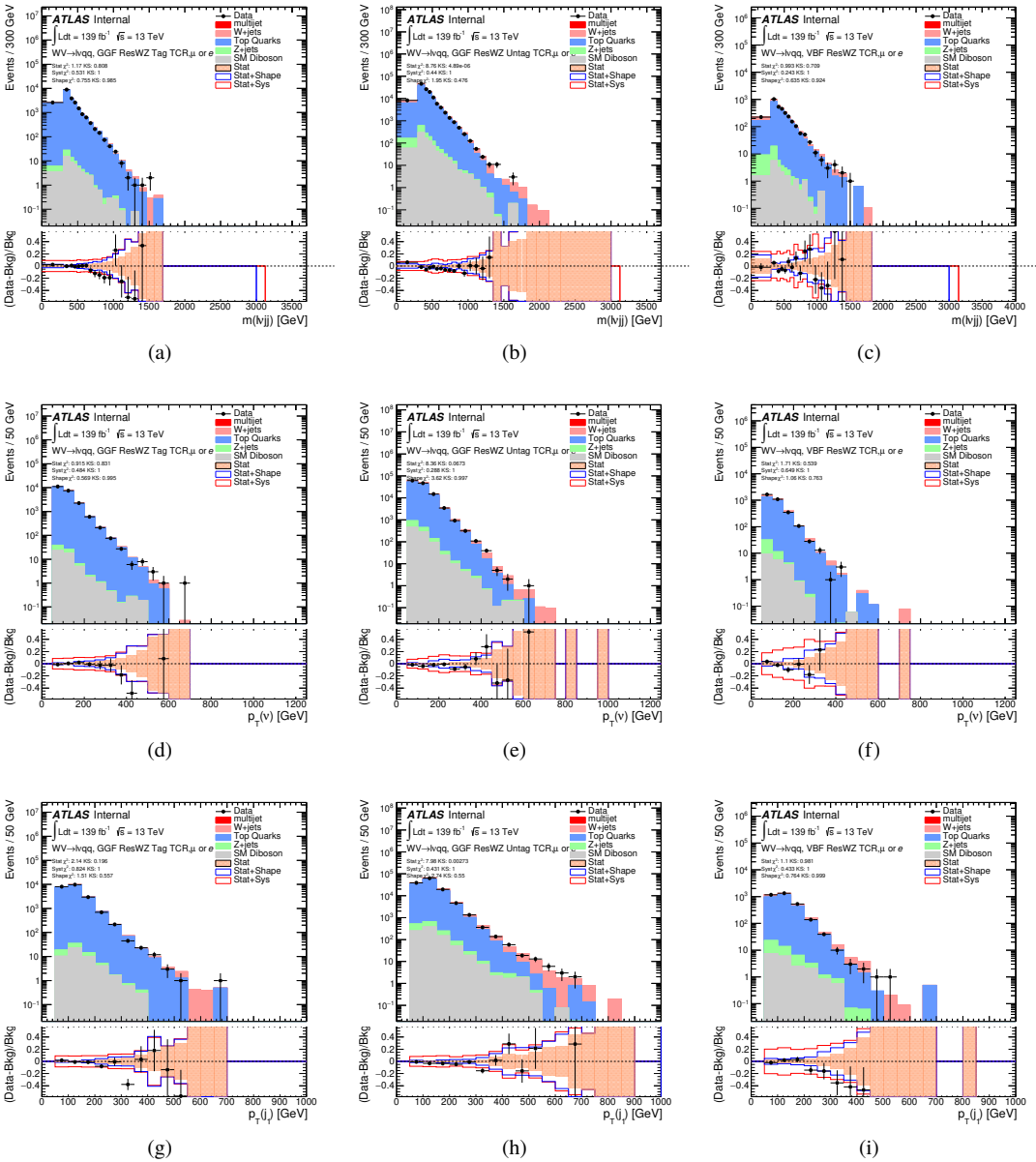


Figure 3.17: Data MC comparison for the resolved WZ TCR.

916 **3.4 Background Estimate**

917 **3.4.1 Multijet Sample**

918 Backgrounds in this analysis containing real leptons (e.g. $W/Z+jets$, diboson,
919 $t\bar{t}$, single- t) are well-modeled with simulated samples and constrained with data
920 from CRs. However, the multijet background containing fake leptons is not well-
921 modeled with simulation. For this reason, the multijet background is extracted
922 from data. Heavy flavor decay products, jets, and converted photons can be
923 mistakenly reconstructed as jets. Fake electrons often arise from jet fakes while
924 fake muons may also arise from heavy flavor decay. For this analysis, these fake
925 electrons generally fail the electron ID criteria and fake muons fail the muon
926 isolation requirement. Therefore, to derive the multijet template shape the SR
927 and CR selections and inverted lepton requirements are used as seen in Table
928 3.4. NB: by inverting the lepton isolation/identification criteria the CR and SRs
929 created are orthogonal to the CR and SRs.

930 The template shape of the MJ background is determined by using a multijet
931 validation region (MJVR) that requires the inverted lepton isolation/id require-
932 ment and the two signal jets to satisfy the m_{jj} requirement used in the $W+jets$
933 CRs. The E_T^{miss} distribution in MJCR is shown in Figure 3.18 for 2017 data.
934 The template is then extracted by subtracting the data in the MJVR from the
935 electroweak background processes. This template is then added in the WCR
936 and a "pre-MJ-fit" is preformed. In this fit the E_T^{miss} distribution is fit with the
937 electroweak background normalizations constrained to expected ranges and the
938 multijet electron and muon background normalizations free to float. The fitted
939 scale factors from this MJVR template are then applied in the MJCR template.
940 The fitted uncertainties on the MJCR normalizations are then used to create the

941 MJ template in the SRs. The electron and muon background normalizations are
 942 parameters in the final simultaneous fit. Technically, there should be a separate
 943 template for every CR and SR, but some MJ regions have insufficient statistics to
 944 do this. Additionally, the shapes for the MJ templates for VBF and ggF regions
 945 are found to be compatible within statistical uncertainty. Therefore, the sample
 946 MJ template used for VBF and ggF CR/SRs, but with different pre-MJ-fit scale
 947 factors.

948 This template method was validated using WCR and full Run 2 data. The
 949 results of the fit are shown in Table 3.5. The multijet contribution in the muon
 950 channel for $p_T^W > 150$ GeV is consistent with zero, and therefore neglected in
 951 the final fit. Applying the extracted normalization factor to MJVR in WCRs for
 952 various kinematic variables such as E_T^{miss} , W transverse mass, lepton p_T , and the
 953 invariant mass as show in Figures 3.19 -3.28. These figures show good agreement
 954 between the data and background estimate.

	Criterion	signal lepton	inverted lepton
Electron	ID	TightLH	MediumLH !TightLH
	Calo Isolation	FixedCutHighPtCaloOnlyIso	FixedCutHighPtCaloOnlyIso
Muon	ID	WHSignalMuon	WHSignalMuon
	Track Isolation	FixedCutTightTrackOnlyIso	!FixedCutTightTrackOnlyIso $ptvarcone30/pt < 0.07^*$
*Only applied to events with $pTW < 150GeV$			

Table 3.4: Definitions of “inverted” leptons used in multijet control region

955

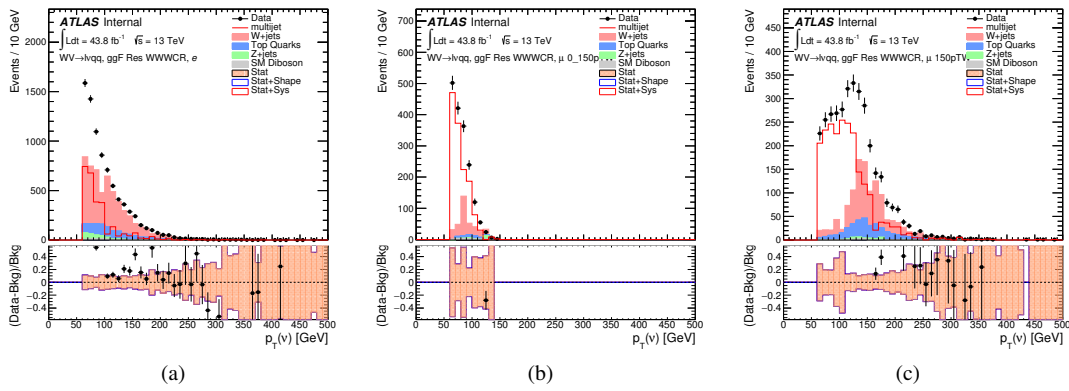


Figure 3.18: The E_T^{miss} distribution in MJCR for 2017 data in the electron channel(left), muon channel with $p_T < 150$ GeV (center) and > 150 GeV (right). Multi-jet templates are calculated as remaining data components after excluding known MC

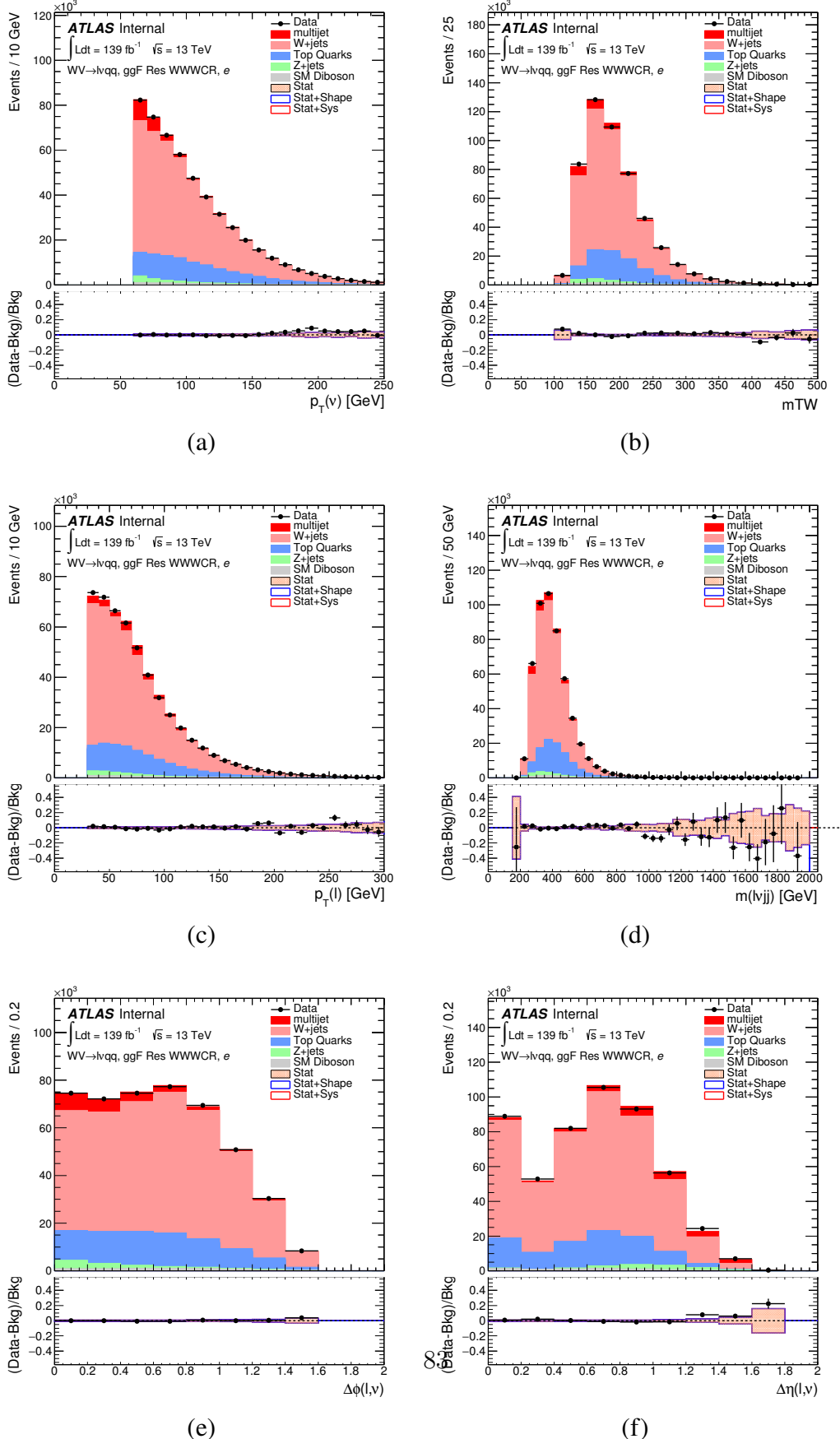


Figure 3.19: Postfit Data/MC comparison of distributions of E_T^{miss} , m_T^W , lepton

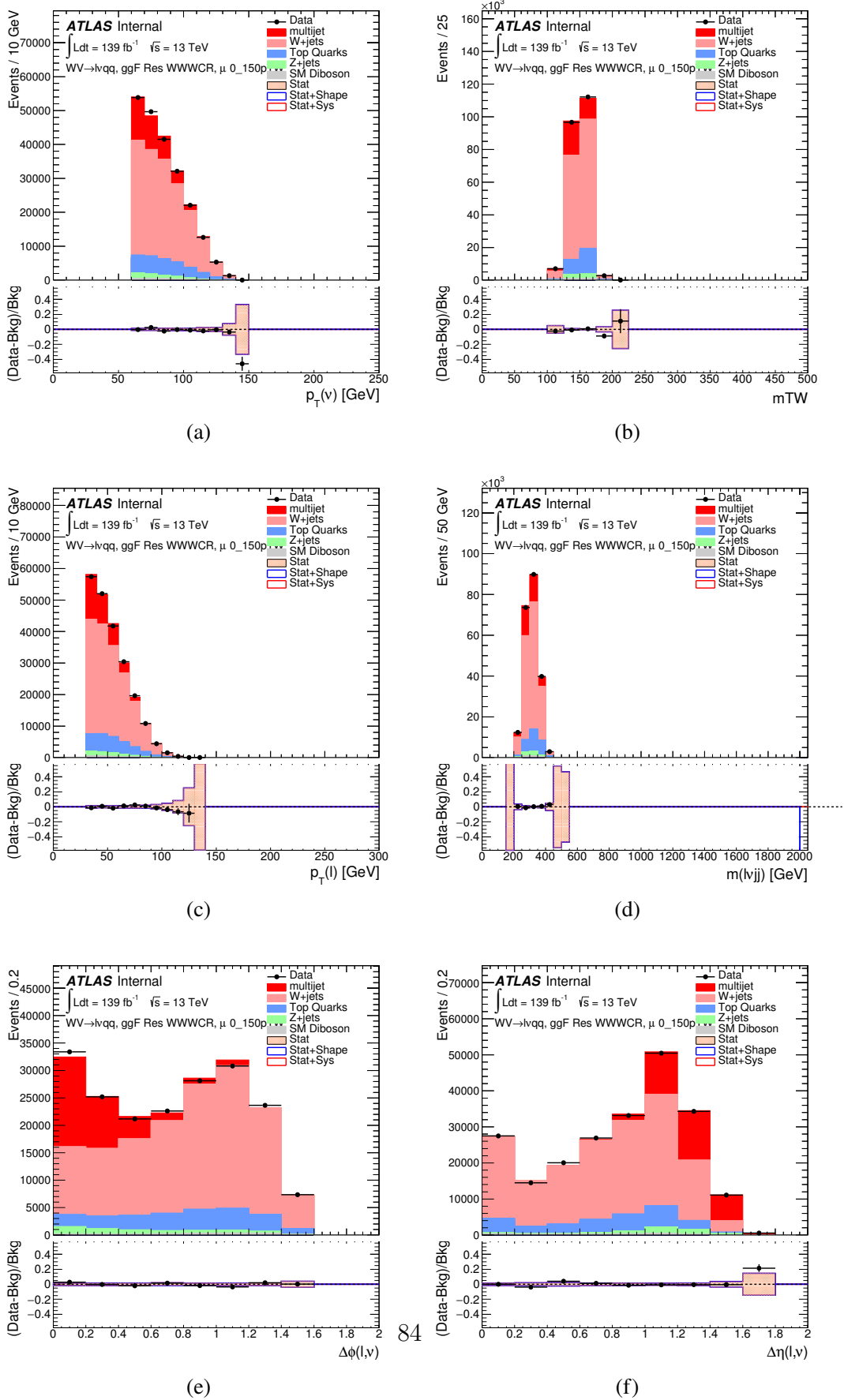
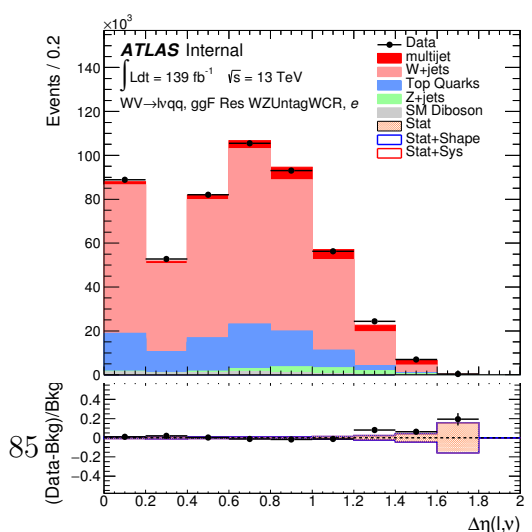
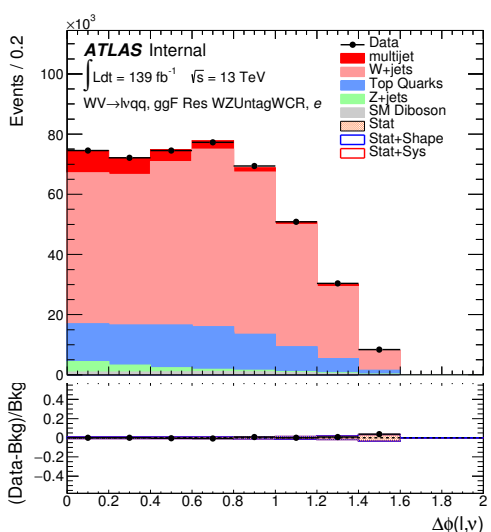
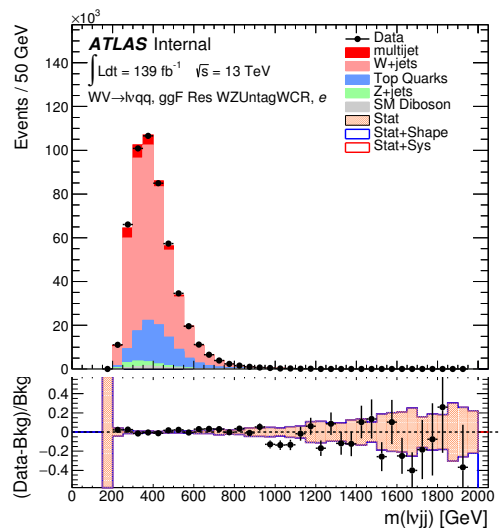
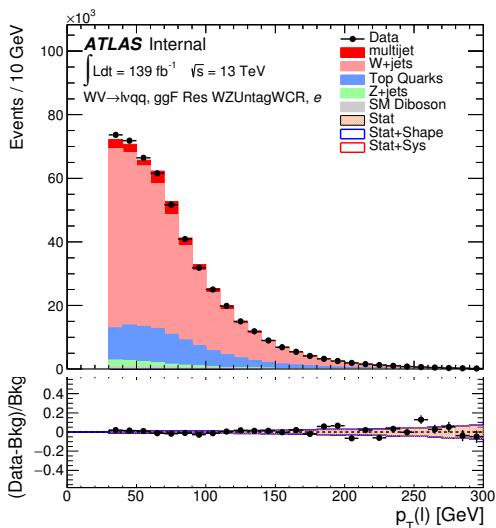
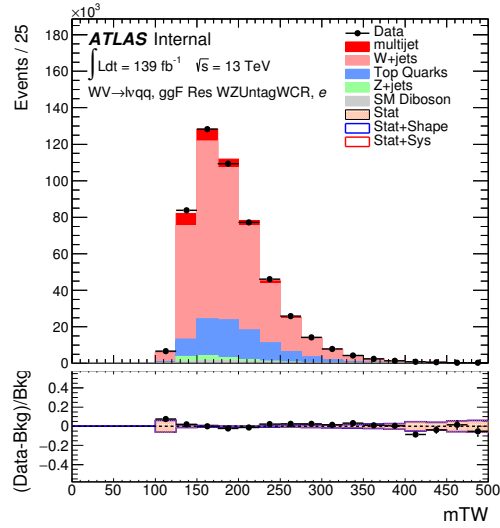
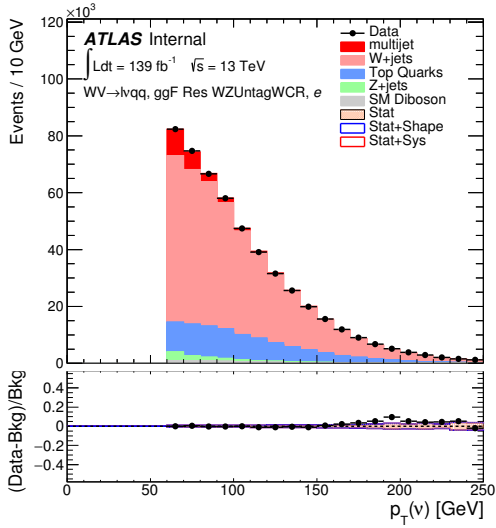


Figure 3.20: Postfit Data/MC comparison of distributions of E_T^{miss} , m_T^W , lepton and neutrino p_T , $m_{l_{jj}}$, lepton- ν angular distance in the WW muon channel. The



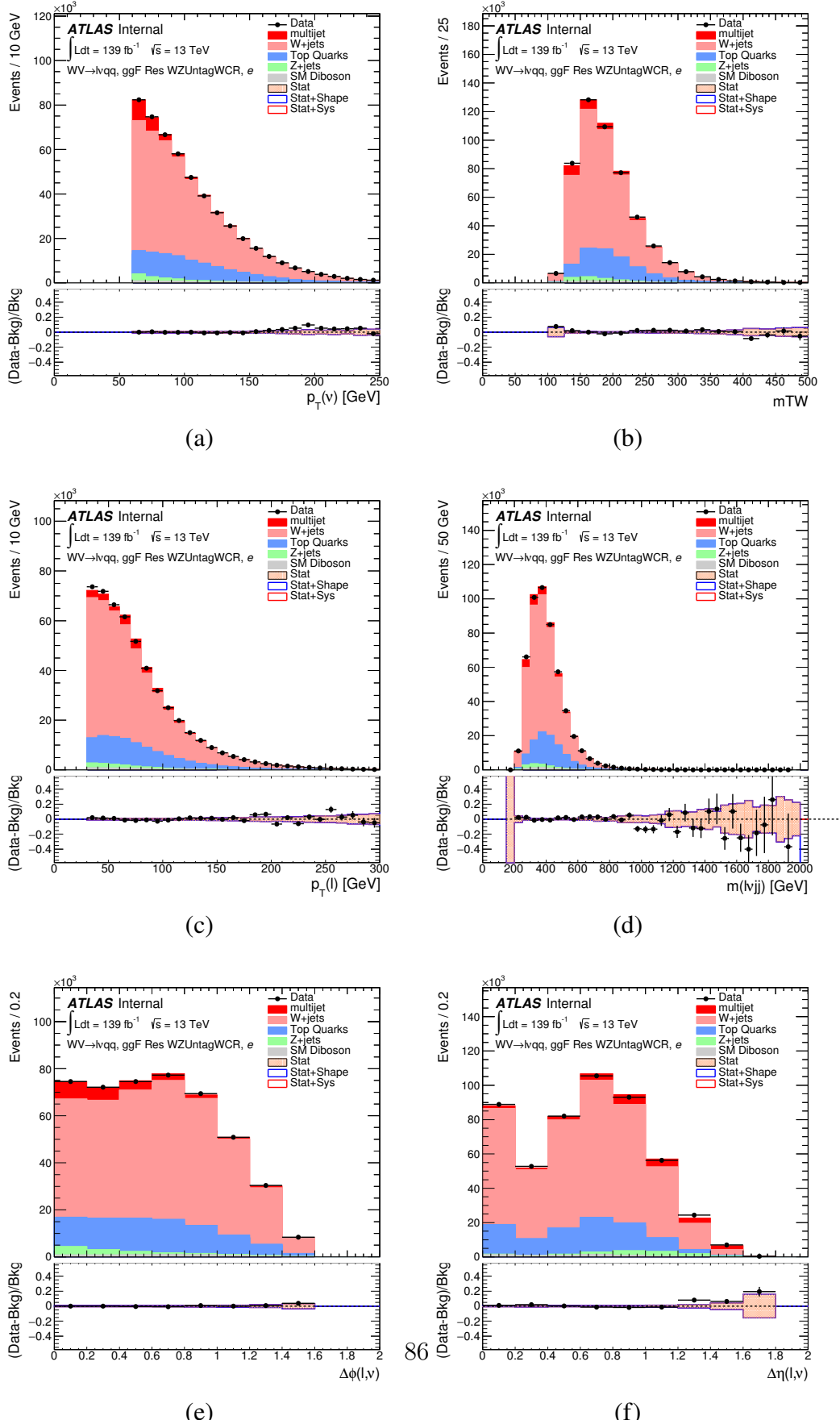
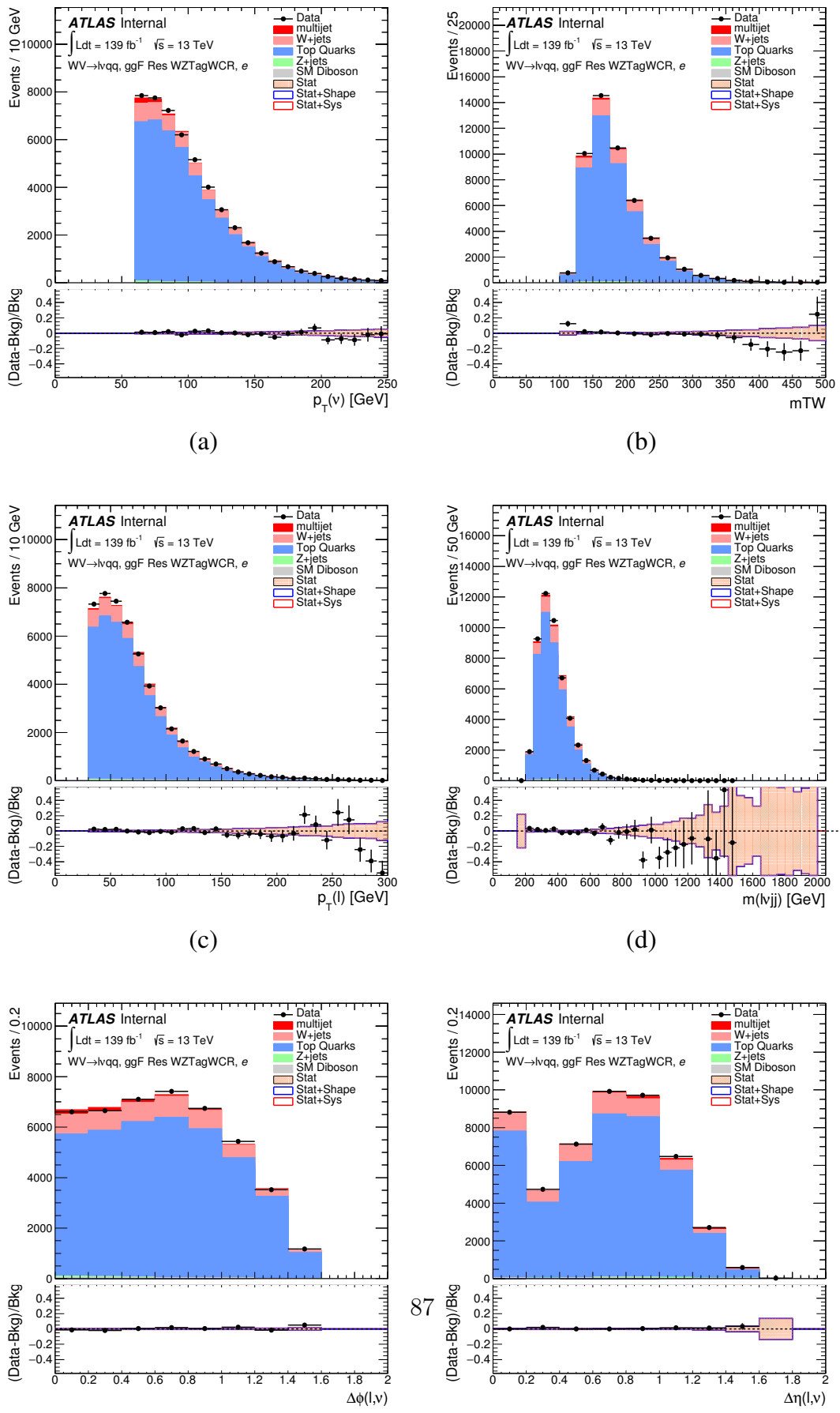
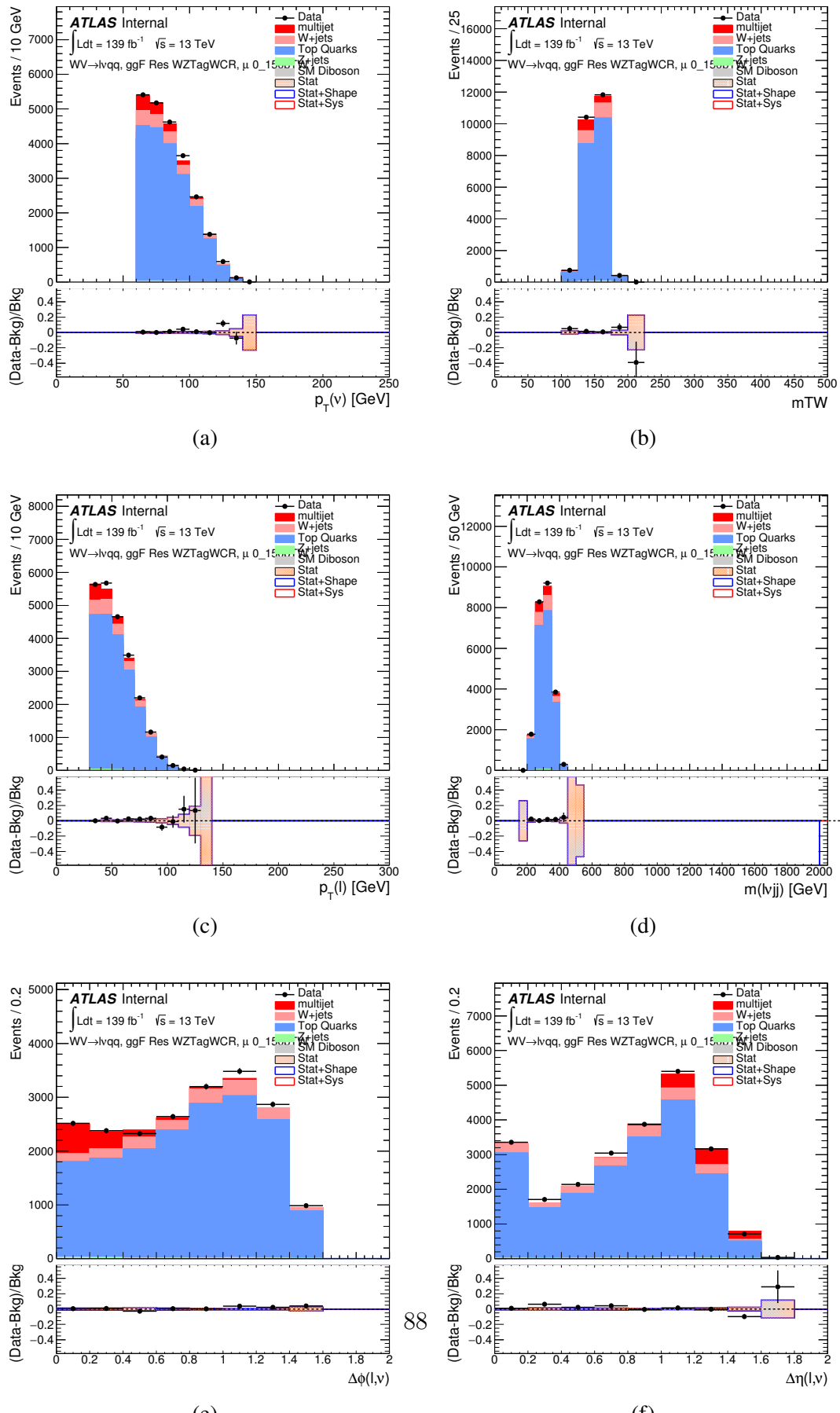
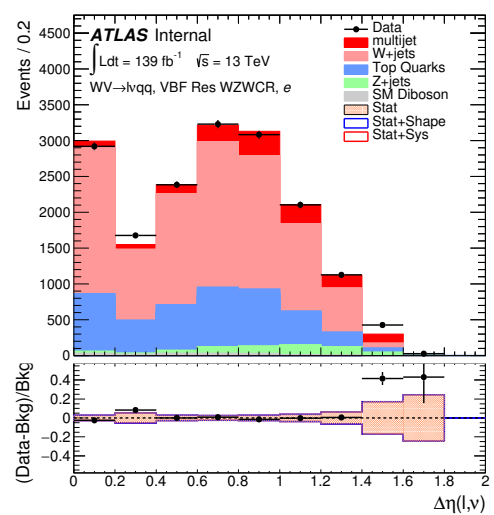
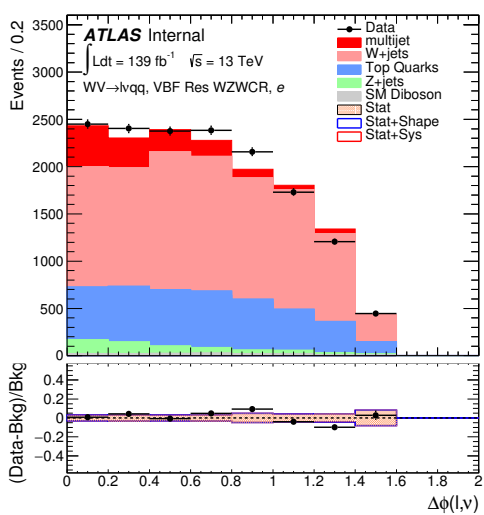
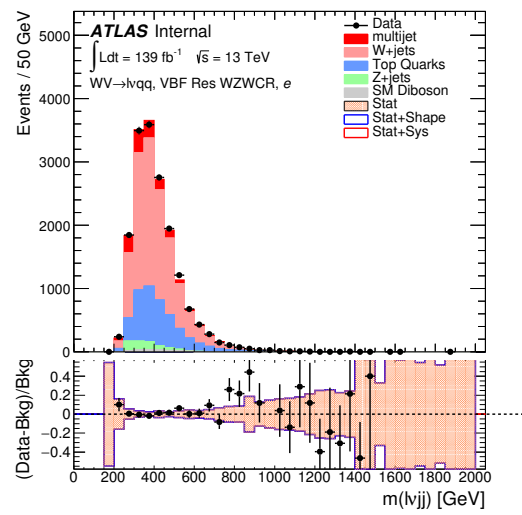
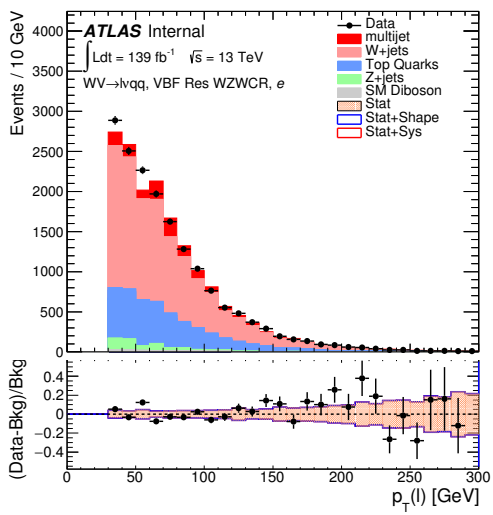
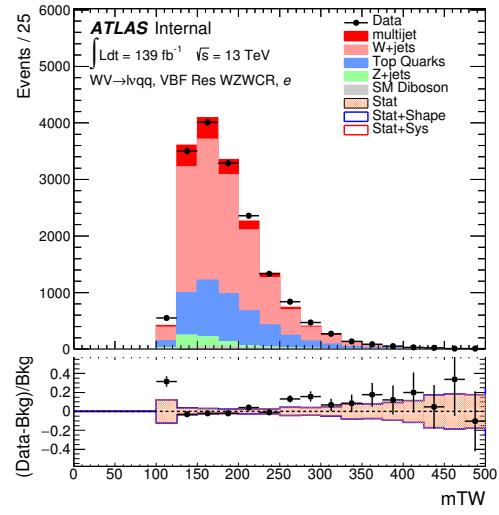
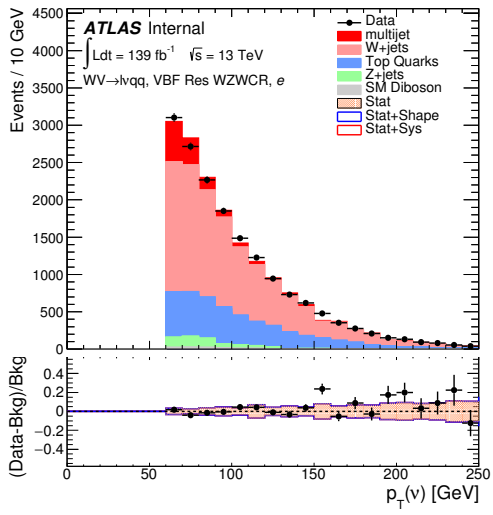
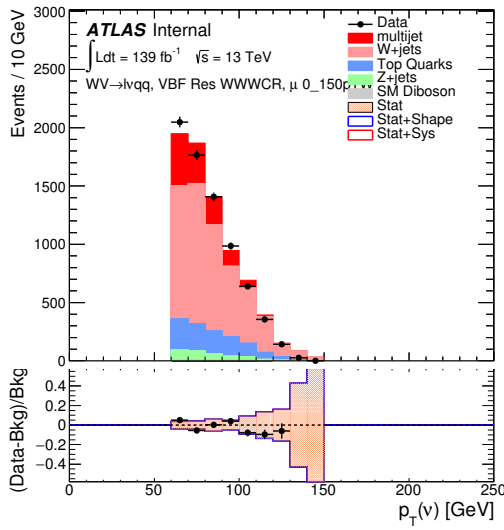


Figure 3.22: Postfit Data/MC comparison of distributions of E_T^{miss} , m_T^W , lepton

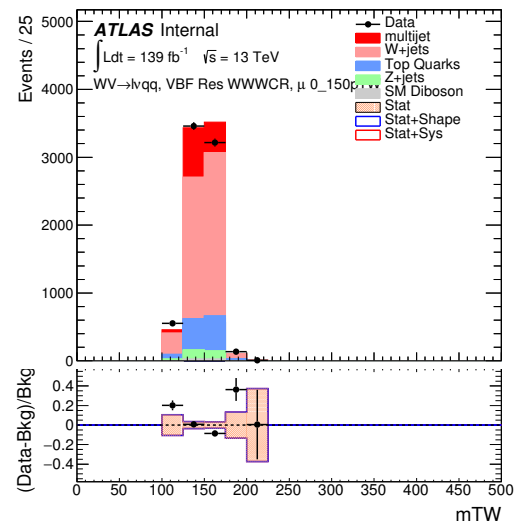




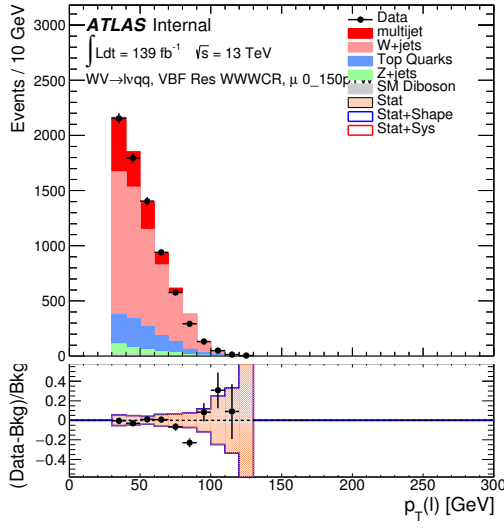




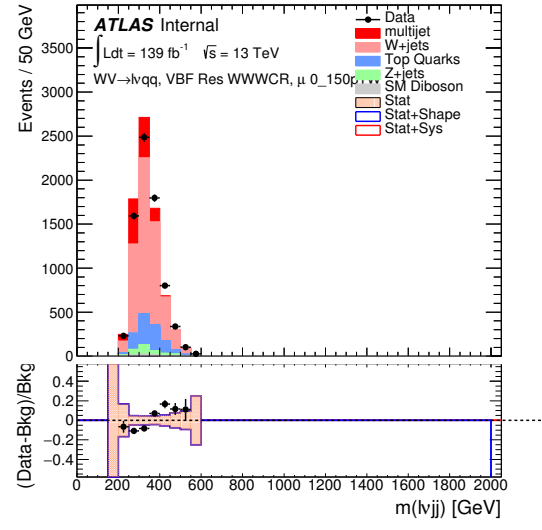
(a)



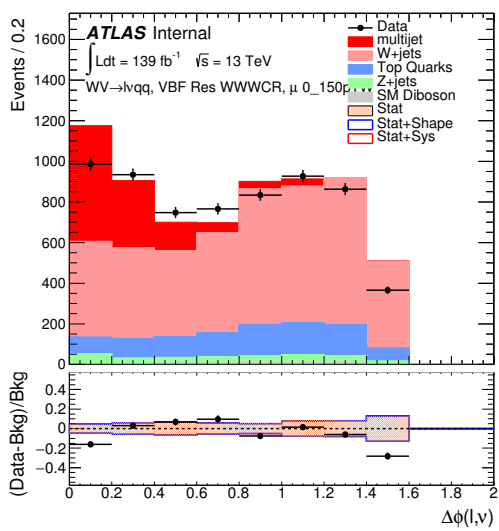
(b)



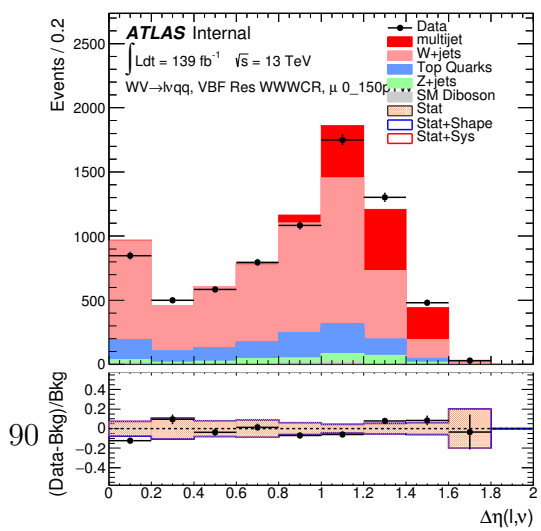
(c)



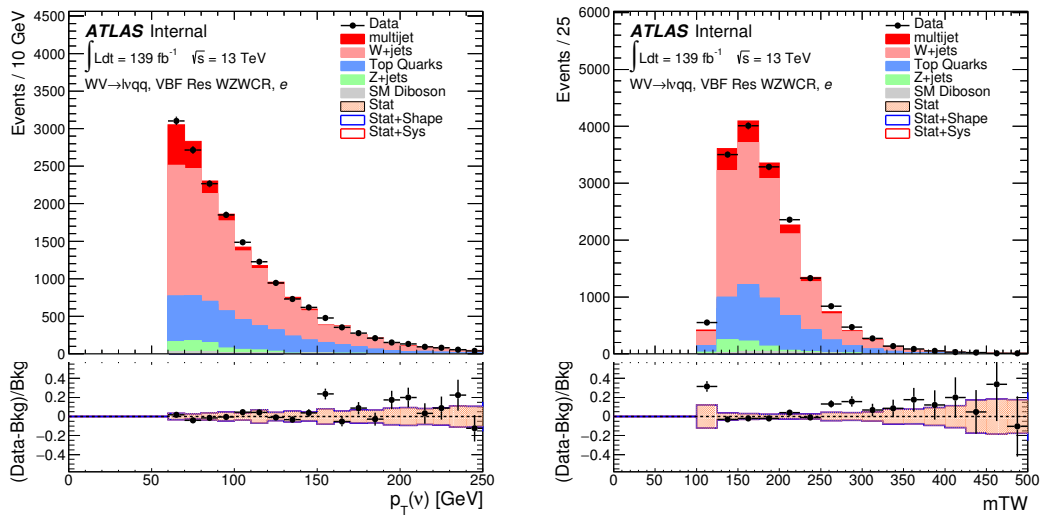
(d)



(e)

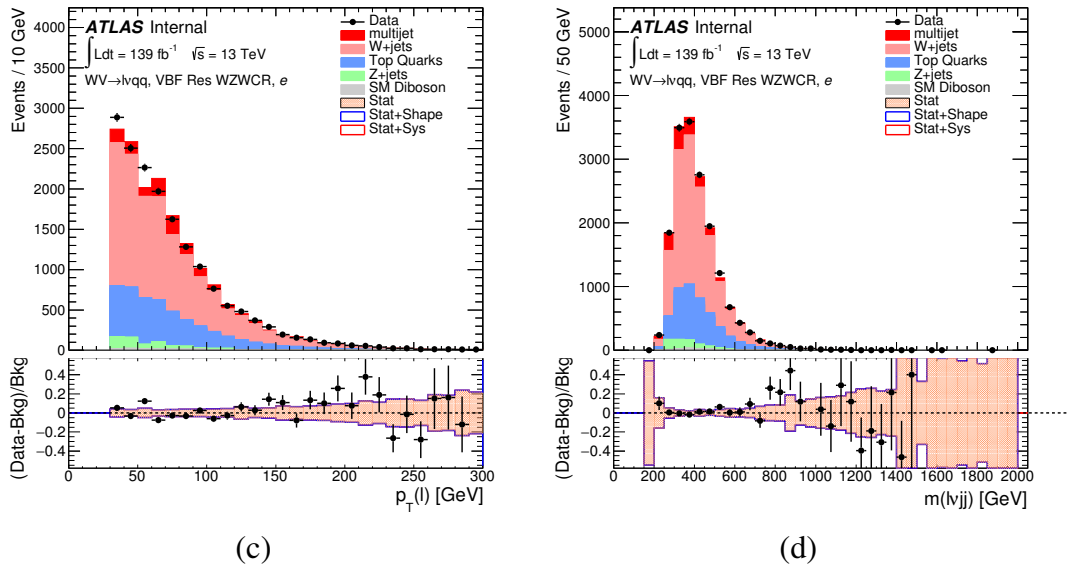


(f)



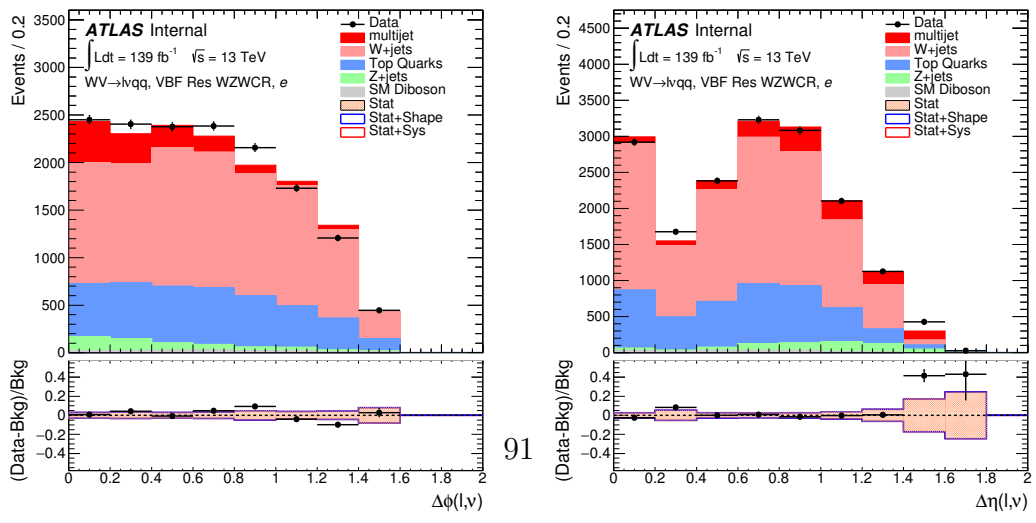
(a)

(b)



(c)

(d)



(e)

(f)

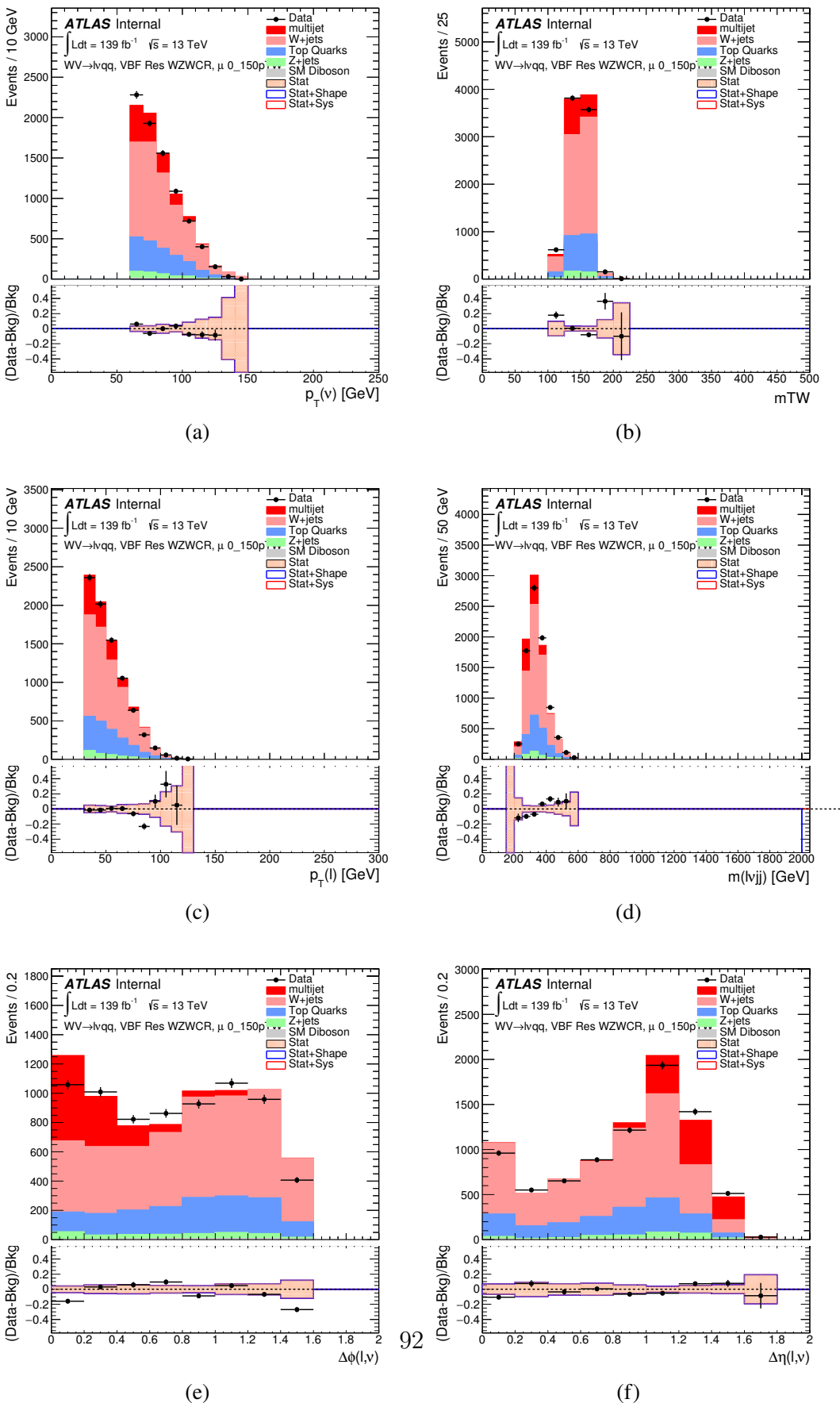


Figure 3.28: Postfit Data/MC comparison of distributions of E_T^{miss} , m_T^W , lepton

956 **3.5 Systematics**

957 This section describes the sources of systematic uncertainties considered in
958 this analysis. These uncertainties are divided into three categories: experimental
959 uncertainties, background modeling uncertainties, and theoretical uncertainties on
960 signal processes. In the statistical analysis each systematic uncertainty is treated
961 as a nuisance parameter estimated on the m_{VV} distribution.

962 **3.5.1 Experimental Systematics**

963 The uncertainty on the integrated luminosity of the dataset used is 1.7% and
964 a systematic in the final fit. The luminosity uncertainty is calculated following a
965 methodology similar to the one in [ref P55].

966 Also, multiple pile up interactions are simulated to match data conditions.
967 This ensures simulated detector response and particle reconstruction conditions
968 are as similar as possible. The distribution of the average number of interactions
969 per bunch crossing applied to simulation is called the μ profile. The pileup mod-
970 eling uncertainty is accounted for by re-weighting simulated events so the average
971 number of interactions per bunch crossing varies within its uncertainty due to
972 systematics from vertex reconstruction [ref ATL-COM-SOFT-2015-119]. The as-
973 sociated re-weighting factors are propagated through the entire analysis chain to
974 construct a systematic uncertainty on m_{VV} .

975 The single-lepton and E_T^{miss} triggers used are not fully efficient and therefore
976 simulated data must be scaled to account for trigger inefficiencies. Trigger effi-
977 ciencies are given by the ratio of the distribution of offline objects before trigger
978 selection and after trigger selection.

979 Uncertainties on small-R jet energy scale and resolution are measured in-situ
980 by calculating the response between data and simulation. This analysis uses a

981 reduced set of JES and JER uncertainties (totaling 30 and 8 systematics, re-
982 spectively). These reduced sets of systematics are calculated using a principal
983 component analysis, yield largely uncorrelated independent systematics. These
984 uncertainties account for the dependence on p_T , η , μ , flavor response and global
985 sequential corrections. Systematic uncertainties associated with b -tagging are also
986 considered. These systematics are evaluated as uncertainties on the scale factor
987 which account for the difference in b -tagging efficiencies in data and MC, and the
988 flavor dependence (between b, c, and light jets).

989 The uncertainty on the p_T scale of the large-R jets is determined by comparing
990 the jet's p_T^{calo} to p_T^{track} in di-jet simulation and data. In addition to this uncertain-
991 ties from tracking, modeling (Pythia vs Herwig), and statistical constraints are
992 also calculated. The large-R jet p_T resolution is given by smearing the jet p_T with
993 a Gaussian with a 2% width.

994 The W/Z -tagging efficiency cannot be evaluated using the Rtrk method as the
995 TCC algorithm uses track measurements to reconstruct jet substructure variables.
996 In order to avoid this potential bias, the W/Z -tagging estimated in data using a
997 control sample and correct by comparing it with simulation. The efficiency to
998 W/Z -induced signal is estimated by a $t\bar{t}$ control sample, while the efficiency to
999 single- q/g background is estimated using a dijet sample. The effects of experimen-
1000 tal and theoretical uncertainties on the efficiency scale factor are by taking the
1001 ratio of efficiencies in data and simulation. By taking this ratio the uncertainties
1002 not arising for jet mass and D_2 cancel.

1003 Lepton identification, reconstruction, isolation systematic uncertainties are de-
1004 termined by reconstructing the Z mass peak with a tag and probe method. The
1005 lepton energy and momentum scales are also measured with the Z mass peak.
1006 Additionally, the track-to-vertex association efficiency is used for muons.

1007 As E_T^{miss} is calculated using all the physics objects in the event, all those objects
1008 associated errors result in an uncertainty on E_T^{miss} . Additionally, the unassociated
1009 tracks used to construct E_T^{miss} contribute to the uncertainty on E_T^{miss} .

1010 **3.5.2 Theory Systematics**

1011 Theoretical uncertainties for signal and background processes arise from un-
1012 certainties in the parameters used in Monte Carlo simulation. In particular for
1013 the $t\bar{t}$, $W/Z + \text{jets}$, and diboson backgrounds and signal samples the QCD scale,
1014 PDF, generator and hadronization uncertainties were evaluated. To assess the
1015 QCD scale uncertainty the renormalization and factorization scales were scaled
1016 up (2.0) and down (0.5) at the event generation stage of sample production. Un-
1017 certainties due to the choice of the parton distribution functions were evaluated
1018 by re-weighting samples from the nominal PDF to a set of error PDFs which ac-
1019 count for the uncertainty of the fits used to produce the PDF set. In addition to
1020 this samples are re-weighted to different PDF sets to account for the arbitrariness
1021 of the PDF choice. The difference between the m_{WW} distributions using differ-
1022 ent event generators is assessed by comparing samples generated with different
1023 generators. Similarly, the uncertainty in hadronization models is account for by
1024 comparing samples created using different hadronization models (e.g. Pythia8 vs.
1025 Herwig7). Figures 3.30 - 3.36 show the impact of these uncertainties on the $t\bar{t}$
1026 and $W/Z + \text{jets}$ backgrounds.

1027 Additionally, contributions to the diboson background for the VBF analysis
1028 were included in [SOME WAY that is not determined yet].

1029 The normalization of the $t\bar{t}$ and $W + \text{jets}$ processes impact the multijet template
1030 shape. The impact of these normalization is assess by including a shape systematic
1031 on the multijet background from varying the $t\bar{t}$ and $W + \text{jets}$ normalization factors.

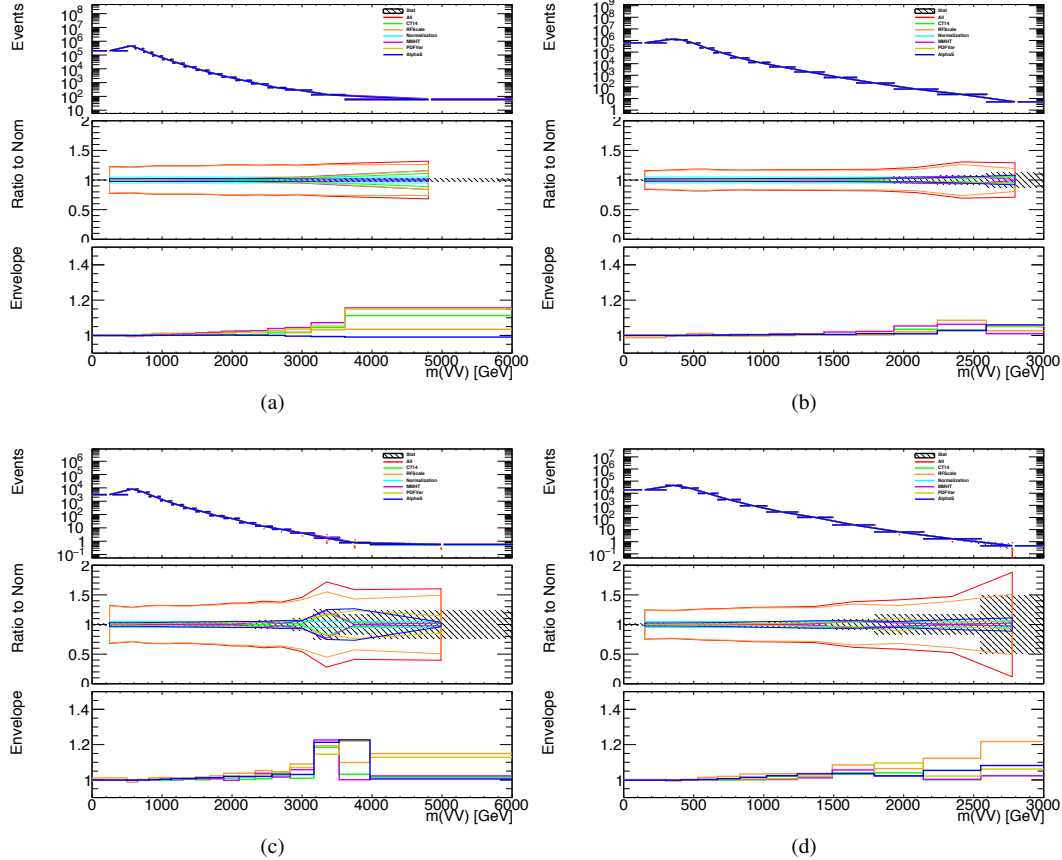


Figure 3.29: The $W/Z + \text{jet}$ systematics for the a) Merged ggF, b) Resolved ggF, c) Merged VBF, and d) Resolved VBF regions. The top subplot shows the nominal and variation distributions/bands, the middle shows the ratio of the two, and the final shows just the shape of the envelope (the final uncertainty).

Full Run 2
ggF Res WWWCR

Sample	Yield	R.U.	SF
Top&W	645040 ± 1971.68	0.31%	0.998
Z&VV	24075.9		fixed
MJ_el	24156.3 ± 1224.62	5.06%	3.973
MJ_mu	35528.5 ± 923.94	2.60%	9.019

ggF Res WZ01bWCR

Sample	Yield	R.U.	SF
Top&W	644690 ± 1981.4	0.31%	0.997
Z&VV	24075.9		fixed
MJ_el	24366.5 ± 1232.69	5.05%	3.874
MJ_mu	35528.5 ± 921.27	2.58%	8.746

ggF Res WZ2bWCR

Sample	Yield	R.U.	SF
Top&W	71236.5 ± 688.74	0.97%	1.031
Z&VV	518.5		fixed
MJ_el	595.63 ± 449.34	75.44%	0.094
MJ_mu	1196.9 ± 222.13	18.56%	0.294

VBF Res WWWCR

Sample	Yield	R.U.	SF
Top&W	19032.3 ± 364.43	1.91%	0.928
Z&VV	1091.63		fixed
MJ_el	1425.73 ± 214.42	15.03%	0.235
MJ_mu	1281.36 ± 157.21	11.83%	0.314

VBF Res WZWCR

Sample	Yield	R.U.	SF
Top&W	21341.8 ± 392.21	1.84%	0.942
Z&VV	1111.75		fixed
MJ_el	1413.76 ± 230.36	16.29%	0.225
MJ_mu	1281.36 ± 157.21	12.27%	0.314

Table 3.5: Fit validation result in WCRs for 2015+16 data. The fit is done in various WCRs, in order to obtain the corresponding scale factors for MJ templates: ggF resolved WCR for the $WW \rightarrow lvqq$ selection, ggF resolved untagged WCR for the $WZ \rightarrow lvqq$ selection, ggF resolved tagged WCR for the $WZ \rightarrow lvqq$ selection, VBF resolved WCR for the $WW \rightarrow lvqq$ selection, and VBF resolved WCR for the $WZ \rightarrow lvqq$ selection. Post-fit event yields for electroweak processes and MJ contributions are shown. The SF column shows the corresponding normalization scale factors for electroweak processes from the fit. R.U. stands for relative uncertainty.

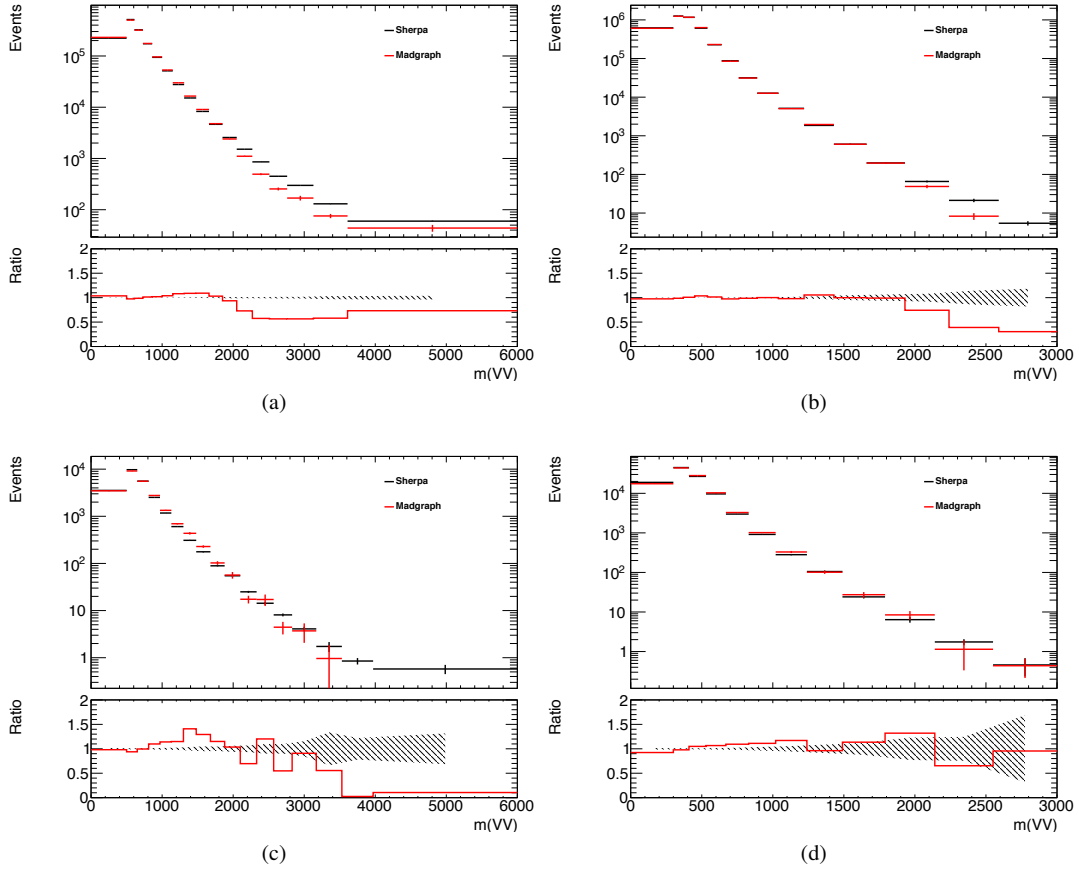


Figure 3.30: The two-point generator comparison between Sherpa and MadGraph for the $W/Z + \text{jet}$ samples in the a) Merged ggF, b) Resolved ggF, c) Merged VBF, and d) Resolved VBF regions. The normalization of the Madgraph sample is set to the Sherpa value to consider only shape effects. The bottom inset shows the ratio of the two.

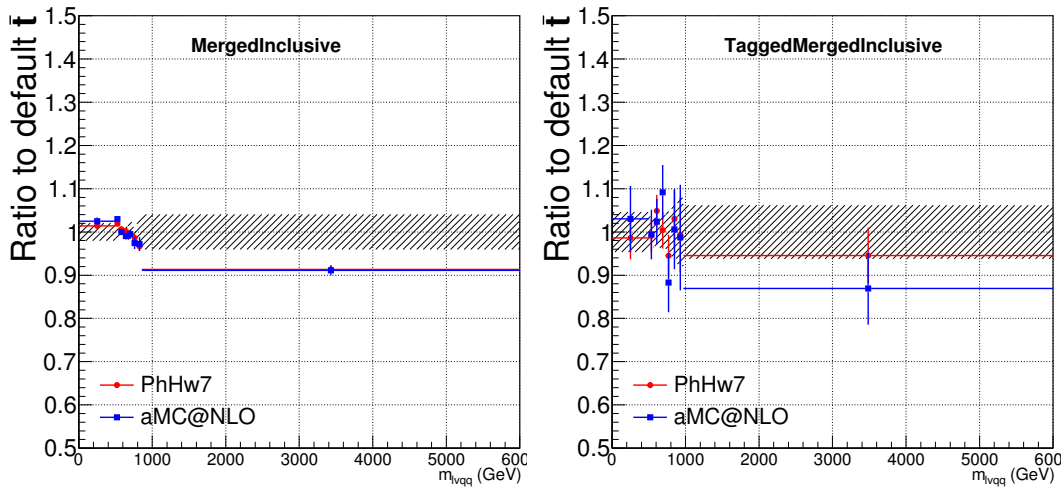


Figure 3.31: Ratio between the variations of generator (red) and hadronization (blue) variations for the Merged regime for $t\bar{t}$ sample.

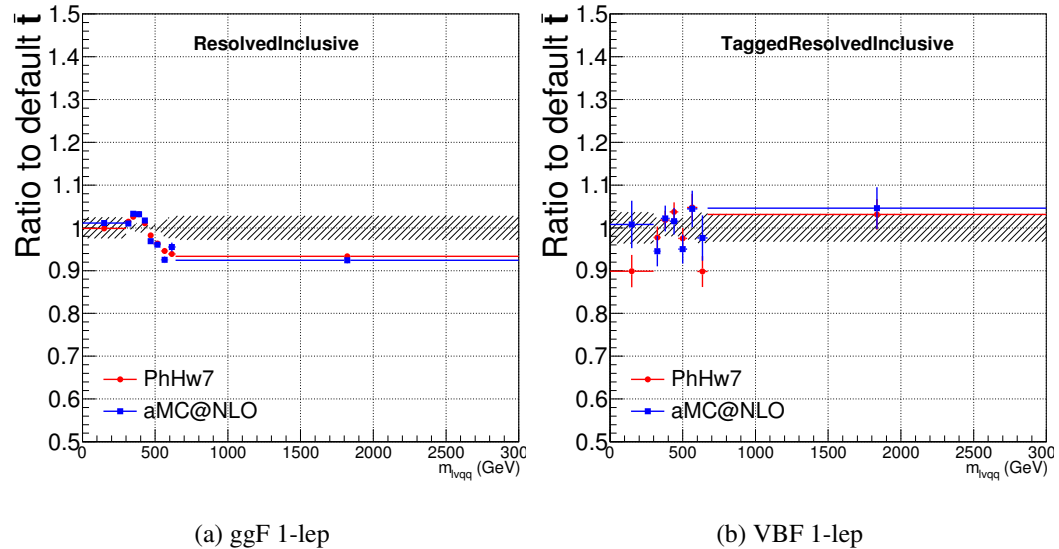


Figure 3.32: Ratio between the variations of generator (red) and hadronization (blue) variations for the Resolved regime for $t\bar{t}$ sample.

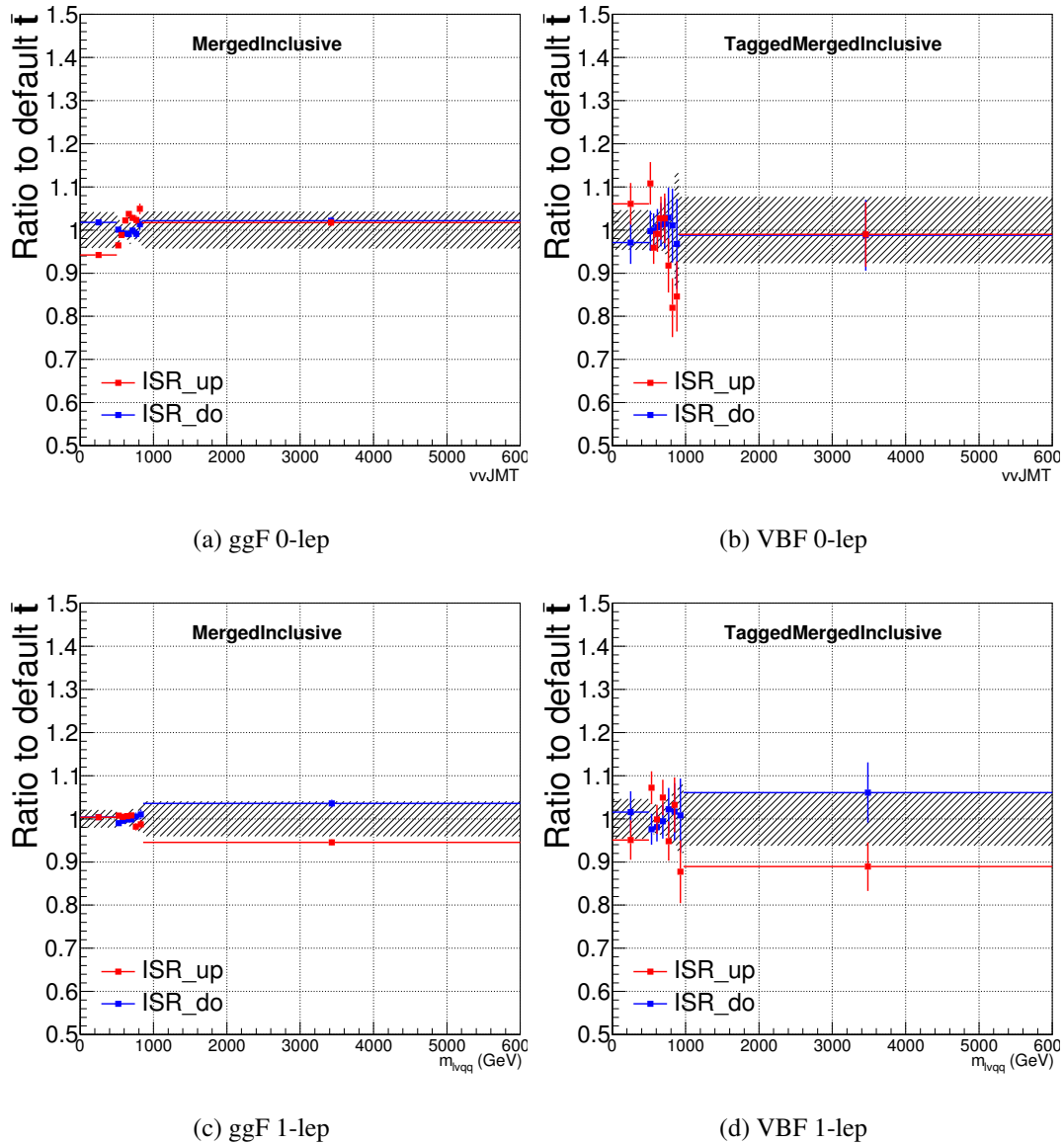


Figure 3.33: Ratio between the variations of ISR up (red) and down (blue) variations for the Merged regime for $t\bar{t}$ sample.

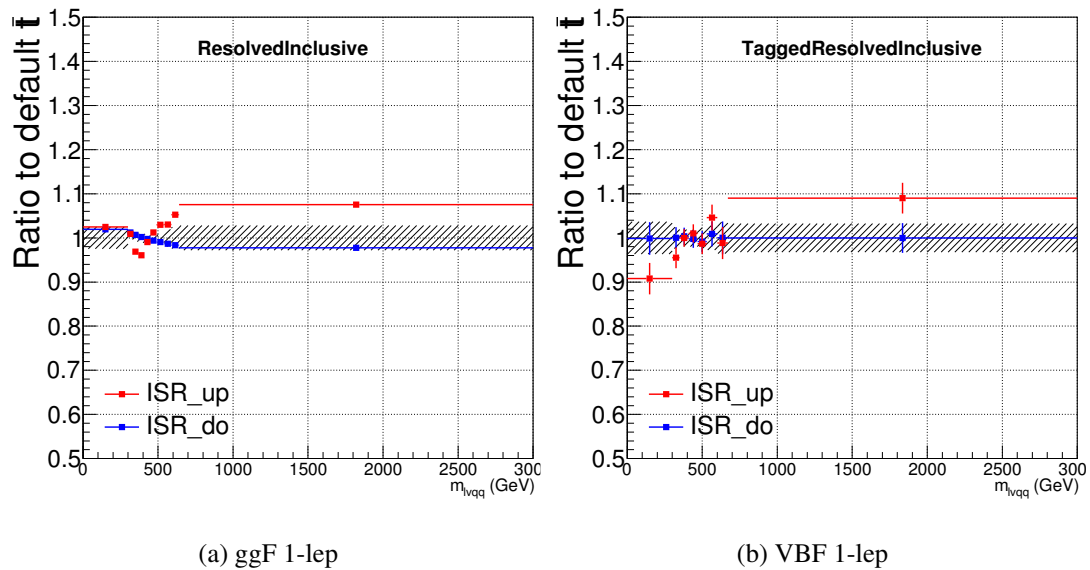


Figure 3.34: Ratio between the variations of ISR up (red) and down (blue) variations for the Resolved regime for $t\bar{t}$ sample.

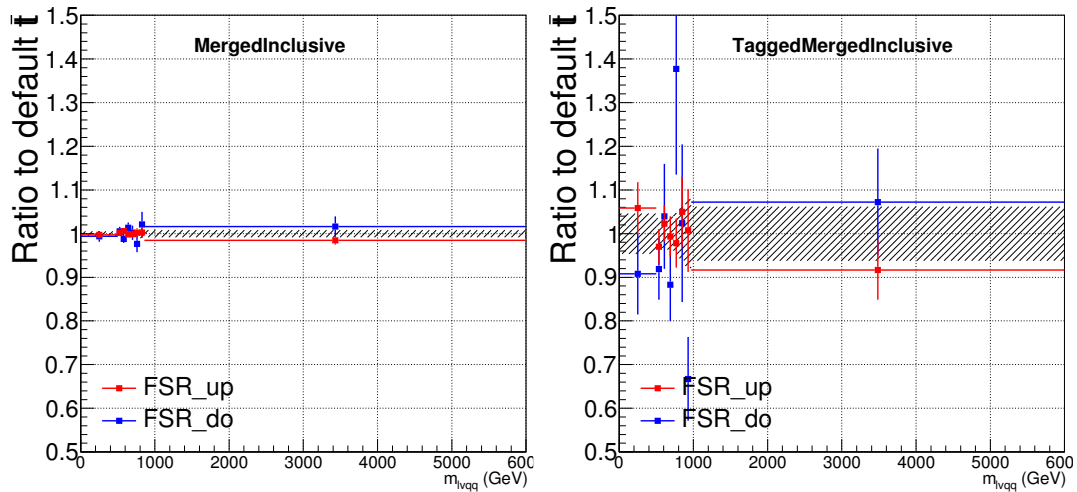
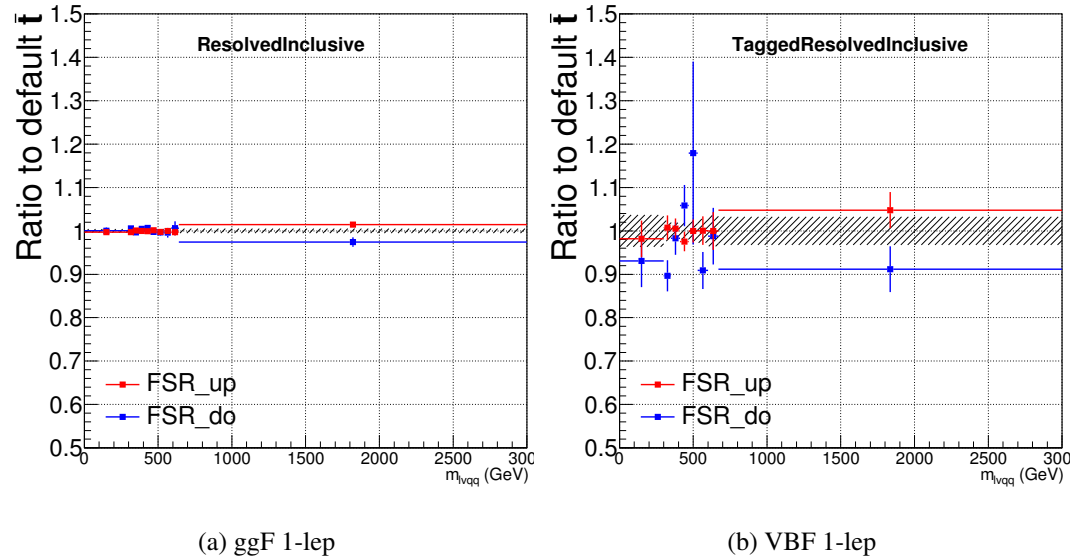


Figure 3.35: Ratio between the variations of FSR up (red) and down (blue) variations for the Merged regime for $t\bar{t}$ sample.



(a) ggF 1-lep

(b) VBF 1-lep

Figure 3.36: Ratio between the variations of FSR up (red) and down (blue) variations for the Resolved regime for $t\bar{t}$ sample.

1032 **3.6 Statistical Analysis**

1033 In the absence of discovery, upper limits on the signal strength parameter, μ ,
1034 are assessed using the CLs method. Specifically, a binned likelihood constructed
1035 from Poisson probabilities and systematic constraints is evaluated:

$$\mathcal{L}(\mu, \vec{\theta}) = \prod_c \prod_i Pois(n_{c_i}^{obs} | n_{c_i}^{sig}(\mu, \vec{\theta}) + n_{c_i}^{bkg}(\vec{\theta})) \prod_k (\theta'_k | \theta_k) \quad (3.8)$$

1036 where μ , a signal strength parameter, multiplies the expected signal yield for a
1037 given benchmark set of parameters $n_{c_i}^{sig}$ in each histogram bin i of the discriminant
1038 from channel c and n_b^{bkg} represents the background content for bin i from channel
1039 c . The dependence of signal and background predictions on systematic uncertain-
1040 ties is described by the aforementioned set of nuisance parameters $\vec{\theta}$, which are
1041 parameterized by Gaussian or log-normal priors denoted here as f_k . Statistical
1042 uncertainties of the simulated bin contents are also included as systematic un-
1043 certainties. Most systematics are correlated among all the analysis regions and
1044 considered to be independent from each other. The validity of this assumption
1045 is checked by evaluating the covariance of nuisance parameters (plots later). The
1046 The nominal fit results in terms of μ and θ_μ are obtained from maximizing the
1047 likelihood function with respect to all parameters. The test statistic, q_μ , is then
1048 constructed as:

$$q_\mu = -2 \frac{\mathcal{L}(\mu, \hat{\theta}_\mu)}{\mathcal{L}l(\hat{\mu}, \hat{\theta})} \quad (3.9)$$

1049 where $\hat{\mu}$ and $\hat{\theta}$ are the parameter values that maximize the likelihood and $\hat{\theta}_\mu$
1050 are the nuisance parameter values that maximize the likelihood for a given μ .
1051 As defined, larger values of q_μ correspond to increasing incompatibility between
1052 the observed data and the background + signal hypothesis. The observed value
1053 of the test statistic, $q_{\mu,obs}$, is then compared to its expected distribution, f_k , to

1054 calculate p-values to assess the likelihood of the background+signal hypothesis.

1055 Using these distributions, CL_s values are computed as:

$$CL_{s+b} = \int_{q_{\mu,obs}}^{\infty} f(q_{\mu}|\mu) dq_{\mu} \quad (3.10)$$

$$CL_b = \int_{q_0^{obs}}^{\infty} f(q_{\mu}|\mu = 0) dq_{\mu} \quad (3.11)$$

$$CL_s = \frac{CL_{s+b}}{CL_b} \quad (3.12)$$

1058 CL_{s+b} is the p-value for the signal + background hypothesis and CL_b is the
1059 p-value for the background only hypothesis. The CL_s value is interpreted as
1060 the probability to observe the background + signal hypothesis normalized to the
1061 probability of background-only hypothesis. Normalizing by CL_b prevents setting
1062 artificially strong exclusion limits due to downward fluctuations in data.

1063 In this analysis, μ values are scanned for each bin in the fit to find the μ value
1064 that yields $CL_s=0.05$, meaning the likelihood of finding data more incompatible
1065 with the signal+background hypothesis (relative to the background only hypoth-
1066 esis) is 5%. The 95% upper limit on the cross section is then calculated as the
1067 product of the μ value found, branching ratio, and theory cross section.

1068 Fit Configuration

1069 For this analysis, each signal model is fit simultaneously with for the Merged
1070 and Resolved channels from VBF and DY production. The WCR and TCR are
1071 used to extract the normalizations for the $W+jets$ and $t\bar{t}$ backgrounds in the
1072 SRs. The binning is in [Natasha add binning table]. The binning is set by signal
1073 resolution and stats. Additionally, talk about NP correlations [Natasha].

1074 Systematics may be affected by low statistics, leading to unsmooth m_{VV} dis-
1075 tributions with unphysically large fluctuations. This can lead to artificial pulls and

1076 constraints in the fit. To remove such issues a multi-step smoothing procedure
1077 is applied to all systematic variation distributions in all regions. First, distribu-
1078 tions are rebinned until the statistical error per bin is at least 5%. Next all local
1079 extrema are identified. The bins around smallest extrema are iteratively merged
1080 until only four local extrema remain. Then distributions are rebinned so that
1081 statistical uncertainties in each bin are < 5%.

1082 For some systematics, up and down variations may be in the same direction
1083 with respect to the nominal distributions, leading to asymmetric distributions.
1084 This causes the variations to not cover the nominal choice, and the interpretation
1085 of the confidence interval is skewed. This asymmetry may also lead to uncon-
1086 strained systematics in the fit. To handle such asymmetric systematics, if the up
1087 and down variation for a given systematic are in the same direction for at least
1088 three m_{VV} bins the variation is averaged for those bins. The averaging proce-
1089 dure replaces bin-by-bin the up and down variation bins by $b_{\pm}^{new} = b_{nom} \pm \frac{|b_+ - b_-|}{2}$,
1090 where b_{nom} is the nominal bin content and b_{\pm} are the original up and down varia-
1091 tion bin content. The same procedure is also applied to any variations where the
1092 integral of the difference between the up/down variation and the nominal distri-
1093 bution is twice that of the other down/up variation, further ensuring variations
1094 are symmetric around the nominal distribution.

1095 Finally, systematics that have a negligible effect on the m_{VV} distribution are
1096 not considered in the fit. Shape systematics where no bin in the variational dis-
1097 tribution deviates more than 1% from the nominal distribution (after normalizing
1098 all histograms to the nominal) are not included in the fit. Also, statistical bin
1099 uncertainties < 1% are ignored.

₁₁₀₀ **3.7 Fitted Systematics**

₁₁₀₁ add Ranking plots add Correlations add Asimov pulls

₁₁₀₂ **3.8 Fit Results**

₁₁₀₃ yield table background xs limits

₁₁₀₄ **3.9 Results**

₁₁₀₅ **3.9.1 Quark/Gluon Tagging**

₁₁₀₆ **Prospects**

₁₁₀₇ For the resolved analysis, signal jets are quark enriched and background jets are
₁₁₀₈ gluon dominated. By classifying jets in the event as quark or gluon initiated, less
₁₁₀₉ background would contaminate the signal region. Figure 4.1 shows the PDGID
₁₁₁₀ for the truth parton matched to the jet (meaning the highest energy parton in
₁₁₁₁ the jet catchment area) in events passing the resolved signal region selections.
₁₁₁₂ PDGID = -1 corresponds to pileup jets, $0 < \text{PDGID} < 6$ correspond to quarks
₁₁₁₃ and $\text{PDGID} = 21$ corresponds to gluons. From this Figure, it is evident that a
₁₁₁₄ notable fraction of the background that contaminates the signal region contains
₁₁₁₅ gluon jets, especially for the sub-leading jet.

₁₁₁₆ As gluons jets have more constituents and therefore more tracks (n_{trk}), the
₁₁₁₇ background jets have more tracks than the signal jets. This is shown in Figure 4.2.
₁₁₁₈ Therefore, by cutting on the number of tracks in a jet, quark and gluon jets may
₁₁₁₉ be distinguished (i.e. jets with less than a given number of tracks are classified as
₁₁₂₀ a quark, otherwise the jet is classified as a gluon.) Moreover, as the momentum
₁₁₂₁ of the jet increases the number of tracks also increases logarithmically. Therefore

1122 by applying a cut on the number of tracks that scales with the $\ln(p_T)$ is more
1123 powerful than a threshold cut on the number of tracks. Figure 4.3-Figure 4.6
1124 show normalized heat maps of $\ln(p_T)$ vs the number of reconstructed tracks for
1125 the background and a 300 GeV Z' signal. In these plots it is evident that the
1126 number of tracks in the background jets grows more quickly with $\ln(p_T)$ than for
1127 the signal jets. This is expected given that the signal is quark dominated and the
1128 background is gluon dominated.

1129 In Figure 4.8 is the ROC Curve for quark gluon tagging with cut on the
1130 number of tracks in a jet that depends on $\ln(p_T)$. The sum of the backgrounds in
1131 the signal region were used for this curve. Here the quark tagging efficiency is the
1132 ratio of quarks tagged as quarks to the total number of quarks in the signal region.
1133 The gluon rejection is calculated as the reciprocal of the gluon tagging efficiency.
1134 Choosing a 90 efficient working point with a rejection of 1.4 corresponds to a slope
1135 of 4 and intercept of -5. Focusing on the background in Figure 4.9, this cut helps
1136 minimize gluon contamination in the signal region. Also, from these heat maps it
1137 is obvious that the number of tracks in gluon jets grows more quickly than those
1138 in quark jets.

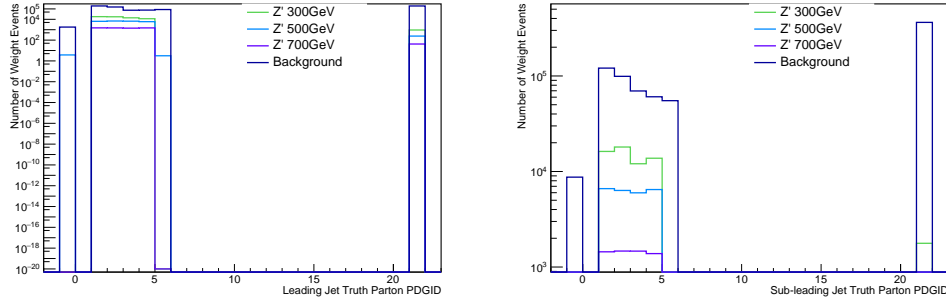


Figure 3.37: PDGID of the truth-level parton matched to the small-R jets passing the Resolved GGF WW Signal Region selections for the (a) Leading (b) Sub-Leading jets . These distributions are shown for 300, 500, and 700GeV Z' signals and the background.

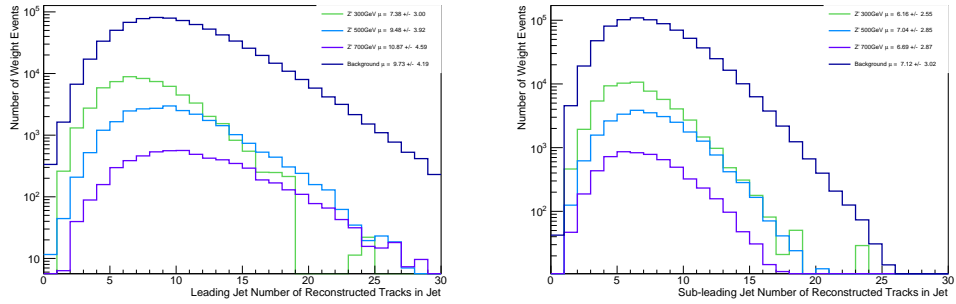


Figure 3.38: The number of tracks in small-R jets in events passing the Resolved GGF WW Signal Region selections for the (a) Leading (b) Sub-Leading jets. These distributions are shown for 300, 500, and 700GeV Z' signals and the background.

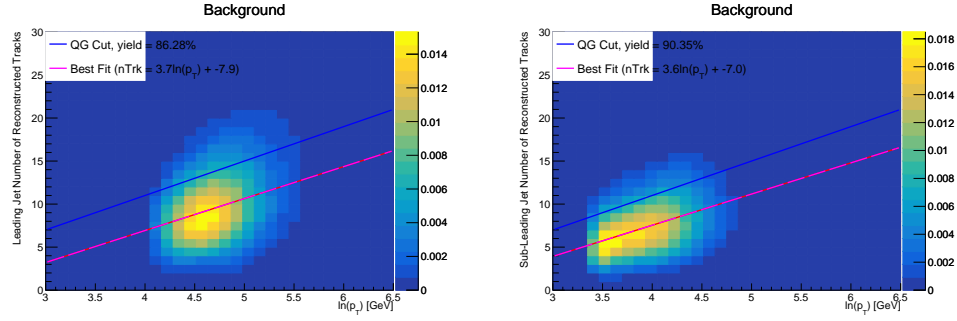


Figure 3.39: The number of tracks in background small-R jets in events passing the Resolved GGF WW Signal region selection vs. $\ln(p_T)$ for (a)Leading (b) Sub-Leading jets. The best fit line for the distribution is also shown, as well as the percentage of jets that pass a cut of number of tracks $< 4 \times \ln(p_T) - 5$. Note the number of total entries in these plots has been normalized to one.

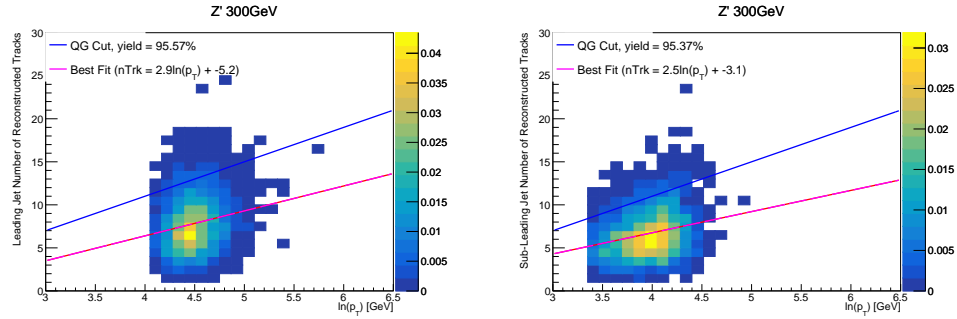


Figure 3.40: The number of tracks in small-R jets in 300GeV Z' events passing the Resolved GGF WW Signal region selection vs. $\ln(p_T)$ for (a)Leading (b) Sub-Leading jets. The best fit line for the distribution is also shown, as well as the percentage of jets that pass a cut of number of tracks $< 4 \times \ln(p_T) - 5$. Note the number of total entries in these plots has been normalized to one.

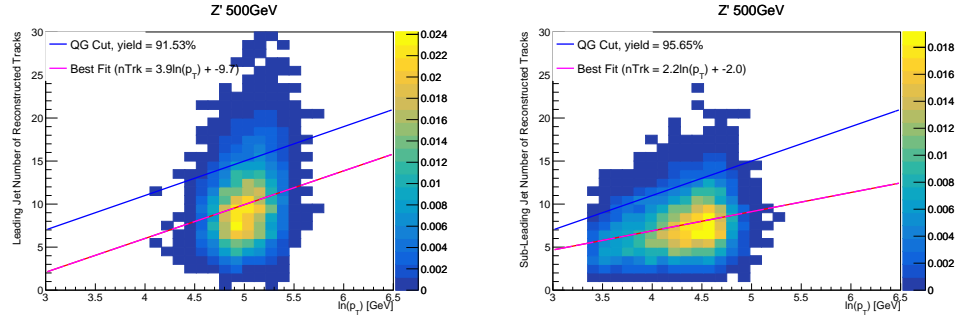


Figure 3.41: The number of tracks in small-R jets in 500GeV Z' events passing the Resolved GGF WW Signal region selection vs. $\ln(p_T)$ for (a)Leading (b) Sub-Leading jets. The best fit line for the distribution is also shown, as well as the percentage of jets that pass a cut of number of tracks $< 4 \times \ln(p_T) - 5$. Note the number of total entries in these plots has been normalized to one.

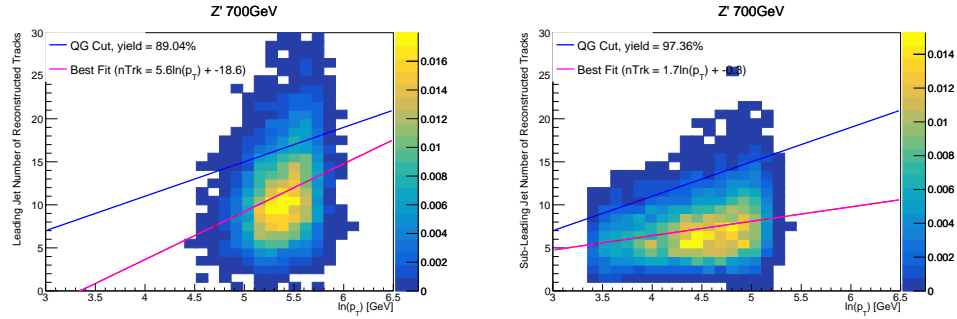


Figure 3.42: The number of tracks in small-R jets in 700GeV Z' events passing the Resolved GGF WW Signal region selection vs. $\ln(p_T)$ for (a)Leading (b) Sub-Leading jets. The best fit line for the distribution is also shown, as well as the percentage of jets that pass a cut of number of tracks $< 4 \times \ln(p_T) - 5$. Note the number of total entries in these plots has been normalized to one.

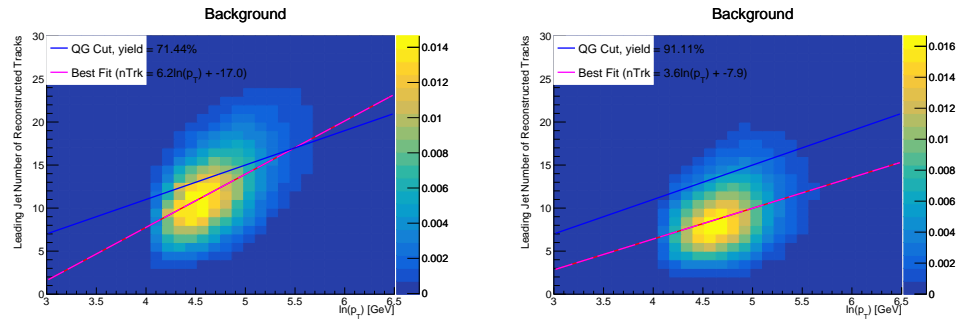


Figure 3.43: The number of tracks in leading small-R jets in background events passing the Resolved GGF WW Signal region selection vs. $\ln(p_T)$ for (a)Gluons (b) Quarks jets. The best fit line for the distribution is also shown, as well as the percentage of jets that pass a cut of number of tracks $< 4 \times \ln(p_T) - 5$.Note the number of total entries in these plots has been normalized to one.

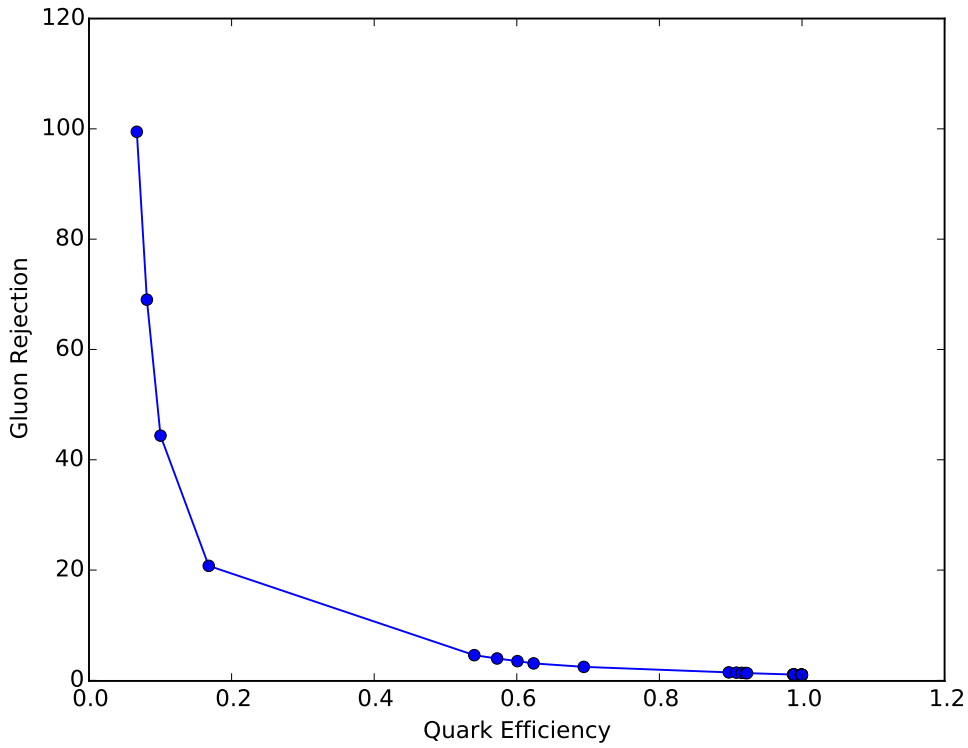


Figure 3.44: ROC Curve for Quark and Gluon Tagging with a cut on the number of tracks that depends on the $\ln(p_T)$.

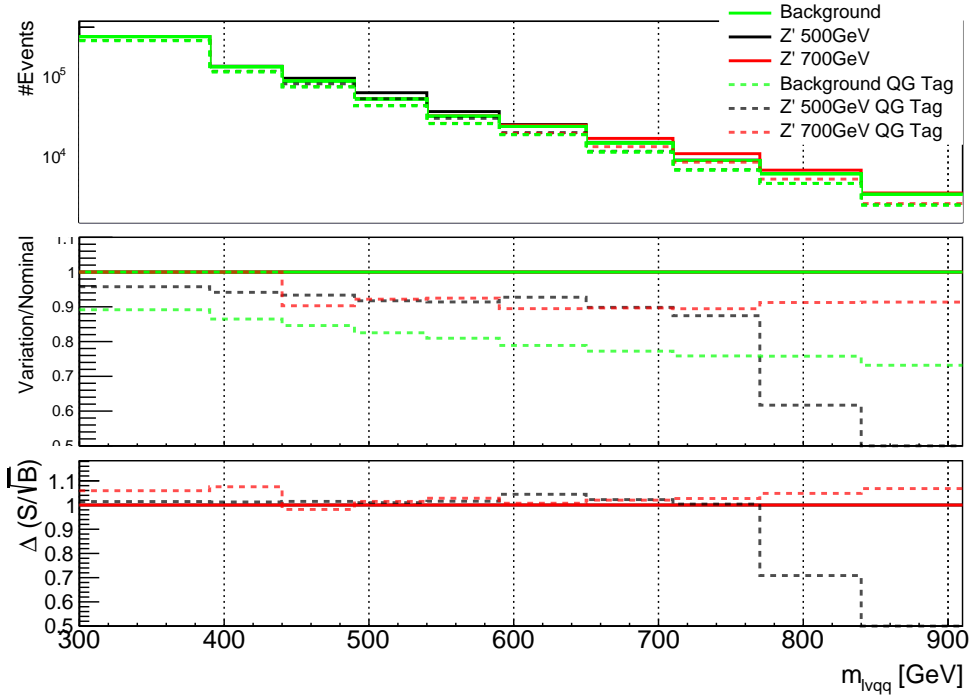


Figure 3.45: The top panel shows the distribution of m_{lvqq} with and without quark gluon tagging. The middle panel shows the ratio of the signals and backgrounds with and without quark gluon tagging. The bottom panel shows the change in S/\sqrt{B} with quark gluon tagging.

1139 n_{trk} Calibration

1140 As tagger based on nTrk cuts on the number of tracks in jets, a quantity that
 1141 is not known with infinite precision, relevant systematic uncertainties must be
 1142 evaluated. The sources of uncertainty in n_{trk} may be split into modeling and
 1143 experimental uncertainties.

1144 Modeling uncertainties are obtained by assessing PDF and ME uncertainties
 1145 on the number of charged particles in particle-level jets in dijet events. The
 1146 number of charged particles as a function of jet p_T is calculated using an Iterative
 1147 Bayesian (IB) technique [cite paper].

1148 This measurement ([7]) uses the ATLAS 2012 pp collision dataset, correspond-

1149 ing to 20.3/fb at center-of-mass energy $\sqrt{s} = 8\text{TeV}$. Monte Carlo (MC) samples
1150 are used to determine the response matrix. The MC sample is a dijet sample gen-
1151 erated with Pythia 8.175 using CT10 PDF and AU2 tune. The anti- k_T algorithm
1152 is used to cluster jets with a radius parameter $R = 0.4$. Jets are required to have
1153 $|\eta| < 2.1$. Tracks in jets are required to have $p_T > 500\text{MeV}$, $|\eta| < 2.5$, track-fit
1154 $\chi^2 < 3.0$ and originate from the primary vertex. Matching tracks to jets is accom-
1155 plished using ghost-association [cite]. In this technique, jets are re-clustered with
1156 the track collection augmented with "ghost" versions of tracks. These "ghosts"
1157 tracks have the same direction as their parent track, but infinitesimal track p_T .
1158 This insures meta-jet properties (e.g. η , p_T , etc) are unchanged. A track is
1159 matched to a jet if it's ghost version remains in the jet after re-clustering. Further
1160 details of the data, object, and event selection may be found in [cite 35].

1161 To select dijet topologies events are required to have at least two jets with
1162 $p_T > 50\text{GeV}$ that are relatively well-balanced ($p_T^{\text{lead}}/p_T^{\text{sub-lead}} < 1.5$).

1163 In the IB technique, the prior distribution and number of iterations are the
1164 inputs [cite Bayesian paper]. The IB response matrix connects number of charged
1165 particles to the number of tracks in jets determined using the simulated samples.
1166 This response matrix is used to unfold data to extract the n_c . Before applying
1167 the response matrix a fake factor is applied. This accounts for jets that pass
1168 detector level selections, but not particle level selections. Following this, the IB
1169 method iteratively applies the response matrix using the nominal Pythia 8.175
1170 sample as a prior. The number of IB iterations is chosen to minimize unfolding
1171 bias and statistical fluctuations. For this measurement four iterations was found
1172 to be optimal by minimizing the unfolding bias from pseudodata simulated with
1173 Herwig++ with a prior from Pythia 8 AU2. Finally, the inefficiency factor is
1174 applied to account for events passing particle level selection but not detector

1175 level, yielding the unfolded nCharged distribution.

1176 This process is prone to three main sources of bias: response matrix, correction
1177 factor, and unfolding procedure uncertainties. The response matrix is sensitive to
1178 experimental uncertainties impacting jet track reconstruction and calorimeter jet
1179 p_T . Correction factors are also sensitive to experimental uncertainties (e.g. JES)
1180 as such uncertainties modify detector level acceptance. Sensitivity to particle level
1181 acceptance is calculated by comparing Pythia and Herwig. Finally, the bias from
1182 the IB prior choice is determined by reweighting the particle-level spectrum, so
1183 the simulated detector level spectrum more closely matches the uncorrected data.
1184 Unfolding this modified detector-level simulation and comparing it re-weighted
1185 particle-level spectrum indicates bias from the prior distribution choice.

1186 A summary of all the systematic uncertainties associated with this unfolding
1187 may be found in [ref paper]. Total uncertainties are < 7% for the number of
1188 charged particles in jets. The unfolded distribution of the nCharged in jets from
1189 data are further analyzed to extract the quark and gluon nCharged distributions.
1190 In dijet events, the jet with a larger η is more energetic and therefore more likely
1191 to be a quark. This is due to the quarks in protons generally having a larger
1192 fraction of the total momentum of the proton constituents. The more central jet
1193 is more likely to be a gluon-initiated jet. This correlation between jet η and flavor
1194 may then be used to extract nCharged in p_T bins using:

$$\langle n_c^f \rangle = f_q^f \langle n_c^q \rangle + f_g^f \langle n_c^g \rangle \quad (3.13)$$

1195

$$\langle n_c^c \rangle = f_q^c \langle n_c^q \rangle + f_g^c \langle n_c^g \rangle \quad (3.14)$$

1196 In this equation the f and c subscripts denote the more forward and central
1197 jets, respectively. The q and g subscripts denote quark and gluon. The fraction
1198 of more forward jets that are say gluons is denoted by f_g^f . The other relevant jet

1199 fractions are denoted with the same naming scheme. Finally, $\langle n_c \rangle$ is the average
 1200 number of charged particles in a jet in a given p_T bin. To show that Eq. (??) may
 1201 be used to extract quark and gluon n_c distributions the extracted distributions
 1202 are compared to n_c distributions determined using the jet flavor in simulation.
 1203 Figure [add figure natasha] shows that the extracted and true distributions differ
 1204 by $< 1\%$ over the p_T ranged probed for this study. Moreover, this implies that n_c
 1205 depends only on the flavor of the initiating parton and jet p_T .

1206 These extracted distributions are prone to PDF and ME biases. The bias from
 1207 the choice of the CT10 PDF for the Pythia sample is accounted for by comparing
 1208 quark/gluon fractions for the nominal CT10 sample with its eigenvector variations.
 1209 Comparing the quark/gluon fractions from Pythia 8 and Herwig++ quantify the
 1210 uncertainty from the ME calculation. These uncertainties are added in quadra-
 1211 ture with the unfolding uncertainty to give the total modelling uncertainty on
 1212 the extracted n_c distribution. This is shown in Figure 4.11.

1213 To apply these uncertainties in n_c distributions in data, per-jet event weights
 1214 are associated with each uncertainty according to:

$$w_i(n_c) = \frac{P(n_c | \langle n_c \rangle \pm \sigma_{n_c}^i)}{P(n_c | \langle n_c \rangle)} \quad (3.15)$$

1215 In Eq. (??), i denotes the uncertainty considered, P is the Poisson probability,
 1216 and $\sigma_{n_c}^i$ represents the average impact of the uncertainty on n_c .

1217 The previous uncertainties described accounted for modeling uncertainty as-
 1218 sociated with the number of charged particles in a jet. However, n_c is not a
 1219 measurable quantity. Instead the number of tracks in a jet is measured, which is
 1220 a proxy for n_c . Therefore the uncertainties associated with the measurement of
 1221 nTracks must also be considered ([9]). These uncertainties were calculated using
 1222 a Pythia 8 dijet sample with NNPDF 23. Track reconstruction efficiency and fake

1223 rates are the dominant sources of nTrack uncertainties.

1224 The track reconstruction efficiency is effected by the uncertainty of the de-
1225 scription of the ID material in simulation and the modeling of charged-particle
1226 interactions with this material. These uncertainties are accounted for by varying
1227 the ID material by 5-25% (dependent on the region of the detector considered).
1228 The difference in the tracking efficiency between the nominal and varied simula-
1229 tion give the uncertainty on the track reconstruction efficiency. Another important
1230 source of track reconstruction efficiency arises in the core of jets. The high density
1231 of tracks in the jet cores can cause ID clusters to merge. The fraction of lost tracks
1232 due to merging is given by the fraction of tracks that have a charge of two mini-
1233 mum ionizing particles. This quantity is compared between data and simulation
1234 resulting in an uncertainty of 0.4% on tracks with $\Delta R < 0.1$. Combining these
1235 effects gives a total uncertainty as a function of p_T and η that is generally $< 2\%$
1236 [references figure 44 from [9]].

1237 Fake tracks are the other dominant source of nTrk uncertainty. Fake tracks
1238 are tracks that cannot be associated to a single particle. Often these tracks are a
1239 result of random combinations of hits from charged particles that overlap in space.
1240 In dense environments, such as the core of jets or high-pileup environments, fake
1241 tracks are more likely. Fake tracks are estimated with a 'control region method'
1242 which is briefly summarized here [[8]]. By applying a series of track selections
1243 to enrich the fraction of fake tracks (e.g. $|d_0| > 0.1$, track $\chi^2 > 1.4$, etc) in
1244 simulation, templates for fake track parameters are calculated. These templates
1245 are then fit to data to determine the fraction of fake tracks. On average the fake
1246 rate is found to be 30% (independent of p_T and η).

1247 To assess the impact of these two detector level uncertainties, tracks are ran-
1248 domly dropped according to the rates described above. Reconstruction and fake

1249 uncertainties both lower the number of tracks, hence these uncertainties are one-
 1250 sided. By dropping tracks in this way a varied nTrk distribution is calculated for
 1251 both uncertainties. The associated per-jet event weights are then calculated in
 1252 the same way as the modeling weights as:

$$w_i(n_c) = \frac{P(n_{trk} | < n_{trk} > \pm \sigma_{n_{trk}}^i)}{P(n_{trk} | < n_{trk} >)} \quad (3.16)$$

1253 Adding the modeling and detector level uncertainties in quadrature gives the
 1254 overall nTrack uncertainty. The effects of the individual uncertainties on the nTrk
 1255 distributions can be seen in Fig 4.13. Fig 4.12 shows the m_{lvqq} and nTrk distri-
 1256 butions for the W and Top control regions before likelihood fitting. In these plots
 1257 the nTrk uncertainties improve agreement between data and MC. The remaining
 1258 differences are likely covered by likelihood fitting and improving the analysis itself.

1259 Application

1260 Using the 90% WP of the n_{trk} tagger improves S/\sqrt{B} is $< 3\%$ as shown in
 1261 Figure 4.9. Although, n_{trk} is the single most powerful discriminating variable
 1262 for quark and gluon jets, the addition of other jet variables would improve the
 1263 classification efficiency. Figure 4.10 shows the possible improvement of 10%
 1264 in jet classification using the truth label of the jets to classify jets. This type of
 1265 improvement is possible by using variables such as jet width, and energy correlata-
 1266 tors. Figure [add BDT figure/use 1612.01551.pdf] shows for a 90% quark tagging
 1267 efficiency for a 100 GeV jet, a BDT improve the gluon rejection by 0.4. Once this
 1268 tagger is calibrated it would improve the analysis sensitivity of this channel.

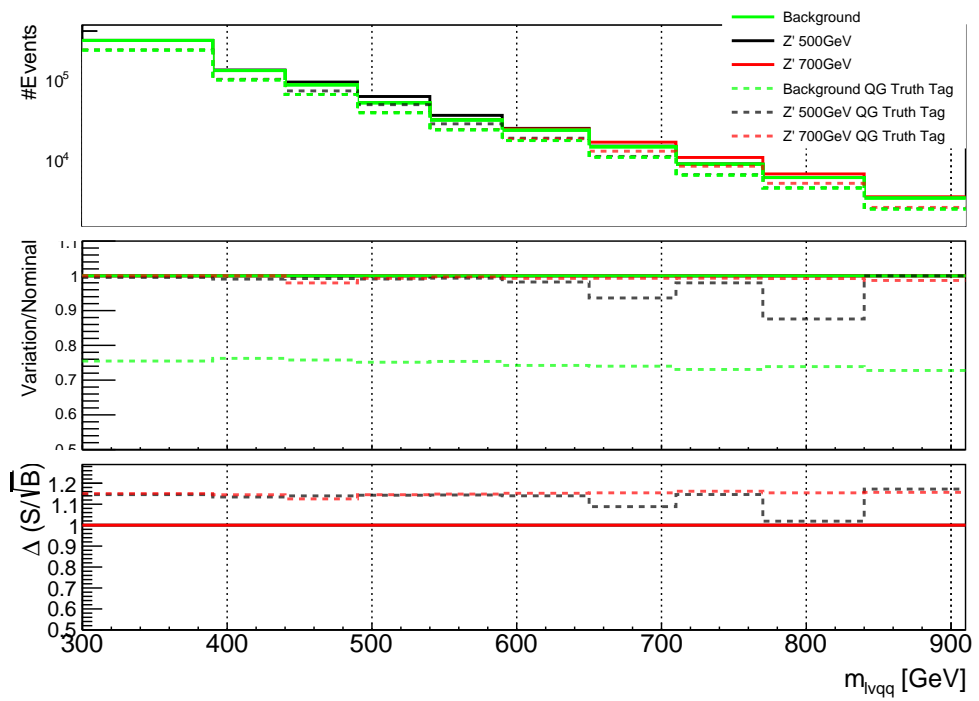


Figure 3.46: The top panel shows the distribution of m_{lvqq} with and without requiring jets to be true quarks. The middle panel shows the ratio of the signals and backgrounds with and without requiring jets to be true quarks. The bottom panel shows the change in S/\sqrt{B} when requiring jets to be true quarks..

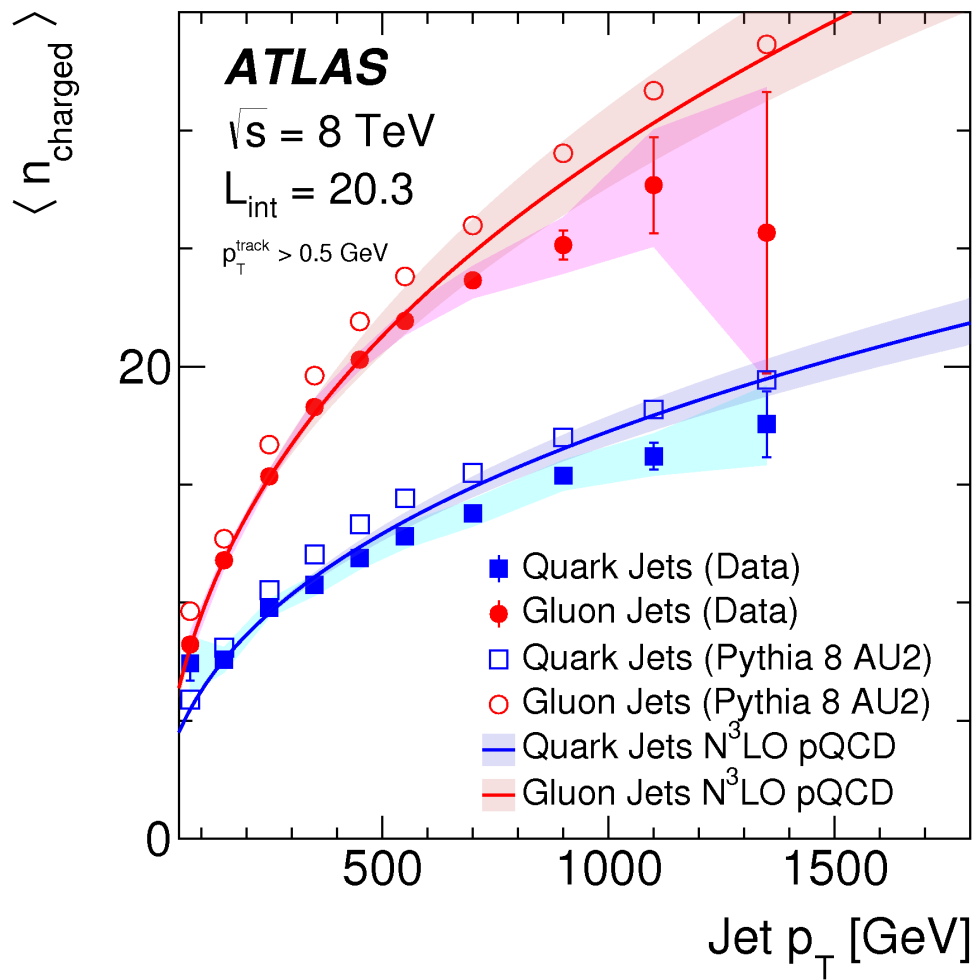


Figure 3.47: Unfolded and extracted n_C qg dstbs..

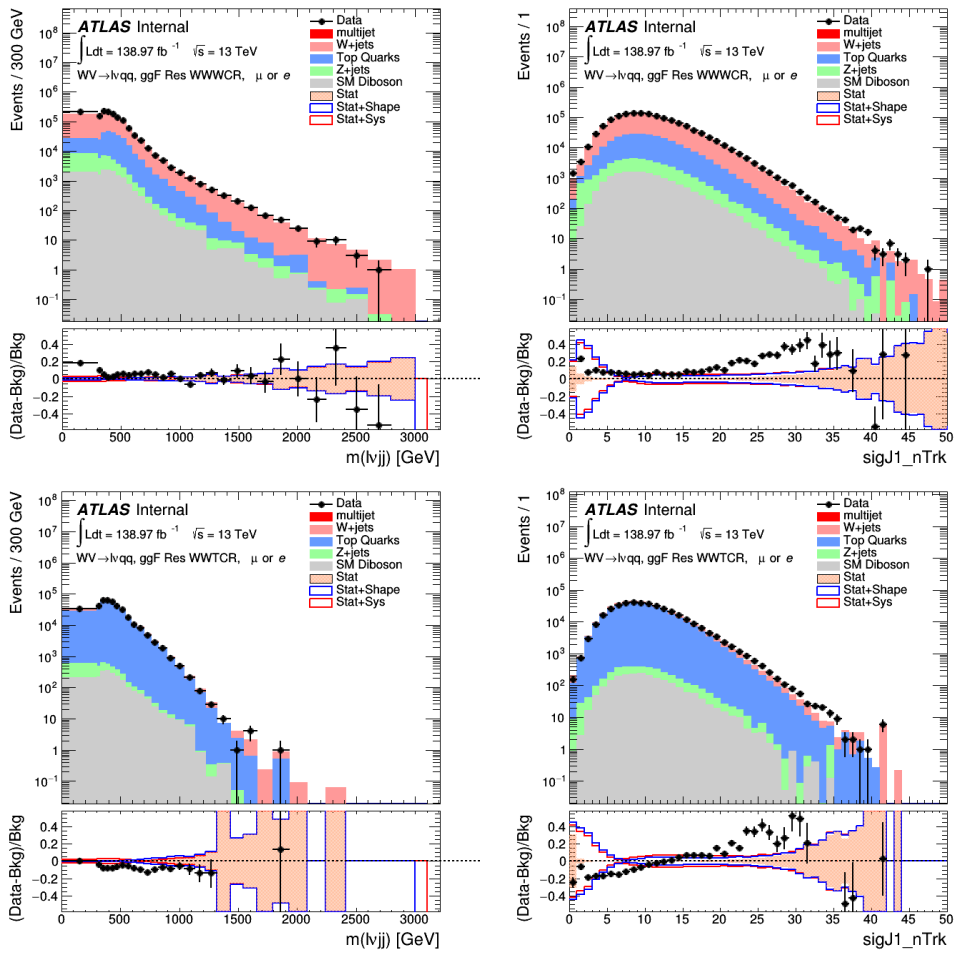


Figure 3.48: PDGID of the truth-level parton matched to the small-R jets passing the Resolved GGF WW Signal Region selections for the (a) Leading (b) Sub-Leading jets . These distributions are shown for 300, 500, and 700GeV Z' signals and the background.

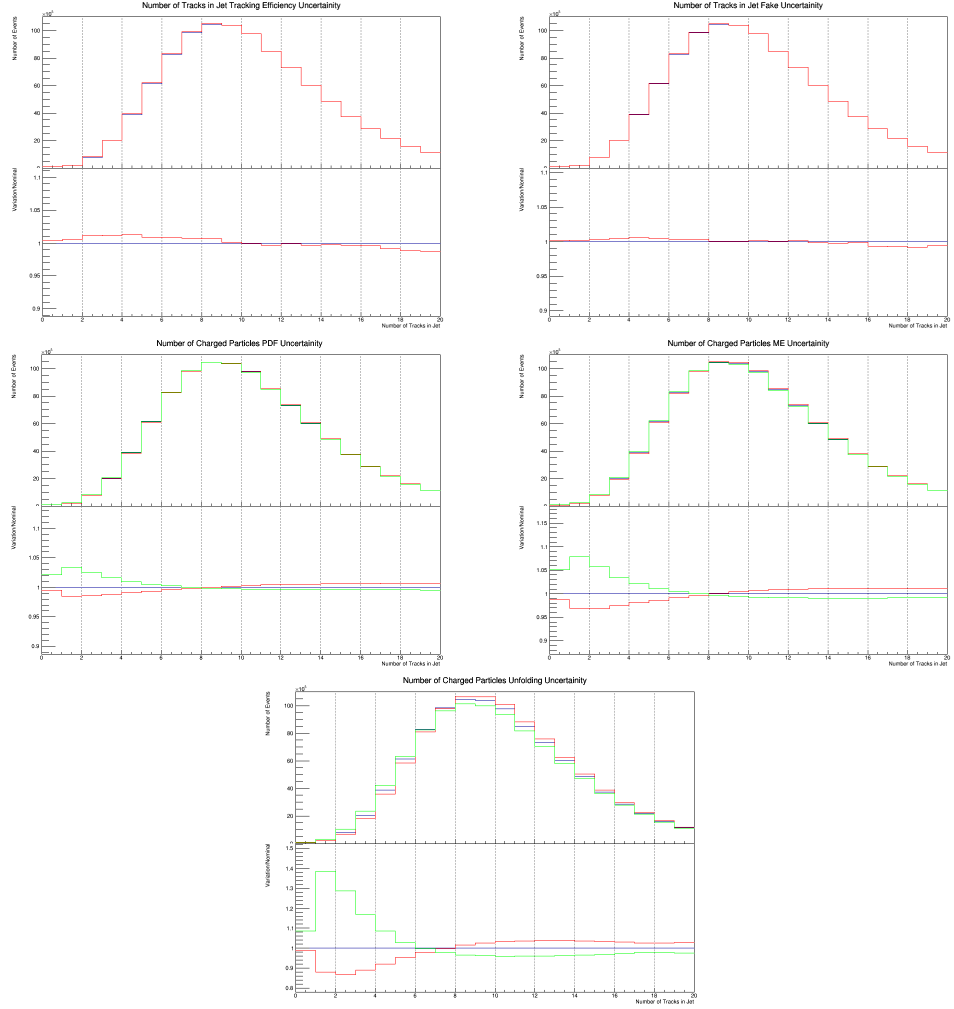


Figure 3.49: These figures show the impact of the uncertainties on the number of tracks in the leading jet in the sum of the background sample in the Resolved GGF WW SR (a) tracking efficiency (b) fake (c) PDF (d) ME (e) unfolding uncertainties.

₁₂₆₉ **Chapter 4**

₁₂₇₀ **Quark and Gluon Tagging**

₁₂₇₁ **4.1 Prospects**

₁₂₇₂ For the resolved analysis, signal jets are quark enriched and background jets are
₁₂₇₃ gluon dominated. By classifying jets in the event as quark or gluon initiated, less
₁₂₇₄ background would contaminate the signal region. Figure 4.1 shows the PDGID
₁₂₇₅ for the truth parton matched to the jet (meaning the highest energy parton in
₁₂₇₆ the jet catchment area) in events passing the resolved signal region selections.
₁₂₇₇ PDGID = -1 corresponds to pileup jets, $0 < \text{PDGID} < 6$ correspond to quarks
₁₂₇₈ and $\text{PDGID} = 21$ corresponds to gluons. From this Figure, it is evident that a
₁₂₇₉ notable fraction of the background that contaminates the signal region contains
₁₂₈₀ gluon jets, especially for the sub-leading jet.

₁₂₈₁ As gluons jets have more constituents and therefore more tracks (n_{trk}), the
₁₂₈₂ background jets have more tracks than the signal jets. This is shown in Figure 4.2.
₁₂₈₃ Therefore, by cutting on the number of tracks in a jet, quark and gluon jets may
₁₂₈₄ be distinguished (i.e. jets with less than a given number of tracks are classified as
₁₂₈₅ a quark, otherwise the jet is classified as a gluon.) Moreover, as the momentum
₁₂₈₆ of the jet increases the number of tracks also increases logarithmically. Therefore

1287 by applying a cut on the number of tracks that scales with the $\ln(p_T)$ is more
1288 powerful than a threshold cut on the number of tracks. Figure 4.3-Figure 4.6
1289 show normalized heat maps of $\ln(p_T)$ vs the number of reconstructed tracks for
1290 the background and a 300 GeV Z' signal. In these plots it is evident that the
1291 number of tracks in the background jets grows more quickly with $\ln(p_T)$ than for
1292 the signal jets. This is expected given that the signal is quark dominated and the
1293 background is gluon dominated.

1294 In Figure 4.8 is the ROC Curve for quark gluon tagging with cut on the
1295 number of tracks in a jet that depends on $\ln(p_T)$. The sum of the backgrounds in
1296 the signal region were used for this curve. Here the quark tagging efficiency is the
1297 ratio of quarks tagged as quarks to the total number of quarks in the signal region.
1298 The gluon rejection is calculated as the reciprocal of the gluon tagging efficiency.
1299 Choosing a 90 efficient working point with a rejection of 1.4 corresponds to a slope
1300 of 4 and intercept of -5. Focusing on the background in Figure 4.9, this cut helps
1301 minimize gluon contamination in the signal region. Also, from these heat maps it
1302 is obvious that the number of tracks in gluon jets grows more quickly than those
1303 in quark jets.

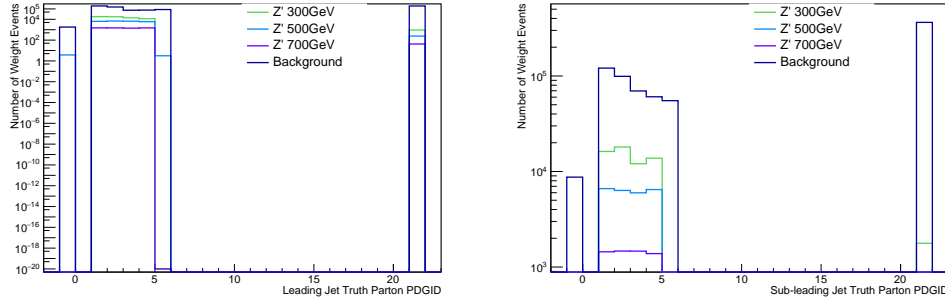


Figure 4.1: PDGID of the truth-level parton matched to the small-R jets passing the Resolved GGF WW Signal Region selections for the (a) Leading (b) Sub-Leading jets . These distributions are shown for 300, 500, and 700GeV Z' signals and the background.

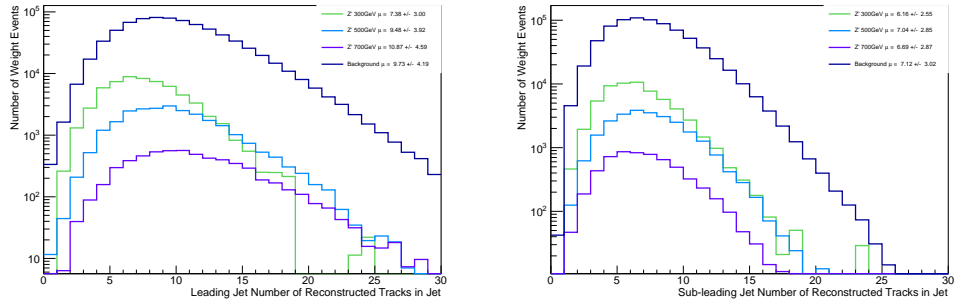


Figure 4.2: The number of tracks in small-R jets in events passing the Resolved GGF WW Signal Region selections for the (a) Leading (b) Sub-Leading jets. These distributions are shown for 300, 500, and 700GeV Z' signals and the background.

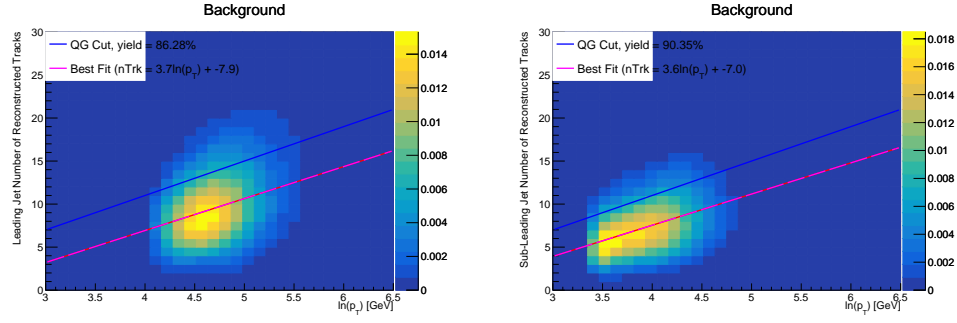


Figure 4.3: The number of tracks in background small-R jets in events passing the Resolved GGF WW Signal region selection vs. $\ln(p_T)$ for (a)Leading (b) Sub-Leading jets. The best fit line for the distribution is also shown, as well as the percentage of jets that pass a cut of number of tracks $< 4 \times \ln(p_T) - 5$. Note the number of total entries in these plots has been normalized to one.

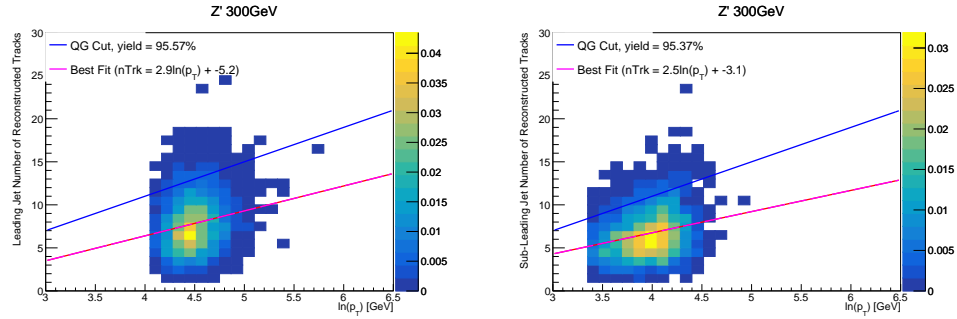


Figure 4.4: The number of tracks in small-R jets in 300GeV Z' events passing the Resolved GGF WW Signal region selection vs. $\ln(p_T)$ for (a)Leading (b) Sub-Leading jets. The best fit line for the distribution is also shown, as well as the percentage of jets that pass a cut of number of tracks $< 4 \times \ln(p_T) - 5$. Note the number of total entries in these plots has been normalized to one.

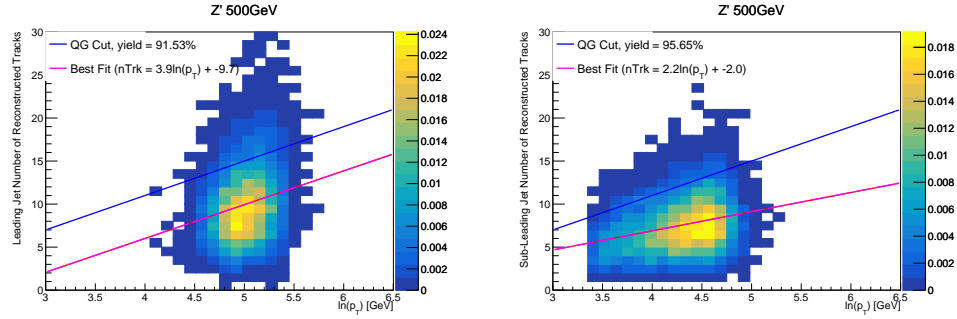


Figure 4.5: The number of tracks in small-R jets in 500GeV Z' events passing the Resolved GGF WW Signal region selection vs. $\ln(p_T)$ for (a)Leading (b) Sub-Leading jets. The best fit line for the distribution is also shown, as well as the percentage of jets that pass a cut of number of tracks $< 4 \times \ln(p_T) - 5$. Note the number of total entries in these plots has been normalized to one.

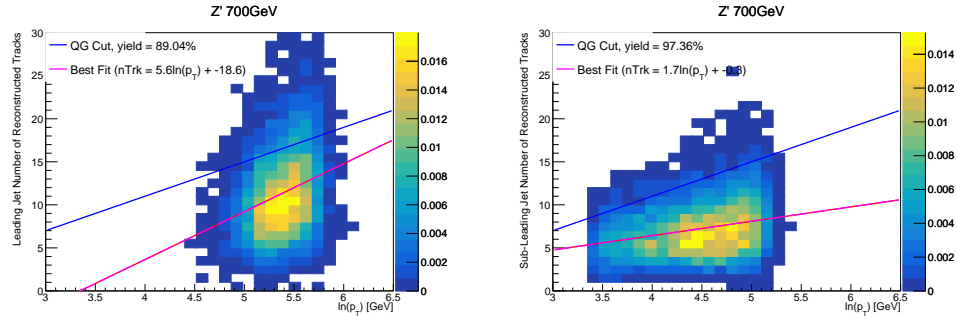


Figure 4.6: The number of tracks in small-R jets in 700GeV Z' events passing the Resolved GGF WW Signal region selection vs. $\ln(p_T)$ for (a)Leading (b) Sub-Leading jets. The best fit line for the distribution is also shown, as well as the percentage of jets that pass a cut of number of tracks $< 4 \times \ln(p_T) - 5$. Note the number of total entries in these plots has been normalized to one.

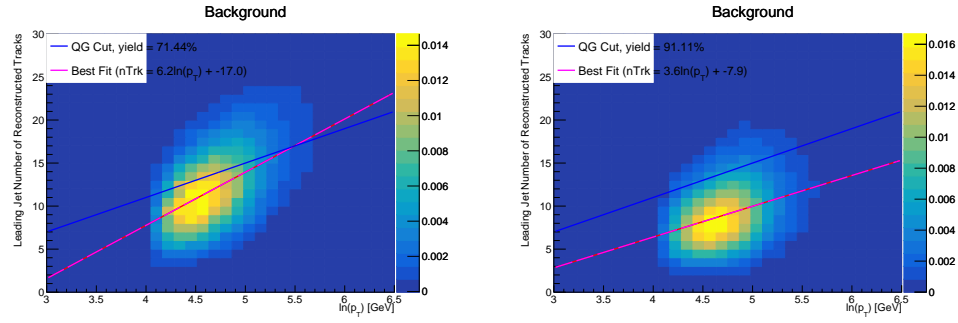


Figure 4.7: The number of tracks in leading small-R jets in background events passing the Resolved GGF WW Signal region selection vs. $\ln(p_T)$ for (a)Gluons (b) Quarks jets. The best fit line for the distribution is also shown, as well as the percentage of jets that pass a cut of number of tracks $< 4 \times \ln(p_T) - 5$.Note the number of total entries in these plots has been normalized to one.

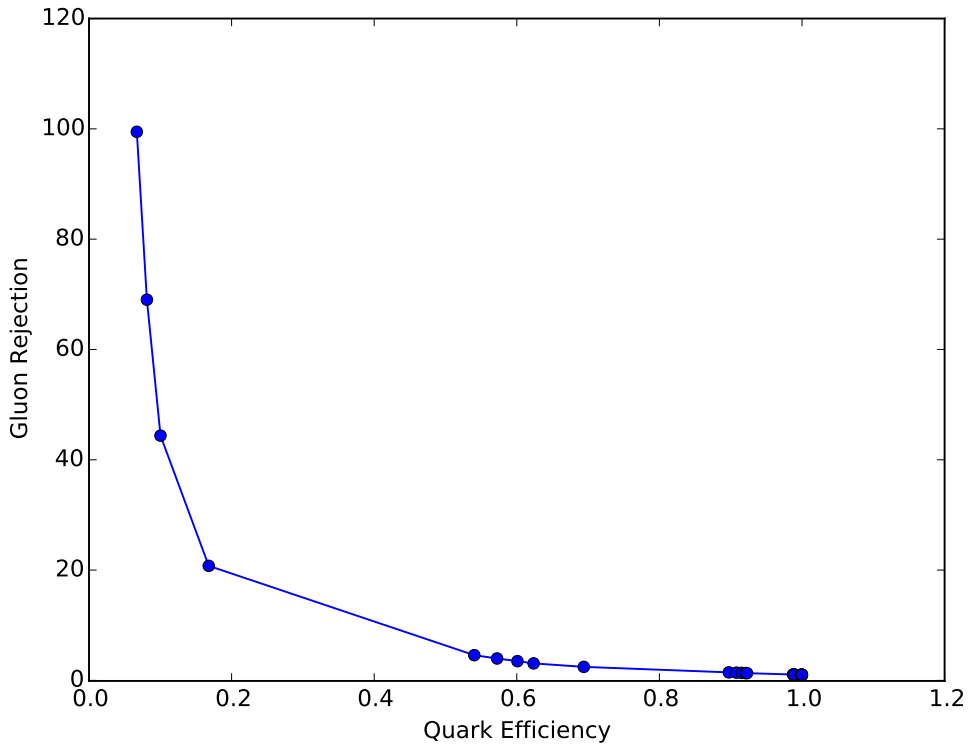


Figure 4.8: ROC Curve for Quark and Gluon Tagging with a cut on the number of tracks that depends on the $\ln(p_T)$.

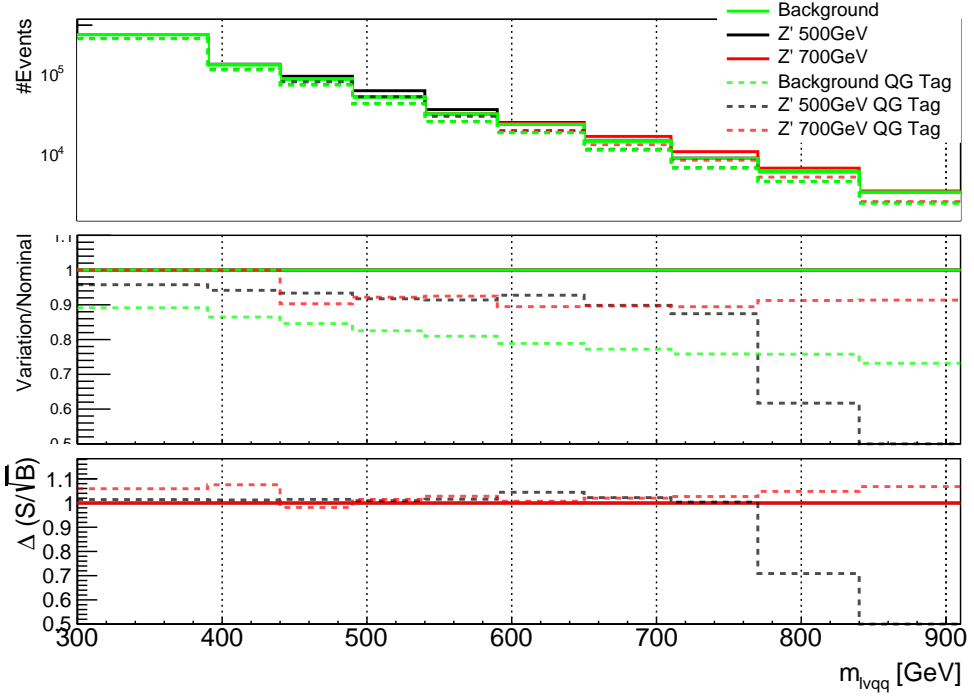


Figure 4.9: The top panel shows the distribution of m_{lvqq} with and without quark gluon tagging. The middle panel shows the ratio of the signals and backgrounds with and without quark gluon tagging. The bottom panel shows the change in S/\sqrt{B} with quark gluon tagging.

1304 4.2 n_{trk} Calibration

1305 As tagger based on nTrk cuts on the number of tracks in jets, a quantity that
 1306 is not known with infinite precision, relevant systematic uncertainties must be
 1307 evaluated. The sources of uncertainty in n_{trk} may be split into modeling and
 1308 experimental uncertainties.

1309 Modeling uncertainties are obtained by assessing PDF and ME uncertainties
 1310 on the number of charged particles in particle-level jets in dijet events. The
 1311 number of charged particles as a function of jet p_T is calculated using an Iterative
 1312 Bayesian (IB) technique [cite paper].

1313 This measurement ([7]) uses the ATLAS 2012 pp collision dataset, correspond-

ing to 20.3/fb at center-of-mass energy $\sqrt{s} = 8\text{TeV}$. Monte Carlo (MC) samples are used to determine the response matrix. The MC sample is a dijet sample generated with Pythia 8.175 using CT10 PDF and AU2 tune. The anti- k_T algorithm is used to cluster jets with a radius parameter $R = 0.4$. Jets are required to have $|\eta| < 2.1$. Tracks in jets are required to have $p_T > 500\text{MeV}$, $|\eta| < 2.5$, track-fit $\chi^2 < 3.0$ and originate from the primary vertex. Matching tracks to jets is accomplished using ghost-association [cite]. In this technique, jets are re-clustered with the track collection augmented with "ghost" versions of tracks. These "ghosts" tracks have the same direction as their parent track, but infinitesimal track p_T . This insures meta-jet properties (e.g. η , p_T , etc) are unchanged. A track is matched to a jet if it's ghost version remains in the jet after re-clustering. Further details of the data, object, and event selection may be found in [cite 35].

To select dijet topologies events are required to have at least two jets with $p_T > 50\text{GeV}$ that are relatively well-balanced ($p_T^{lead}/p_T^{sub-lead} < 1.5$).

In the IB technique, the prior distribution and number of iterations are the inputs [cite Bayesian paper]. The IB response matrix connects number of charged particles to the number of tracks in jets determined using the simulated samples. This response matrix is used to unfold data to extract the n_c . Before applying the response matrix a fake factor is applied. This accounts for jets that pass detector level selections, but not particle level selections. Following this, the IB method iteratively applies the response matrix using the nominal Pythia 8.175 sample as a prior. The number of IB iterations is chosen to minimize unfolding bias and statistical fluctuations. For this measurement four iterations was found to be optimal by minimizing the unfolding bias from pseudodata simulated with Herwig++ with a prior from Pythia 8 AU2. Finally, the inefficiency factor is applied to account for events passing particle level selection but not detector

1340 level, yielding the unfolded nCharged distribution.

1341 This process is prone to three main sources of bias: response matrix, correction
1342 factor, and unfolding procedure uncertainties. The response matrix is sensitive to
1343 experimental uncertainties impacting jet track reconstruction and calorimeter jet
1344 p_T . Correction factors are also sensitive to experimental uncertainties (e.g. JES)
1345 as such uncertainties modify detector level acceptance. Sensitivity to particle level
1346 acceptance is calculated by comparing Pythia and Herwig. Finally, the bias from
1347 the IB prior choice is determined by reweighting the particle-level spectrum, so
1348 the simulated detector level spectrum more closely matches the uncorrected data.
1349 Unfolding this modified detector-level simulation and comparing it re-weighted
1350 particle-level spectrum indicates bias from the prior distribution choice.

1351 A summary of all the systematic uncertainties associated with this unfolding
1352 may be found in [ref paper]. Total uncertainties are < 7% for the number of
1353 charged particles in jets. The unfolded distribution of the nCharged in jets from
1354 data are further analyzed to extract the quark and gluon nCharged distributions.
1355 In dijet events, the jet with a larger η is more energetic and therefore more likely
1356 to be a quark. This is due to the quarks in protons generally having a larger
1357 fraction of the total momentum of the proton constituents. The more central jet
1358 is more likely to be a gluon-initiated jet. This correlation between jet η and flavor
1359 may then be used to extract nCharged in p_T bins using:

$$\langle n_c^f \rangle = f_q^f \langle n_c^q \rangle + f_g^f \langle n_c^g \rangle \quad (4.1)$$

1360

$$\langle n_c^c \rangle = f_q^c \langle n_c^q \rangle + f_g^c \langle n_c^g \rangle \quad (4.2)$$

1361 In this equation the f and c subscripts denote the more forward and central
1362 jets, respectively. The q and g subscripts denote quark and gluon. The fraction
1363 of more forward jets that are say gluons is denoted by f_g^f . The other relevant jet

1364 fractions are denoted with the same naming scheme. Finally, $\langle n_c \rangle$ is the average
 1365 number of charged particles in a jet in a given p_T bin. To show that Eq. (??) may
 1366 be used to extract quark and gluon n_c distributions the extracted distributions
 1367 are compared to n_c distributions determined using the jet flavor in simulation.
 1368 Figure [add figure natasha] shows that the extracted and true distributions differ
 1369 by $< 1\%$ over the p_T ranged probed for this study. Moreover, this implies that n_c
 1370 depends only on the flavor of the initiating parton and jet p_T .

1371 These extracted distributions are prone to PDF and ME biases. The bias from
 1372 the choice of the CT10 PDF for the Pythia sample is accounted for by comparing
 1373 quark/gluon fractions for the nominal CT10 sample with its eigenvector variations.
 1374 Comparing the quark/gluon fractions from Pythia 8 and Herwig++ quantify the
 1375 uncertainty from the ME calculation. These uncertainties are added in quadra-
 1376 ture with the unfolding uncertainty to give the total modelling uncertainty on
 1377 the extracted n_c distribution. This is shown in Figure 4.11.

1378 To apply these uncertainties in n_c distributions in data, per-jet event weights
 1379 are associated with each uncertainty according to:

$$w_i(n_c) = \frac{P(n_c | \langle n_c \rangle \pm \sigma_{n_c}^i)}{P(n_c | \langle n_c \rangle)} \quad (4.3)$$

1380 In Eq. (??), i denotes the uncertainty considered, P is the Poisson probability,
 1381 and $\sigma_{n_c}^i$ represents the average impact of the uncertainty on n_c .

1382 The previous uncertainties described accounted for modeling uncertainty as-
 1383 sociated with the number of charged particles in a jet. However, n_c is not a
 1384 measurable quantity. Instead the number of tracks in a jet is measured, which is
 1385 a proxy for n_c . Therefore the uncertainties associated with the measurement of
 1386 nTracks must also be considered ([9]). These uncertainties were calculated using
 1387 a Pythia 8 dijet sample with NNPDF 23. Track reconstruction efficiency and fake

1388 rates are the dominant sources of nTrack uncertainties.

1389 The track reconstruction efficiency is effected by the uncertainty of the de-
1390 scription of the ID material in simulation and the modeling of charged-particle
1391 interactions with this material. These uncertainties are accounted for by varying
1392 the ID material by 5-25% (dependent on the region of the detector considered).
1393 The difference in the tracking efficiency between the nominal and varied simula-
1394 tion give the uncertainty on the track reconstruction efficiency. Another important
1395 source of track reconstruction efficiency arises in the core of jets. The high density
1396 of tracks in the jet cores can cause ID clusters to merge. The fraction of lost tracks
1397 due to merging is given by the fraction of tracks that have a charge of two mini-
1398 mum ionizing particles. This quantity is compared between data and simulation
1399 resulting in an uncertainty of 0.4% on tracks with $\Delta R < 0.1$. Combining these
1400 effects gives a total uncertainty as a function of p_T and η that is generally $< 2\%$
1401 [references figure 44 from [9]].

1402 Fake tracks are the other dominant source of nTrk uncertainty. Fake tracks
1403 are tracks that cannot be associated to a single particle. Often these tracks are a
1404 result of random combinations of hits from charged particles that overlap in space.
1405 In dense environments, such as the core of jets or high-pileup environments, fake
1406 tracks are more likely. Fake tracks are estimated with a 'control region method'
1407 which is briefly summarized here [[8]]. By applying a series of track selections
1408 to enrich the fraction of fake tracks (e.g. $|d_0| > 0.1$, track $\chi^2 > 1.4$, etc) in
1409 simulation, templates for fake track parameters are calculated. These templates
1410 are then fit to data to determine the fraction of fake tracks. On average the fake
1411 rate is found to be 30% (independent of p_T and η).

1412 To assess the impact of these two detector level uncertainties, tracks are ran-
1413 domly dropped according to the rates described above. Reconstruction and fake

1414 uncertainties both lower the number of tracks, hence these uncertainties are one-
1415 sided. By dropping tracks in this way a varied nTrk distribution is calculated for
1416 both uncertainties. The associated per-jet event weights are then calculated in
1417 the same way as the modeling weights as:

$$w_i(n_c) = \frac{P(n_{trk} | < n_{trk} > \pm \sigma_{n_{trk}}^i)}{P(n_{trk} | < n_{trk} >)} \quad (4.4)$$

1418 Adding the modeling and detector level uncertainties in quadrature gives the
1419 overall nTrack uncertainty. The effects of the individual uncertainties on the nTrk
1420 distributions can be seen in Fig 4.13. Fig 4.12 shows the m_{lvqq} and nTrk distri-
1421 butions for the W and Top control regions before likelihood fitting. In these plots
1422 the nTrk uncertainties improve agreement between data and MC. The remaining
1423 differences are likely covered by likelihood fitting and improving the analysis itself.

1424 4.3 Application

1425 Using the 90% WP of the n_{trk} tagger improves S/\sqrt{B} is $< 3\%$ as shown in
1426 Figure 4.9. Although, n_{trk} is the single most powerful discriminating variable
1427 for quark and gluon jets, the addition of other jet variables would improve the
1428 classification efficiency. Figure 4.10 shows the possible improvement of 10%
1429 in jet classification using the truth label of the jets to classify jets. This type of
1430 improvement is possible by using variables such as jet width, and energy correlata-
1431 tors. Figure [add BDT figure/use 1612.01551.pdf] shows for a 90% quark tagging
1432 efficiency for a 100 GeV jet, a BDT improve the gluon rejection by 0.4. Once this
1433 tagger is calibrated it would improve the analysis sensitivity of this channel.

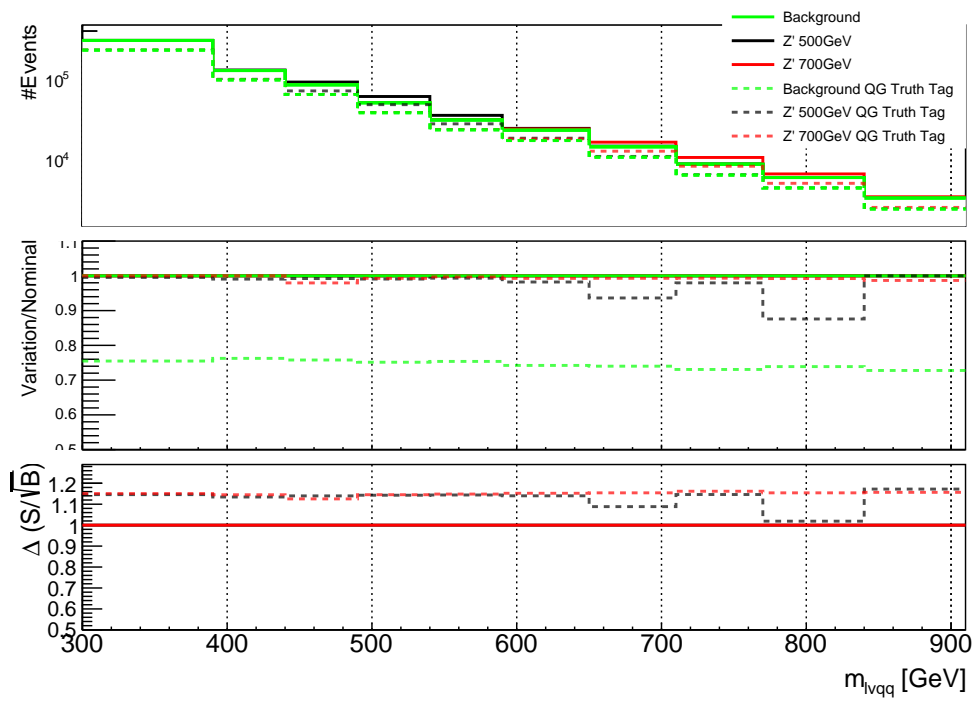


Figure 4.10: The top panel shows the distribution of m_{lvqq} with and without requiring jets to be true quarks. The middle panel shows the ratio of the signals and backgrounds with and without requiring jets to be true quarks. The bottom panel shows the change in S/\sqrt{B} when requiring jets to be true quarks..

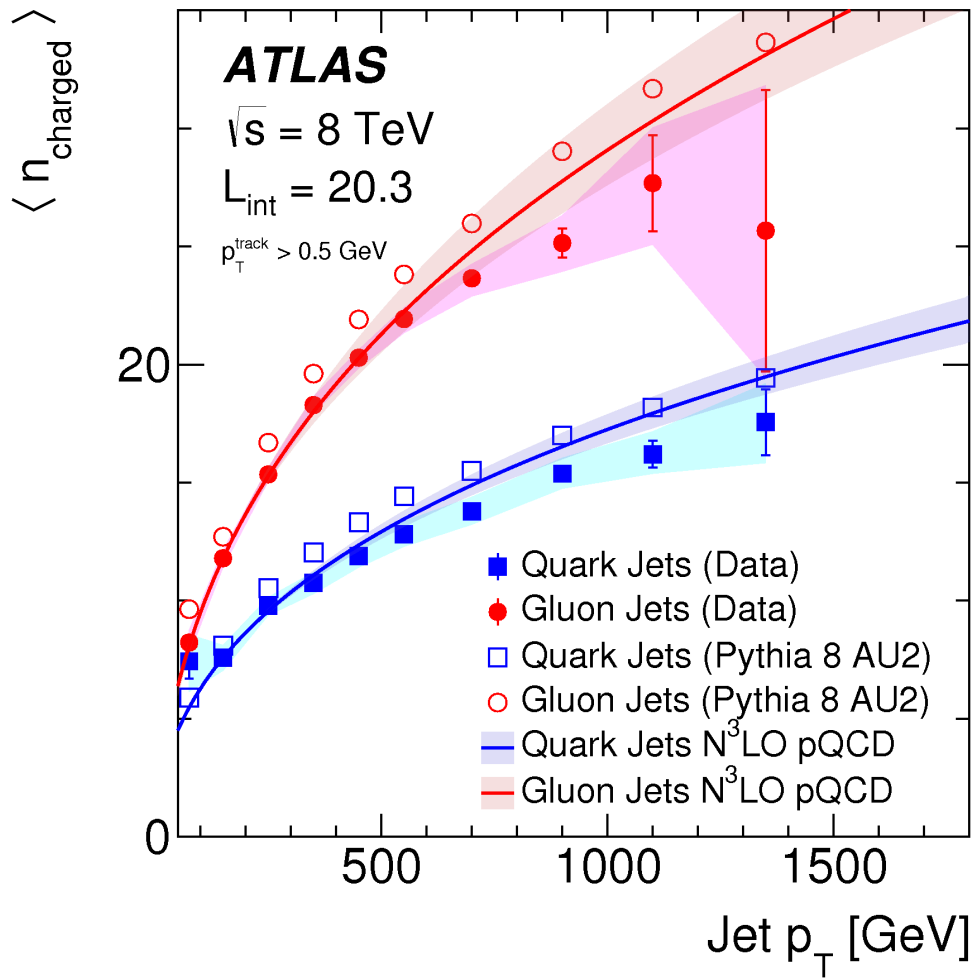


Figure 4.11: Unfolded and extracted n_C qg dstbs..

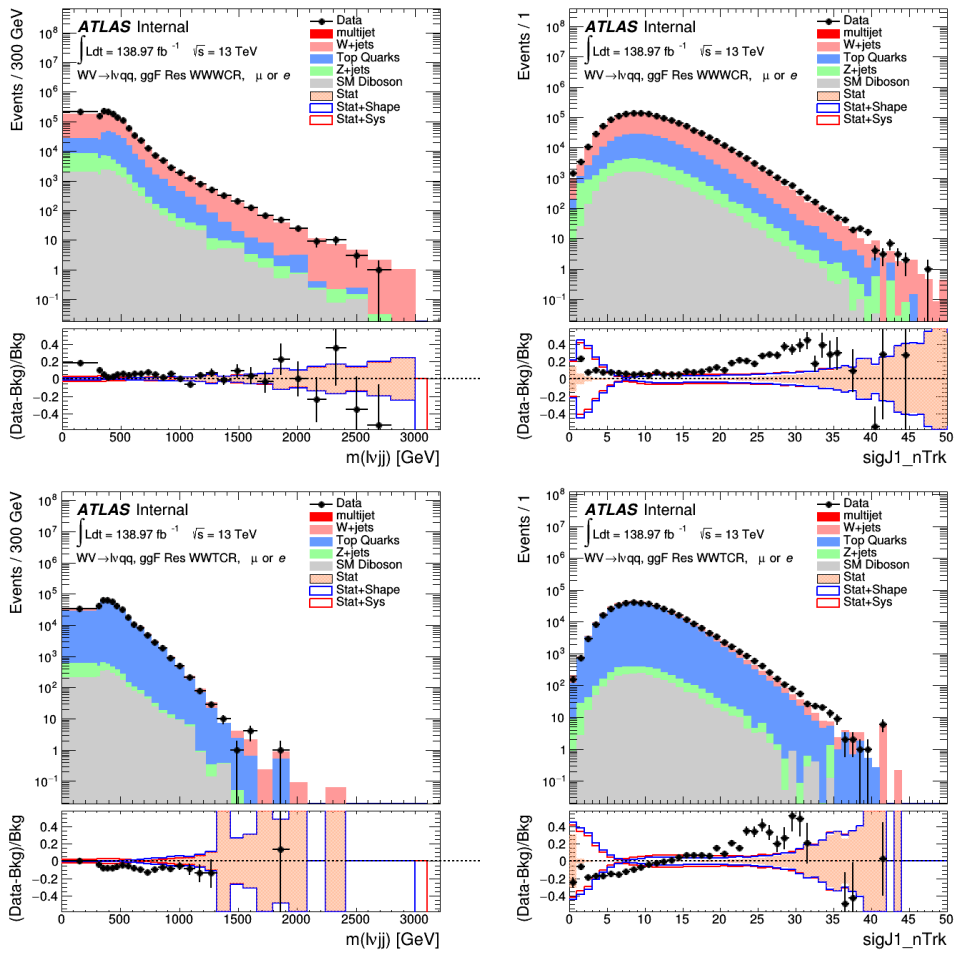


Figure 4.12: PDGID of the truth-level parton matched to the small-R jets passing the Resolved GGF WW Signal Region selections for the (a) Leading (b) Sub-Leading jets . These distributions are shown for 300, 500, and 700GeV Z' signals and the background.

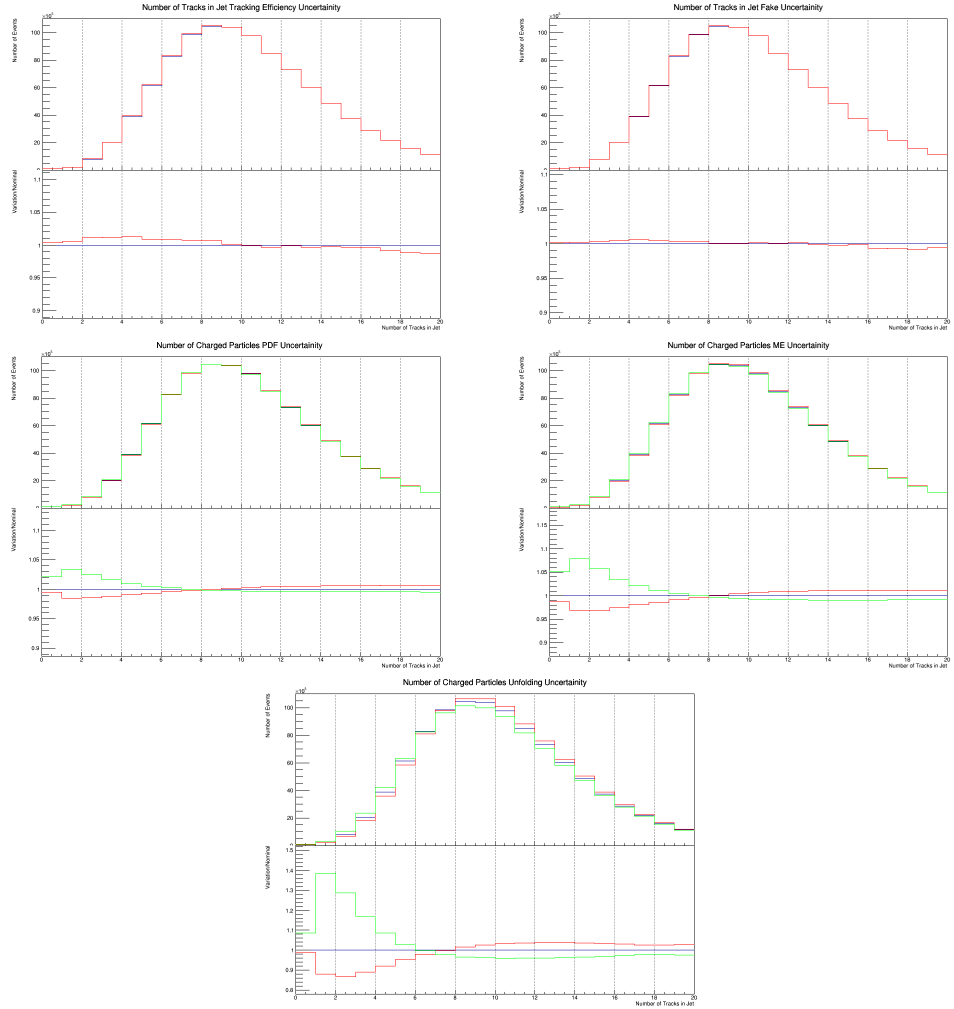


Figure 4.13: These figures show the impact of the uncertainties on the number of tracks in the leading jet in the sum of the background sample in the Resolved GGF WW SR (a) tracking efficiency (b) fake (c) PDF (d) ME (e) unfolding uncertainties.

1434 **Chapter 5**

1435 **Conclusion**

1436 **5.1 Conclusions**

1437 This is where conclusions go.

¹⁴³⁸ Bibliography

- ¹⁴³⁹ [1] Lecture notes particle physics ii.
- ¹⁴⁴⁰ [2] Kaustubh Agashe, Hooman Davoudiasl, Gilad Perez, and Amarjit Soni.
¹⁴⁴¹ Warped Gravitons at the LHC and Beyond. *Phys. Rev.*, D76:036006, 2007.
- ¹⁴⁴² [3] G. Altarelli and G. Parisi. Asymptotic freedom in parton language. *Nuclear*
¹⁴⁴³ *Physics B*, 126(2):298 – 318, 1977.
- ¹⁴⁴⁴ [4] ATLAS Collaboration. Atlas muon reconstruction performance in lhc run 2.
- ¹⁴⁴⁵ [5] ATLAS Collaboration. Summary plots from the atlas standard model physics
¹⁴⁴⁶ group.
- ¹⁴⁴⁷ [6] ATLAS Collaboration. Jet energy scale measurements and their systematic
¹⁴⁴⁸ uncer- tainties in proton–proton collisions at $\sqrt{s} = 13$ tev with the atlas
¹⁴⁴⁹ detector. arXiv: 1703.09665 [hep-ex].
- ¹⁴⁵⁰ [7] ATLAS Collaboration. Measurement of the charged-particle multiplicity
¹⁴⁵¹ inside jets from $s=\sqrt{8}$ tev pp collisions with the atlas detector.
¹⁴⁵² arXiv:1602.00988 [hep-ex].
- ¹⁴⁵³ [8] ATLAS Collaboration. Performance of the atlas track reconstruction algo-
¹⁴⁵⁴ rithms in dense environments in lhc run 2. arXiv:1704.07983 [hep-ex].
- ¹⁴⁵⁵ [9] ATLAS Collaboration. Properties of jet fragmentation using charged par-
¹⁴⁵⁶ ticles measured with the atlas detector in pp collisions at $\sqrt{s} = 13$ tev.
¹⁴⁵⁷ arXiv:1906.09254 [hep-ex].
- ¹⁴⁵⁸ [10] Alex Dias and V. Pleitez. Grand unification and proton stability near the
¹⁴⁵⁹ peccei-quinn scale. *Physical Review D*, 70, 07 2004.
- ¹⁴⁶⁰ [11] Stefan Höche, Frank Krauss, Marek Schönherr, and Frank Siegert. Qcd ma-
¹⁴⁶¹ trix elements + parton showers. the nlo case. *Journal of High Energy Physics*,
¹⁴⁶² 2013(4), Apr 2013.
- ¹⁴⁶³ [12] Gregory Soyez Matteo Cacciari, Gavin P. Salam. The anti- k_T jet clustering
¹⁴⁶⁴ algorithm. arXiv:0802.1189 [hep-ph].

- 1465 [13] Duccio Pappadopulo, Andrea Thamm, Riccardo Torre, and Andrea Wulzer.
1466 Heavy vector triplets: bridging theory and data. *Journal of High Energy*
1467 *Physics*, 2014(9), Sep 2014.
- 1468 [14] Antonio Pich. The Standard Model of Electroweak Interactions. In *Proceed-*
1469 *ings, High-energy Physics. Proceedings, 18th European School (ESHEP 2010):*
1470 *Raseborg, Finland, June 20 - July 3, 2010*, pages 1–50, 2012. [,1(2012)].
- 1471 [15] Lisa Randall and Raman Sundrum. A Large mass hierarchy from a small
1472 extra dimension. *Phys. Rev. Lett.*, 83:3370–3373, 1999.
- 1473 [16] Tania Robens and Tim Stefaniak. Lhc benchmark scenarios for the real higgs
1474 singlet extension of the standard model. *The European Physical Journal C*,
1475 76(5), May 2016.